

ACOUSTIC NOISE REDUCTION IN AN 8/6 SWITCHED  
RELUCTANCE MACHINE USING STRUCTURAL DESIGN

# ACOUSTIC NOISE REDUCTION IN AN 8/6 SWITCHED RELUCTANCE MACHINE USING STRUCTURAL DESIGN

By

Nathan Emery, B.Sc.

A Thesis

Submitted to the School of Graduate Studies

in Partial Fulfilment of the Requirements

for the Degree

Master of Applied Science

McMaster University

© Copyright by Nathan Emery, May 2021

All Rights Reserved

MASTER OF APPLIED SCIENCE (2021)

McMaster University

(Mechanical Engineering)

Hamilton, Ontario, Canada

TITLE:

ACOUSTIC NOISE REDUCTION IN AN 8/6  
SWITCHED RELUCTANCE MACHINE USING  
STRUCTURAL DESIGN

AUTHOR:

Nathan Emery

B.Sc.

University of Richmond

(Richmond, Virginia)

SUPERVISORS:

Ali Emadi, Professor

Ph.D. (Texas A&M University)

IEEE Fellow

Canada Excellence Research Chair Laureate

Berker Bilgin, Assistant Professor

Ph.D (Illinois Institute of Technology)

IEEE Senior Member

NUMBER OF PAGES:

XIV, 132

Dedicated to my parents

# Abstract

Switched reluctance motors (SRMs) possess many desirable qualities for the long-term sustainability of electrified transportation such as cheap production costs and simple, robust configurations. However, high acoustic noise and torque ripple are two performance imperfections that have prevented the widespread implementation of SRMs. This thesis investigates design techniques to reduce the acoustic noise produced by an 8/6 SRM while also analyzing the impact each design has on the motor's performance.

The fundamentals of SRMs are discussed including the operating principles, modelling and control strategies. The multiphysics finite element analysis (FEA) toolchain used to accurately model acoustic noise and vibrations of SRMs is described. Using the network of FEA tools, nodal forces and natural frequencies of a four phase 8/6 SRM are analyzed to study the acoustic noise and vibration behaviours. The FEA process is validated experimentally by matching measured vibration modes and acoustic noise sound pressure level (SPL) with FEA numerical results.

Through inspiration from an extensive literature review, various design techniques are applied to a baseline four phase 8/6 SRM and compared for both acoustic noise reduction and EM performance criteria. The investigated designs were split into two categories, stator-housing modifications that aim to increase the stiffness of the assembly and rotor modifications that aim to reduce the magnitude of radial forces while preserving performance.

The best design strategies as determined by the comparative analysis were then further optimized to combine the best techniques together for the 8/6 SRM. The proposed structural improvements included the modifications of the stator yoke shape along with increasing the number of fastening components involved in the assembly. Additionally, an iterative procedure for the parametric modelling of windows introduced to the rotor poles is outlined. The best design considerations are combined to create the design of a novel 8/6 SRM which significantly reduces the acoustic noise produced by the motor with little impact to performance.

## Acknowledgments

I would like to firstly thank my supervisor Dr. Ali Emadi for providing the opportunity to be apart of an amazing group of world class researchers at MARC. His continuous support and encouragement helped me throughout my graduate studies.

I would like to give a special thank you to my co-supervisor Dr. Berker Bilgin for his leadership and guidance these past two years. I appreciate all the encouragement and advice he has provided for my research, publications, and this thesis. His leadership is inspiring, and I am grateful to have worked with him throughout my studies at McMaster.

A thank you goes out to all the electric machines group members, Jianbin Liang, Yawei Wang, Ahmed Abdelrahman, Ashish Sahu, Yihui Li and Sujana Dasara, whom I worked closely with on a day-to-day basis.

I would like to thank all my peers and co-workers from Dr. Emadi's research group at MARC. Special thanks goes to Aashit Rathore, Diego Garcia, Josh Taylor, Sumedh Dhale, Jeremy Lempert, Adam Lempert, Mina Naguib, Lucas Bruck, Atriya Biswas, Peter Azer, Fabricio Alvares, Josimar Duque and Wesam Taha. Their friendship and support during my graduate studies at MARC is appreciated and I am proud to have been apart of such a wonderful group of people.

I would also like to commemorate Iman Aghabali and Mehdi Dorcheh who I had the pleasure of knowing, may you both rest in peace.

Finally, I would like to thank my parents, Nancy and Dave and my brother Curtis for always supporting me and for all the sacrifices they have ever made to provide me with the opportunities to pursue my dreams. Thank you to Sophie for always being the person I can turn to and for never doubting me throughout my undergraduate and graduate journeys. Without my family and friends, I would not be the person who I am today, and I am forever grateful for them. I am very fortunate to be surrounded by people who care so much for me and push me to achieve what I set out to accomplish.

This research was undertaken in part thanks to funding from the Natural Sciences and Engineering Council of Canada (NSERC). I also gratefully acknowledge ANSYS for their support with ANSYS Workbench used in this research.



# Contents

<b>Abstract</b>	iv
<b>Acknowledgments</b>	vi
<b>List of Publications</b>	x
<b>List of Figures</b>	xi
<b>List of Tables</b>	xiv
<b>List of Abbreviations</b>	xiv
<b>1 Introduction and Motivation</b>	<b>1</b>
1.1 Electric Vehicle Traction Motors .....	2
1.2 Switch Reluctance Motors .....	3
1.3 Active Research in SRM Acoustic Noise Reduction .....	5
1.4 Thesis Outline .....	10
<b>2 Fundamentals of Switched Reluctance Machines</b>	<b>13</b>
2.1 Introduction .....	13
2.2 Operation Principles .....	13
2.3 Flux Linkage, Inductance and Magnetic Co-energy .....	14
2.4 Electromechanical Energy Conversion and Torque .....	19
2.5 Phase Excitation Sequence .....	21
2.6 Induced Voltage and System Dynamics .....	23
2.7 SRM Dynamical Modelling Techniques .....	25
<b>3 Vibration and Acoustic Noise Modelling and Analysis for Switched Reluctance Motors</b>	<b>29</b>
3.1 Electromagnetic forces .....	29
3.2 Mechanical Vibrations and Acoustic Noise .....	38
3.2.1 Vibration Fundamentals.. .....	39
3.2.2 Mode Shapes .....	42
3.3 Resonance Excitation .....	44
3.4 Mechanical Modelling Considerations .....	46
3.5 Damping Ratio Losses .....	49
3.6 Acoustic Noise Modelling .....	51
3.7 Multiphysics FEA Network .....	56

---

<b>3.8 FEA Module Considerations</b> .....	59
<b>3.9 Experimental Validation of the Multiphysics Vibroacoustic Model</b> .....	63
<b>4 Structural Design Techniques in SRMs for Acoustic Noise and Vibration Reduction</b>	<b>70</b>
<b>4.1 Baseline Motor Design</b> .....	71
<b>4.2 Stator-Housing Assembly Considerations</b> .....	79
<b>4.3 Stator Yoke Modifications</b> .....	80
<b>4.4 Fastener Component Considerations</b> .....	87
<b>4.5 Stator Back Iron Notches</b> .....	89
<b>4.6 Rotor Modifications</b> .....	93
<b>4.7. Rotor Pole Tip Modifications</b> .....	99
<b>5 Acoustic Noise Reduction in the 8/6 SRM Using Structural Design Methods</b>	<b>103</b>
<b>5.1 Stator-Housing Design</b> .....	103
<b>5.2 Rotor Modifications for Acoustic Noise Reduction</b> .....	109
<b>5.2.1 Iteration I</b> .....	109
<b>5.2.2 Iteration II</b> .....	112
<b>5.2.3 Rotor Mass Reduction</b> .....	115
<b>5.3 Final Design Modifications</b> .....	118
<b>6 Conclusions and Future Work</b>	<b>122</b>
<b>6.1 Thesis Summary</b> .....	122
<b>6.2 Future Work</b> .....	125
<b>References</b> .....	128

## List of Publications

### Conference Papers

1. **N. Emery**, S. Dasara, J.Liang, D.Al-Ani, A. Emadi, B.Bilgin, “Study on the effect of dynamic eccentricity on acoustic noise of an interior permanent magnet traction motor,” in *Proc. IEEE Transportation Electrification Conference & Expo. (ITEC)*, Chicago, IL, USA, 2020. Pp1147-1152
2. **N. Emery**, Y.Yang, D. Al-Ani, B. Bilgin, “Acoustic noise and vibration of an interior permanent magnet traction motor: PWM effect,” accepted to *IEEE Transportation Electrification Conference & Expo. (ITEC)*, Chicago, IL, USA, 2021.

### Journal Papers

1. M.Naguib, A. Rathore, **N.Emery**, S.Ghasemi, R.Ahmed, “Robust electro-thermal modelling of lithium-ion batteries for electrified vehicles applications,” submitted to *Journal of Emerging and Selected Topics in Power Electronics*.

# List of Figures

Fig. 1.1 Traction motor candidate cross sections (a) 48 slot 4 pole IPMSM (b) 18 stator slot 26 rotor slot 4 pole IM .....	3
Fig. 1.2 Cross section of an 8/6 interior rotor SRM.....	4
Fig. 1.3 Flowchart diagram of various SRM mechanical design techniques for vibration and acoustic noise reduction.....	6
Fig. 1.4 Notations for common SRM design features.....	7
Fig. 1.5 Comparison of rotor pole topologies (a) conventional (b) novel design from [40] (c) improved novel design from [37].....	9
Fig. 1.6 Various notch designs from literature (a) square notches [43] (b) circular notches [44] (c) arrow notches [34] .....	10
Fig. 2.1 Flux linkage of magnetic field energy and co-energy versus current [47] .....	16
Fig. 2.2 Phase inductance of SRM at various rotor positions at constant current [6] .....	18
Fig. 2.3 Flux linkage vs current characteristics of SRM laminations from unaligned to aligned positions [6] .....	19
Fig. 2.4 Idealized phase current and inductance for sequential phase excitation [6] .....	22
Fig. 2.5 Flux-linkage curves for rotor position versus current, (a) unsaturated SRM (b) saturated SRM [47] .....	23
Fig. 2.6 Equivalent circuit diagram for a single-phase SRM.....	25
Fig. 2.7 (a) Flux linkage, (b) torque, and (c) induced voltage vs. current FEA data exported for LUTs [6].....	26
Fig. 2.8 Simulink voltage control for SRM operation [47].....	28
Fig. 3.1 Circumferential order relationship with shape [49].....	31
Fig. 3.2 Radial force density of a four phase 8/6 SRM.....	32
Fig. 3.3 Dominant radial force density harmonics for a four phase 8/6 SRM .....	33
Fig. 3.4 Rotational directions of surface waves in all four quadrants [2] .....	35
Fig. 3.5 First and third quadrant radial force density surface wave characteristics traveling in the CW direction of the stator circumference [22] .....	37
Fig. 3.6 Radial force density harmonic amplitudes vs. temporal orders.....	38
Fig. 3.7 Spring mass damper system.....	39
Fig. 3.8 Forced vibration damped system .....	41
Fig. 3.9 Circumferential mode shapes for a cylindrical shell for circ=(a) 0 (b) 1 (c) 2 (d) 3 (e) 4 and (f) 5 [22].....	42
Fig. 3.10 Mode shapes of a cylindrical shell for circumferential and axial orders [50].....	43
Fig. 3.11 Radial force density harmonics resonance excitation of vibration mode 2 for a four phase 8/6 SRM.....	45
Fig. 3.12 Radial force density harmonics for a 24/16 SRM [50] .....	46
Fig. 3.13 Bolts contacts used in mechanical modelling of connections for SRM assemblies .....	47
Fig. 3.14 Vibration modes of individual coils vs. combined windings [50] .....	48
Fig. 3.15 (a) Assembly connections for an SRM and (b) system damping losses [2] .....	50

Fig. 3.16 Longitudinal acoustic pressure wave visualization .....	52
Fig. 3.17 Acoustic environment interface [50] .....	55
Fig. 3.18 Virtual microphone locations according to ISO 3744 standard [50] .....	56
Fig. 3.19 Multiphysics FEA network of connections for SRM acoustic noise analysis .....	58
Fig. 3.20 Mapped 3D nodal forces to SRM stator teeth.....	59
Fig. 3.21 2D electromagnetic meshing .....	60
Fig. 3.22 Stator and windings mesh interface .....	62
Fig. 3.23 Cross sectional view of the acoustic near field mesh .....	63
Fig. 3.24 Experimental setup for acoustic noise measurement of the four phase 8/6 SRM [22,50] .....	64
Fig. 3.25 Stator-housing assembly CAD model for the 8/6 SRM .....	65
Fig. 3.26 FEA calculated vibration mode's for the 8/6 SRM .....	66
Fig. 3.27 Impact hammer test frequency-domain response when (a) struck in middle of stator lamination and (b) struck on the bolted corner .....	66
Fig. 3.28 Phase currents for one electric cycle at 2000 rpm 5 Nm reference.....	67
Fig. 3.29 (a) Experimental SPL results from [22] and (b) FEA calculated SPL results .....	69
Fig. 3.30 Acoustic noise near field directivity plots (a) mode (2,1) resonance at 1843 Hz and (b) mode (2,2) resonance at 2662 Hz.....	69
Fig. 4.1 Baseline 8/6 SRM stator and rotor dimensions [53].....	71
Fig. 4.2 Exploded view of the baseline 8/6 motor assembly.....	72
Fig. 4.3 Induced voltage vs. constant current.....	73
Fig. 4.4 Torque, Induced Voltage and Flux Linkage LUTs.....	74
Fig. 4.5 Dynamic phase currents and torque for the baseline 8/6 SRM at 2000 rpm .....	75
Fig. 4.6 Spatial and temporal decomposition of radial force density harmonics .....	75
Fig. 4.7 Mode (2,1) natural frequencies of the baseline 8/6 stator.....	76
Fig. 4.8 (a) Deformation and (b) stress contour from the forced vibration simulation at 2600 Hz	77
Fig. 4.9 Acoustic noise SPL results for the baseline 8/6 SRM .....	77
Fig. 4.10 Radial force density harmonics (78,2) and (90,2) that excite vibration mode 2 of the baseline 8/6 SRM.....	78
Fig. 4.11 Bolted contact modes (2,1) natural frequencies (a) 2242.2 Hz and (b) 2298.2 Hz vs. interference press fit contact modes (2,1) (c) 3030Hz and (d) 3551.7 Hz .....	80
Fig. 4.12 Stator yoke shape designs (a) octagon I (b) octagon II (c) square (d) hybrid octagon ...	81
Fig. 4.13 Deformation contour plots for (a) octagon II (b) hybrid octagon and (c) baseline and stress contour plot for (d) octagon II (e) hybrid octagon and (f) baseline .....	83
Fig. 4.14 Total SPL comparison for octagon II and hybrid octagon designs vs. baseline .....	84
Fig. 4.15 Increased fastener components .....	88
Fig. 4.16 Stator back iron notch design .....	90
Fig. 4.17 Flux line comparison between (a) the baseline stator and (b) the notched back iron stator .....	90
Fig. 4.18 Deformation contour plot for the (a) baseline design and (b) notched stator back iron design.....	91
Fig. 4.19 Acoustic noise SPL comparison for notched stator back iron design.....	92

Fig. 4.20 Baseline design static characteristics (a) torque and (b) radial force.....	94
Fig. 4.21 Various rotor window geometries (a) square (b) triangle (c) circle (d) oval I (e) oval II	95
Fig. 4.22 Rotor window performance comparisons for (a) torque and (b) radial forces.....	96
Fig. 4.23 Performance ratio comparison for various window shapes .....	96
Fig. 4.24 Rotor vs. stator window comparisons (a) torque and radial force reductions (b) performance ratios .....	97
Fig. 4.25 Stator and rotor laminations with parametric circular windows .....	98
Fig. 4.26 Rotor, stator and combined circular window design comparisons based on proximity to the airgap (a) torque and radial force decreases and (b) performance ratios .....	98
Fig. 4.27 Various rotor laminations with pole modifications (a) rectangular pole surface notch (b) semi-circular pole surface notch (c) rotor rib (d) curved rotor poles .....	100
Fig. 4.28 Comparison of the various rotor modifications (a) torque and (b) radial force .....	101
Fig. 4.29 Performance ratio comparison of the various rotor modifications .....	101
Fig. 5.1 Acoustic noise reduction strategies flowchart .....	104
Fig. 5.2 Exploded view of Design I .....	105
Fig. 5.3 Design I vibration mode (2,1) at (a) 3491.6 Hz and (b) 3492.5 Hz.....	106
Fig. 5.4 Design II vibration mode (2,1) at (a) 3586.4 Hz (b) 3587.8 Hz .....	106
Fig. 5.5 Acoustic noise comparisons for Designs I and II .....	108
Fig. 5.6 Radial force density harmonics responsible for resonance overlap and peak acoustic noise .....	108
Fig. 5.7 Parametric sweep for size and location of the circular rotor window (a) torque (b) radial force .....	110
Fig. 5.8 Dynamic EM results for the optimal circular rotor window (a) torque and (b) radial force .....	111
Fig. 5.9 Dynamic current profile vs. torque .....	112
Fig. 5.10 Introduced notch to the leading edge of the rotor pole .....	113
Fig. 5.11 Parametric sweep for the angle of the leading edge notch (a) torque (b) radial force ..	114
Fig. 5.12 Dynamic simulation comparisons for iterations I and II (a) torque and (b) radial force .....	115
Fig. 5.13 Rotor lamination with cut-outs to reduce mass .....	116
Fig. 5.14 Exploded view of the Final Design for the 8/6 SRM.....	118
Fig. 5.15 Acoustic noise comparison of the Final Design to the baseline design of the 8/6 SRM .....	119
Fig. 5.16 Final Design EM performance analysis (a) torque and (b) radial force.....	120

## List of Tables

Table.3.1 Reference sound pressure levels, sound pressures and sound intensities [51] .....	54
Table 3.2 Exerimental SPL vs. FEA calculated SPL .....	68
Table 4.1 Material properties for the baseline 8/6 SRM assembly .....	72
Table 4.2 Stator yoke designs and corresponding mode 2 natural frequencies .....	82
Table 4.3 Evaluated performance criteria for the evaluated stator yoke designs .....	85
Table 4.4 Total assembly mass for modified stator yoke designs .....	86
Table 4.5 Mode (2,1) natural frequencies of increased bolt designs .....	87
Table 4.6 Mode (2,1) natural frequencies of an additional flange mount design .....	89
Table 4.7 EM performance of the notched back iron design .....	90
Table 5.1 Designs I and II component and total mass comparison .....	109
Table 5.3 Performance evaluations for the best 8/6 SRM designs .....	121

## List of Abbreviations

2D	Two dimensional
3D	Three dimensional
CW	Clockwise
CCW	Counter-clockwise
FEA	Finite Element Analysis
IM	Induction machine
IMPSM	Interior permanent magnet synchronous motor
LUT	Lookup table
PR	Performance ratio
PWM	Pulse width modulation
RPM	Revolutions per minute
SPL	Sound pressure level
SRM	Switched reluctance motor
TSF	Torque sharing function

# Chapter 1

## Introduction and Motivation

The global shift towards greener technologies has been a major emphasis in recent years as the impacts of global warming and climate change grow increasingly. With more evident information known about the impacts of fossil fuels and greenhouse gas emissions, leaders of countries around the globe have started increasing their efforts to reduce global warming. These efforts include the introduction of carbon taxes, regulations of carbon emissions and development of cleaner, more efficient sources of energy. The emphasis for change in daily energy consumption has launched the development of new technologies in a wide range of industries. Research has significantly improved technologies and resources for everything from the electrical grid that power cities to the transportation sector. The field of renewable energy has experienced significant global growth in recent years and is paving the way for the future.

Consequently, the automotive industry is shifting gears from traditional fossil fueled internal combustion engines to electrification of vehicles. In the United States alone, the fossil fueled transportation industry contributed as much as 36.6 % of all carbon dioxide emissions in 2018 [1]. Internal combustion engines and fossil fuels, which are used in the



majority of vehicles today, are inefficient energy sources and this large percentage of greenhouse gas emissions is a consequence of inefficient energy generation from the burning of fossil fuels. The electrification of transportation is pushing towards finding new long-term solutions to reduce greenhouse emissions and rely on more energy efficient energy production to supply the transportation sector.

## **1.1 Electric Vehicle Traction Motors**

With the expansion into transportation electrification, the development of hybrid electric and battery electric vehicles has become a staple for developing technologies of vehicle companies and manufacturers around the world. With this switch to electrification, selecting the best possible traction motor candidates for optimal performance is of most importance. The most popular choice for traction motors in electric vehicles on the market today are Interior Permanent Magnet Synchronous Motors (IPMSMs). This is a result of IPMSMs' high efficiency at low to medium speed ranges, and their ability to produce high torque density from the use of high energy density permanent magnets [2]. These traction motors provide good performance and have many benefits, but they suffer from some major disadvantages due to the use of rare earth elements in the permanent magnets. Firstly, the performance of rare earth element magnets is highly dependent on temperature, including the possibility of permanently damaging the magnets if demagnetization occurs. Secondly, the cost and supply of rare earth magnets are volatile. These types of magnets are expensive, and the availability of these materials makes the market subject to unreliable and inconsistent production costs [2-5]. Another candidate for traction motors in vehicles on

the market today are induction motors (IMs). IMs have become a popular choice for traction motors in the electrification industry, with big name companies such as Tesla adopting these motors for their electric vehicle models. These motors are asynchronous as the electric frequency of the rotating field differs from the mechanical speed of the rotor. IMs address the issue of using rare earth permanent magnets that IPMSMs face, however due to the induced current in the rotor IMs suffer from high copper losses which require the need for rotor cooling [6]. An example cross section of the two popular traction motor candidates along with their labelled components can be seen in Fig. 1.1.

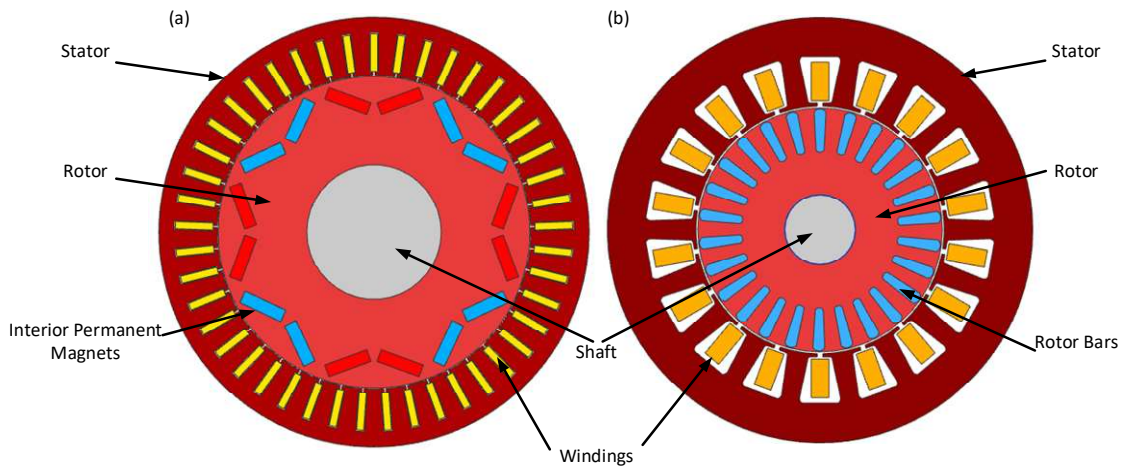


Fig. 1.1 Traction motor candidate cross sections (a) 48 slot 4 pole IPMSM (b) 18 stator slot 26 rotor slot 4 pole IM

## 1.2 Switched Reluctance Motors

To sustain the push for electrified transportation for the long term, a more sustainable traction motor technology is needed. A potential candidate to fill this void is the Switched Reluctance Motor (SRM). SRMs do not require the use of rare earth magnets or rotor

conductors and have simple and robust construction. SRMs are capable of operation at high speeds and high temperatures which helps to achieve high power density without the use of rotor excitation. The fundamental behaviour of reluctance torque generation for SRMs makes them more efficient in a wider speed range compared to IPMSMs as they do not require flux weakening at high speeds [7]. As a result, SRMs also have large constant power speed ranges and have fault tolerance capabilities as the winding phases are conventionally controlled and operated independently [8]. The simple geometry of SRMs reduces manufacturing complexity as it avoids the use of rare earth element permanent magnets and avoids rotor cavities for magnets or rotor bars. With simplified production and manufacturing costs, SRMs have the potential to provide long term solutions to the increasing demand for electric traction motors. The simple machine design topology can be seen in Fig. 1.2, where an example internal rotor SRM along with the labelled components are outlined.

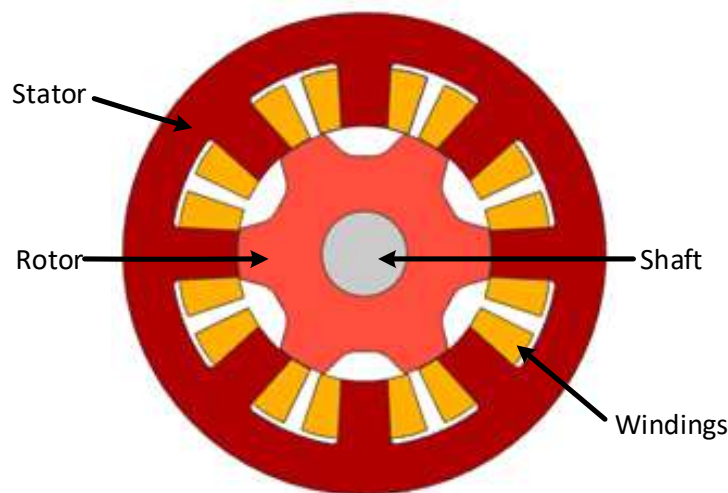


Fig. 1.2 Cross section of an 8/6 interior rotor SRM

The SRM proves advantageous over other traction motor candidates in many categories; however, SRMs face disadvantages that have prevented them from being the solution thus far. The major deterrent for the use of SRMs in traction applications is the high torque ripple and high radial forces produced by these motors, which result in excessive vibrations and acoustic noise. The high torque ripple and acoustic noise produced by SRMs are a result of salient rotor design and conventional operation characteristics of an SRM.

### **1.3 Active Research in SRM Acoustic Noise Reduction**

The reduction of torque ripple and acoustic noise produced by SRMs could address the disadvantages SRMs have and push these motors closer to being the ideal long-term solution for electrified transportation. Reduction techniques are related to both current control and mechanical design for these motors. Many approaches in both categories have been studied in literature to further improve the performance of SRMs. Firstly, from a controls aspect, the most common techniques include manipulating and optimizing current excitation profiles. Current switching techniques including optimization of turn on and turn off angles along with the use of torque sharing functions (TSFs) have been applied to produce smoother torque and reduce torque ripple [6, 9-13]. Additionally, further research in literature aims to reduce acoustic noise by targeting the reduction of radial forces through current shape profiling [14-22].

From a mechanical design perspective many techniques have been considered to improve the disadvantages of SRMs. The vast majority of which target the reduction or mitigation

of radial forces, which are the main contributor to SRM acoustic noise. The radial forces produced by SRMs create oscillating deformations of the stator which result in vibrations that transmit sound waves through the air surrounding the motor [23]. The characteristics and behaviours of these radial forces produced by SRMs will be further discussed in Chapter 3. To organize the extensive list of design techniques used in literature, a flow chart is presented in Fig. 1.3. These techniques are split into four general categories: machine topology, stator design, rotor design, and damping techniques.

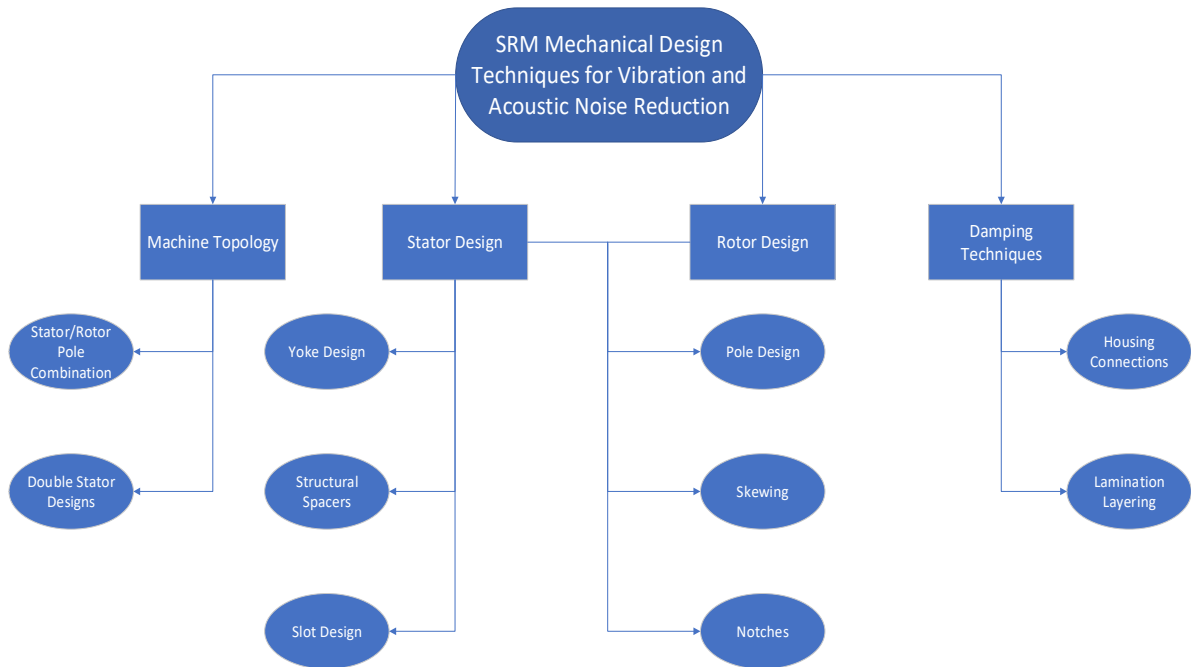
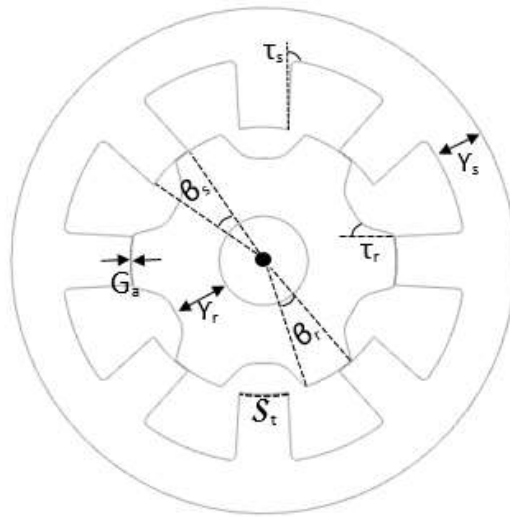


Fig. 1.3 Flowchart diagram of various SRM mechanical design techniques for vibration and acoustic noise reduction

Based on the literature, acoustic noise can be reduced by increasing the number of poles per phase, as dominant mode shapes will be pushed higher and reduce the overlap of mechanical resonance [24-29]. Additionally, some studies have recommended a higher

amount of rotor poles than stator poles to reduce acoustic noise [30]. In the machine topology category, research has also been conducted in [31-33] which introduced double stator SRM designs to decrease radial forces and obtain higher power density compared with conventional SRMs.

A large portion of research conducted in the field of mechanical design for SRM acoustic noise reduction is related to modifications of the stator and rotor. Some modifications apply strictly to stator design, while most design techniques can be applied to both the rotor and the stator. For classification of terminology references made in this section, various components of a typical SRM design are outlined in Fig. 1.4.



Notation	Description
$Y_s$	Stator yoke thickness
$Y_r$	Rotor yoke thickness
$\hat{\theta}_s$	Stator pole angle
$\hat{\theta}_r$	Rotor pole angle
$\tau_s$	Stator taper angle
$\tau_r$	Rotor taper angle
$G_a$	Airgap distance
$S_t$	Stator tooth

Fig. 1.4 Notations for common SRM design features

To improve structural stiffness, various shapes and thicknesses of stator yokes have been investigated in [34-38]. Specifically, by modifying the shape and size of stator yokes, these studies targeted the increase in stiffness and manipulation of stator natural frequencies to

minimize vibrations and limit natural frequency resonance. Additionally, in [34, 37], various shapes and designs of the stator winding slots were compared to measure the impact on stator deformation. A common practice in SRM manufacturing is the addition of slot wedges in between the stator poles to secure the windings in place. These slot wedges have been enhanced in [38, 39] to improve stator stiffness by using stiff dielectric materials such as alumina and polyvinyl chloride. The name for this enhancement is classified as structural spacers.

Modifying SRM mechanical designs is a multi-faceted problem where many things need to be considered. In order to target the reduction of vibrations and acoustic noise, the performance of the machine cannot be ignored. The principal cause of acoustic noise in SRMs is from the radial force on the stator teeth, which is the consequence of magnetic attraction between the rotor and stator [23]. The radial forces propagate from the stator teeth through the stator back iron to cause deformation and vibrations of the stator. The next category of stator and rotor design methods includes many studies which targeted the reduction of radial forces as a means of vibration and acoustic noise reduction. In this category, the modifications made include pole shape design, skewing and notching. All three of which can significantly decrease the performance of the motor if acoustic noise reduction is the only goal.

Firstly, improved stator and rotor shapes were introduced in [34,35,37,40]. Stator pole modifications included optimizing the stator taper angle and adjusting the profile of stator tooth shape. Rotor modifications in [37, 40] included novel designs of rotor poles, including the introduction of a curvature to the conventional extrusions of the rotor poles. This novel

rotor geometry can be compared to conventional designs as outlined in Fig. 1.5. These rotor modifications reduced the produced radial forces and hence acoustic noise of the machine, while maintaining efficiency with less than 0.5% reduction. This design modification aimed to change the characteristics of the magnetic flux path near the airgap to be comprised of more tangential flux than radial flux; therefore, reducing the magnitude of radial forces produced.

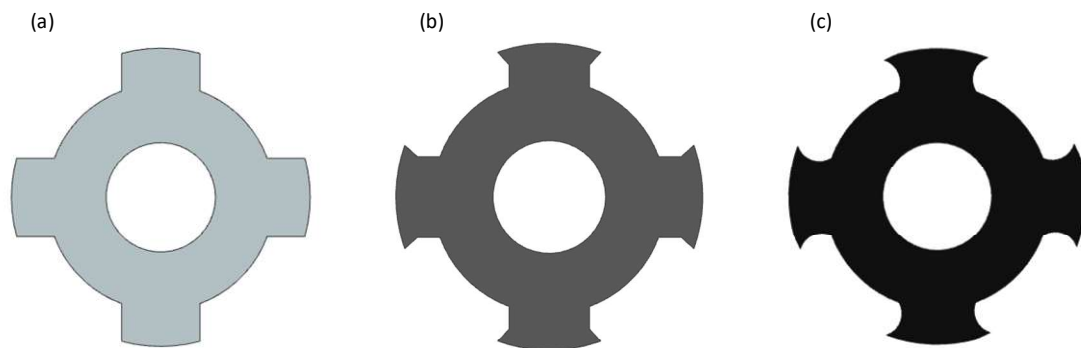


Fig. 1.5 Comparison of rotor pole topologies (a) conventional (b) novel design from [40]  
(c) improved novel design from [37]

Skewing is a common technique in existing studies for both the rotor and stator. These skewing techniques aim to distribute the radial force densities along the stator teeth and the axial length to reduce the magnitudes of deformations and vibrations. The introduction of skew angles can be effective towards reducing acoustic noise as seen in [41,42]. Skewing of the stator only was concluded as the most effective method for reducing acoustic noise while also preserving machine performance [42].



Recently, investigations have been conducted on the introduction of notches to the rotor and/or stator to mitigate acoustic noise. In [28,30,34,40,43,44], various types of notches were introduced to either the rotor or stator of the corresponding SRMs, including various shapes and locations. These techniques tracked EM performance closely as the notches change the characteristics of the flux linkage path. An example of a few designs that were investigated for notches in the rotor are outlined in Fig. 6. Lastly, damping techniques have also been applied to SRM designs by inserting damping materials in between stator laminations [45]. Another approach in [46], modified the contact areas and housing assembly that surround a motor to reduce the propagation of vibrations from the stator to the surrounding environment.

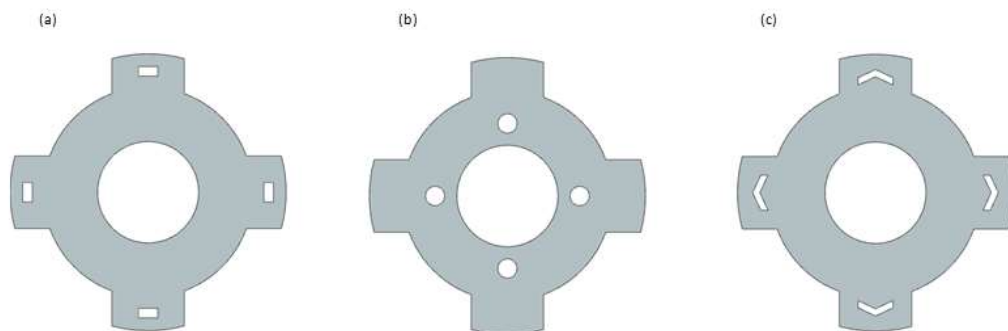


Fig. 1.6 Various notch designs from literature (a) square notches [43] (b) circular notches [44] (c) arrow notches [34]

## 1.4 Thesis Outline

In this thesis, machine design techniques to reduce the acoustic noise of an SRM have been proposed. These designs mitigate produced radial forces and the behaviours of the

system which produce noise, while maintaining the performance of the machine. By strategically designing the machine components, the disadvantages of SRMs can be reduced. These improvements can enhance SRMs and makes them an attractive machine topology to supply the long-term demand for traction motors.

The design techniques investigated in this thesis include modifying the stator yoke and housing components to increase the stiffness of the system while also reducing the magnitude of radial forces through the introduction of notches on the rotor. The reduction of acoustic noise for SRMs is a multifaceted issue that must address machine performance along with acoustic noise reduction. Therefore, the proposed design techniques evaluate many aspects of machine design involved when investigating acoustic noise reduction. To model, predict and reduce acoustic noise of SRMs, an extensive network of multiphysics Finite Element Analysis (FEA) modelling simulations has been developed and validated experimentally. The development and implementation of acoustic noise reduction techniques are organized for this thesis in the following way.

Chapter 2 starts by introducing the fundamental operating principles of SRMs. The dynamics involved in the operation of SRMs is outlined in detail. In this chapter, dynamic modelling techniques used for SRM analysis are presented and described in detail.

Chapter 3 introduces the analysis of radial forces and outlines the various noise, vibration and harshness (NVH) modelling techniques used to analyse SRMs. Fundamentals for vibration and acoustic noise as they apply to SRMs are described. The connections between multi physics FEA domains are explained and outlined. This chapter also include the

verification of FEA NVH analysis by comparing numerical results with the experimental results for a four phase 8/6 SRM.

Based on inspiration from an extensive literature review, Chapter 4 compares various mechanical design techniques for acoustic noise reduction. This chapter outlines effective design approaches for reducing the acoustic noise of a four phase 8/6 SRM. The best design techniques are chosen based on acoustic noise reduction with minimal impact on the performance of the machine.

Chapter 5 describes the design techniques to reduce acoustic noise while maintaining the performance of a four phase 8/6 SRM. The designs are obtained from parametric geometry analyses based on the best design considerations chosen in Chapter 4.

Finally, a conclusion and summary of the thesis is provided in Chapter 6. Future work and considerations are also presented.

## **Chapter 2**

# **Fundamentals of Switched Reluctance Machines**

### **2.1 Introduction**

The potential opportunities for SRM applications with improved design are promising as they have many advantages over other machine drives such as IPMSMs and IMs. To target and improve the current shortcomings of SRMs, an extensive understanding of the fundamental behaviours of the machine must be known. In this chapter, the fundamental operating principles will be discussed, including an overview of machine operation and electromechanical energy conservation. This chapter also outlines dynamic modelling and control techniques used for characterizing SRMs.

### **2.2 Operation Principles**

SRMs present highly nonlinear characteristics as a result of their salient stator and rotor pole construction. The operation of SRMs occurs when individual phases are excited with current. When a phase is excited, a resulting magnetic field is created between stator poles of the excited phase, which then magnetizes the rotor poles into alignment with the stator poles. By exciting the phases of SRMs in a sequential matter, the produced magnetic fields

force the rotor poles to continuously move into alignment with the stator poles of the excited phase.

### 2.3 Flux Linkage, Inductance and Magnetic Co-energy

To understand the operating principles and terminology for SRMs, flux linkage must be examined. For each turn of a coil in a phase winding, the flux is summed together according to (2.1), where  $N$  is number of coil turns and  $\psi$  is the total magnetic flux.

$$\lambda = N\psi \quad (2.1)$$

The total magnetic flux is calculated by integrating the magnetic flux density through an area as seen in (2.2), where  $S$  is the surface through which the flux is measured and  $\vec{B}$  is the magnetic flux density.

$$\psi = \int_S \vec{B} \cdot d\vec{S} \quad (2.2)$$

The magnetic flux density is dependant on  $\vec{H}$  field intensity and  $\mu$  the magnetic permeability of the material or medium as described in (2.3).

$$\vec{B} = \mu\vec{H} \quad (2.3)$$

Similarly, a relationship exists with the excitation current, magnetic flux and inductance. Inductance can be described as the inertia of the electromagnetic system, which is related to the dimensions and material characteristics of the ferromagnetic material, along with the

number of turns in the coil [2]. For SRMs, inductance can be described linearly when the relationship between current and flux are in the linear region of magnetic co-energy as described in (2.4), where  $i$  is current and  $\lambda$  is flux linkage.

$$L = \frac{i}{\lambda} \quad (2.4)$$

In SRMs the inductance and flux- linkage both depend on rotor position. The movement of the rotor poles changes the effective air gap length as it rotates because of its salient design, which causes variations in flux linkage and induces electromotive force to limit the rate of change of current. As a result, (2.4) can be expressed as function of rotor position  $\theta$  seen in (2.5).

$$\lambda(\theta, i) = L(\theta, i)i \quad (2.5)$$

In SRMs, the stators and rotors are composed of laminations of ferromagnetic material. The ferromagnetic material has a magnetic permeability that is much greater than air because of they include domains where the magnetic dipoles are in complete alignment. This is desirable because as the current is excited in the coils, the flux density in the pole will increase, but only to a certain point. This is where magnetic saturation becomes a factor. When the magnetomotive force is high, the ferromagnetic material will saturate, resulting in a reduction to the rate of increase in produced flux linkage. This non-linear relationship caused by saturation impacts the relationship between the magnetic field energy and co-energy depicted in Fig. 2.1.

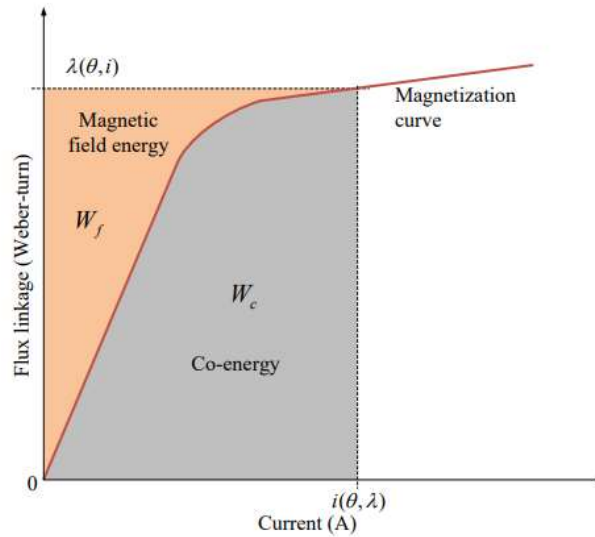


Fig. 2.1 Flux linkage of magnetic field energy and co-energy versus current [47]

The magnetic flux moves from the stator pole to the rotor pole through the airgap as the rotor rotates. This forms a magnetic circuit when a phase is excited. As the magnetic permeability of air is much smaller than that of the ferromagnetic materials, the reluctance in the airgap is much higher. Reluctance of a magnetic path is defined as in (2.6), where  $\ell_c$  is the length of the closed loop flux path,  $\mu_r$  is the relative permeability,  $\mu_0$  is the permeability of air and  $A_c$  is the cross-section area the flux flows through.

$$\mathcal{R} = \frac{\ell_c}{\mu_r \mu_0 A_c} \quad (2.6)$$

When related to inductance and flux linkage, reluctance can be expressed as (2.7). To understand the relationship reluctance has with inductance and magnetic flux, (2.7) can be

further simplified by substituting with (2.4) and (2.5) to be expressed simply as seen in (2.8).

$$\mathcal{R} = \frac{N^2}{L} \quad (2.7)$$

$$\mathcal{R} = \frac{Ni}{\psi} \quad (2.8)$$

As the magnetic field configuration changes with rotation of the rotor poles, the reluctance in the magnetic circuit is also changing and hence the reason for the naming of ‘reluctance machine’. This variation in flux linkage from the rotation of the rotor induces electromotive forces to limit the rate of change of current. This magnetic field behaves as the connecting link for electromechanical energy conversion. The stored magnetic energy  $W_f$  and magnetic co-energy  $W_c$  can be expressed as:

$$W_f = \int i d\lambda \quad (2.9)$$

$$W_c = \int \lambda di \quad (2.10)$$

Before electromechanical energy conversion is explained, the characteristics of flux linkage with respect to rotor position must be understood. To characterize the dynamic behaviour of an SRM system, three important rotor pole positions will be referenced



moving forward, which are the unaligned, mid-aligned and aligned positions. Unaligned corresponds to when a stator pole is in between rotor poles, when the relative distance between these poles is the largest. Mid-aligned position corresponds to a half overlap of the rotor pole and the stator pole and lastly aligned corresponds to when the rotor and stator poles are in alignment and the airgap is minimized. These positions are crucial to understanding the dependence of flux linkage and inductance on rotor position. The unaligned position results in minimum flux linkage due to the large airgap. In the aligned position, flux linkage and inductance are maximized as the airgap between the poles is the smallest and maximizes the effective permeability. A visualization of flux linkage based on rotor position can be seen in Fig. 2.2.

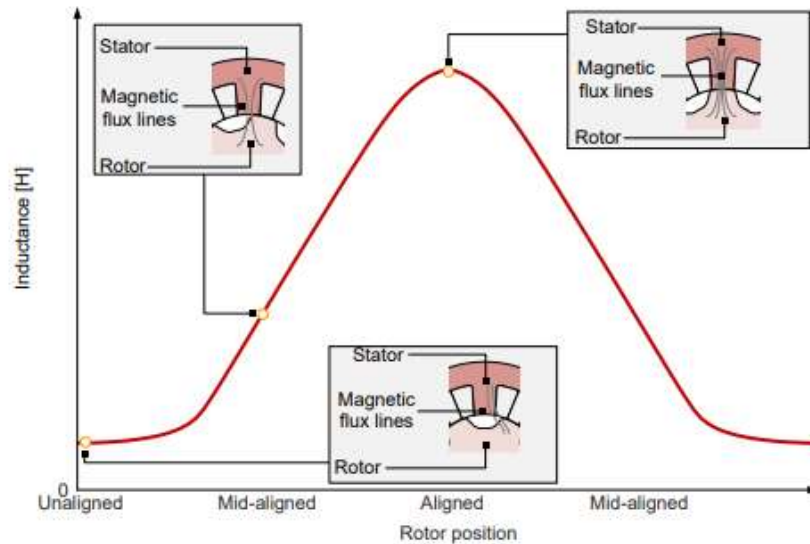


Fig. 2.2 Phase inductance of SRM at various rotor positions at constant current [6]

## 2.4 Electromechanical Energy Conversion and Torque

The production of torque in SRMs is dependant on the rate of change of stored energy in the system. When a stator pole is energized, the amount of stored energy in the magnetic circuit changes as the rotor pole starts to align with the stator. This is because as the rotor moves from the unaligned to aligned position, the airgap length changes due to the salient pole design and hence increases flux linkage. In Fig. 2.3, the flux linkage characteristics can be visualized for increasing current based on rotor position.

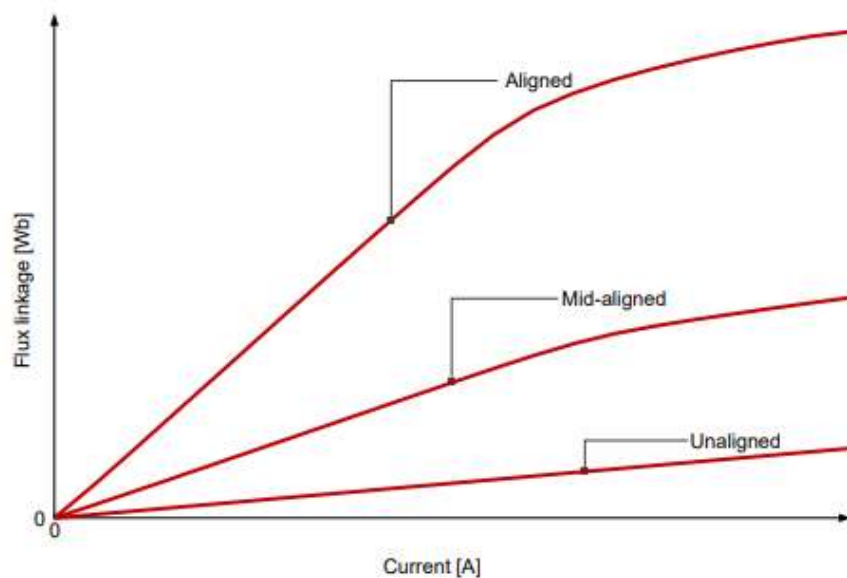


Fig. 2.3 Flux linkage vs current characteristics of SRM laminations from unaligned to aligned positions [6]

At the aligned position, due to the increase in the effective permeability of the magnetic circuit, the magnetic field energy decreases, and magnetic co-energy increases. This increase in magnetic co-energy is converted into mechanical energy in the form of

rotational motion. For a constant current excitation, torque can be expressed as the rate of change of the magnetic co-energy in the system as outlined in (2.11).

$$T = \frac{\delta W_c}{d\theta} \quad (2.11)$$

Additionally, the previously stated (2.10) for magnetic co-energy can be simplified in the linear region in respect to rotor position by (2.12)

$$W_c = \frac{1}{2}L(\theta)i^2 \quad (2.12)$$

which then simplifies generated torque to (2.13).

$$T = \frac{1}{2} \frac{dL(\theta)}{d\theta} i^2 \quad (2.13)$$

This relationship between torque, inductance and rotor position relates to a single rotor pole as it rotates into alignment with an excited stator pole. This explanation of torque generation has been simplified to understand the electro-mechanical energy conversion for a single rotor pole alignment. The next operational concept of SRMs is continuous torque generation for multi-phase multi-pole SRMs. In order to generate continuous torque, the phase excitations of stator poles must occur in a sequential pattern to facilitate the proper generation of torque for machine operation.

## 2.5 Phase Excitation Sequence

The generation of torque for an SRM relies on the specific phase excitation of the currents in the stator windings. The phase excitation sequence drives either the motoring or generating mode for an SRM with the production of positive or negative torque. As an individual phase is excited, the rotor will move into alignment with the stator pole of that phase. To facilitate continuous rotation, the phases must be sequentially excited. For positive torque generation, or motoring mode, SRM phases must be demagnetized before the rotor pole passes the aligned position. This corresponds to the sequential excitation of each phase in the positive slope of the flux linkage.

The rotor moves from the unaligned to aligned position from the excited stator phase to minimize the reluctance in the magnetic circuit [48]. In the aligned position, both the inductance and flux linkage are at their peak values. The inductance decreases passed the aligned position and becomes zero when the rotor reaches to the unaligned position again. In order to produce continuous torque and avoid negative braking torque, the currents for the phases must be turned on and off in a proper manner. Negative braking torque occurs if the phase current remains excited after the rotor moves beyond the aligned position. To avoid this, the timing of turning the phase current on and off is crucial. An example transition between phase excitations can be seen in Fig. 2.4.

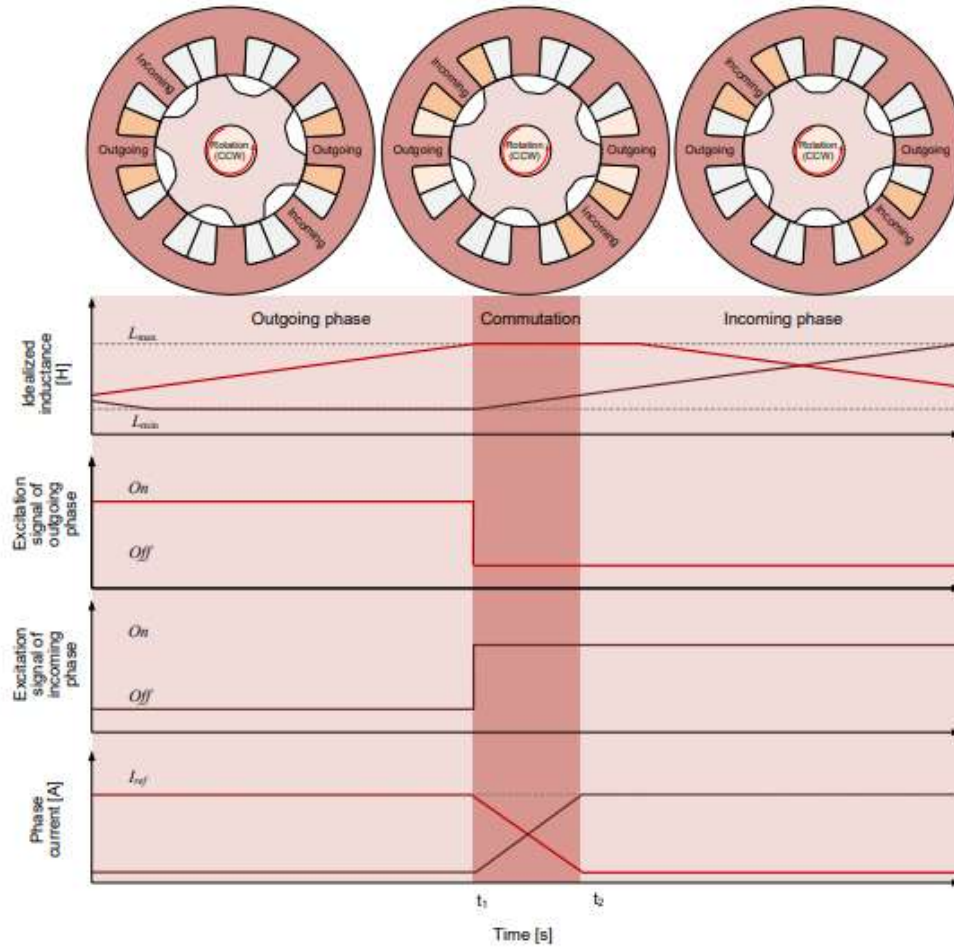


Fig. 2.4 Idealized phase current and inductance for sequential phase excitation [6]

The relationship the phase excitation sequence has with the magnetic co energy can be combined with the magnetic co-energy and saturation principles in Fig. 2.5 which describes the flux linkage and magnetic co-energy according to the rotor position for an unsaturated SRM and a saturated SRM.

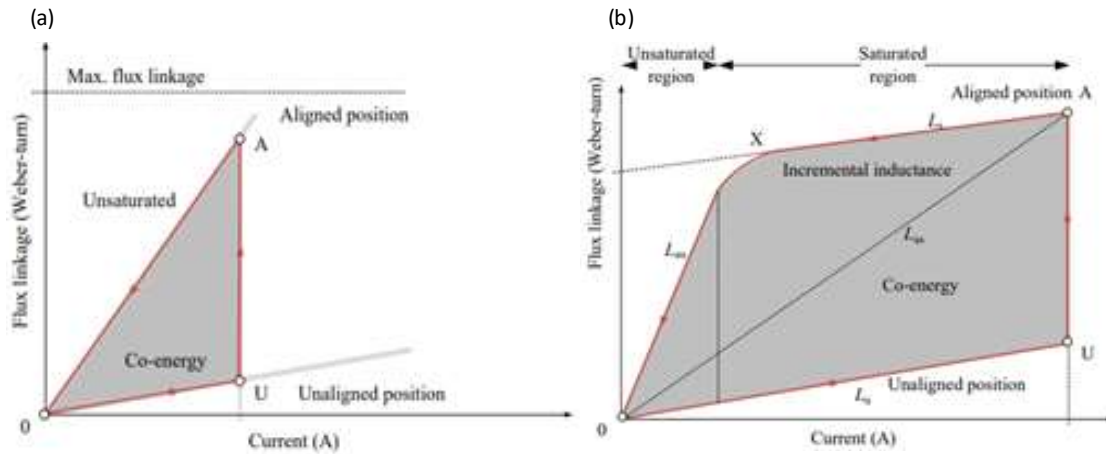


Fig. 2.5 Flux-linkage curves for rotor position versus current, (a) unsaturated SRM (b) saturated SRM [47]

In Fig.2.5 (a) the unsaturated SRM flux linkage limits the maximum energy that can be generated. In comparison, Fig 2.5 (b) depicts the flux linkage of a saturated SRM. It can be observed that the amount of energy generated is higher than the unsaturated case. Additionally, the saturated case can apply a higher current. The enclosed area represented by points  $OUAX0$  is the mechanical energy when the rotor moves from unaligned to aligned position in one electrical cycle [47]. A saturated SRM can help improve the torque density as the average torque is related to the rate of change of co-energy.

## 2.6 Induced Voltage and System Dynamics

For simplification, the induced voltage and system dynamics can be explained using the linear regions of operation. Without loss of generality, these underlying principles can also be applied to the magnetic saturated regions. Therefore, for the linear region of operation, the equivalent voltage equation for one phase of an SRM can be derived from Faraday's

law of magnetic induction as seen in (2.14). The terminal voltage  $V$  is supplied to the phases,  $R$  is the phase resistance and the change in flux linkage with respect to time is the induced voltage.

$$V = iR + \frac{d\lambda(\theta, i)}{dt} \quad (2.14)$$

In the linear region, the flux linkage is represented in terms of inductance and current which allows the induced voltage term in (2.14) above to be expanded into (2.15) below. This expression outlines that the terminal voltage of an SRM is comprised of a voltage due to the inductance in the coil and an electromotive force (EMF) that is a product of the changing inductance.

$$V = iR + L(\theta) \frac{di}{dt} + i \frac{dL(\theta)}{d\theta} \frac{d\theta}{dt} \quad (2.15)$$

The change in inductance with respect to rotor position is dependent on the time rate of change of the rotor position, which simply stated is the angular speed of the rotor. This means the induced voltage is dependent on rotor speed. Additionally, the EMF can be expressed as the third term on the right in (2.15), and expressed as (2.16), where  $\omega$  is the angular speed of the rotor. This voltage has an impact on the dynamics of phase current in SRMs as it is due to the changing magnetic field that is created during phase excitation.

$$\varepsilon = i \frac{dL(\theta)}{d\theta} \omega \quad (2.16)$$

The input power is also given by the product of voltage and current defined by (2.17)

$$Vi = i^2R + iL(\theta) \frac{di}{dt} + i^2 \frac{dL(\theta)}{d\theta} \omega \quad (2.17)$$

Here the first term,  $i^2R$ , is the ohmic losses and the third term,  $i^2 \frac{dL(\theta)}{d\theta} \omega$ , is the airgap power. An equivalent circuit diagram representing these system dynamics can be seen below in Fig. 2.6:

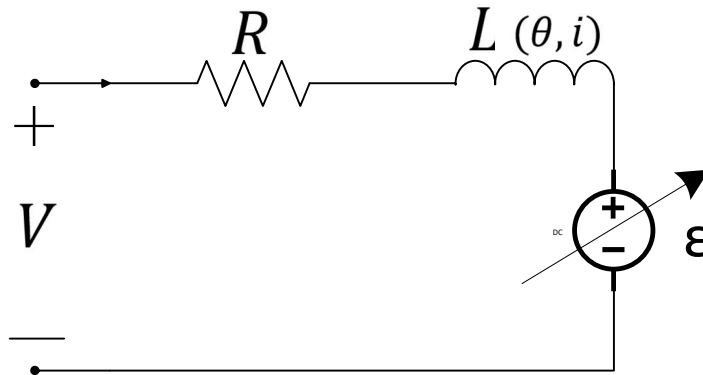


Fig. 2.6 Equivalent circuit diagram for a single-phase SRM

## 2.7 SRM Dynamical Modelling Techniques

Once the operating characteristics are understood, the dynamic modelling techniques of SRMs must be considered. The nonlinear characteristics of SRM operation makes the modelling techniques a crucial aspect when analysing these machines. Finite element



analysis (FEA) is used in conjunction with control models from MATLAB and Simulink to accurately describe the nonlinear dynamics of SRMs. Static electromagnetic simulations are conducted in FEA analysis to acquire the torque, flux linkage and induced voltage characteristics of the machine for a constant current single-phase excitation. For incremental values of constant current, these FEA calculated characteristics are then fed to a Simulink model as look up table (LUT) data for control purposes of SRMs. The three LUTs exported from FEA to Simulink include torque, flux linkage and induced voltage plotted with respect to electrical angle of the rotor pole, which can be seen in Fig.2.7.

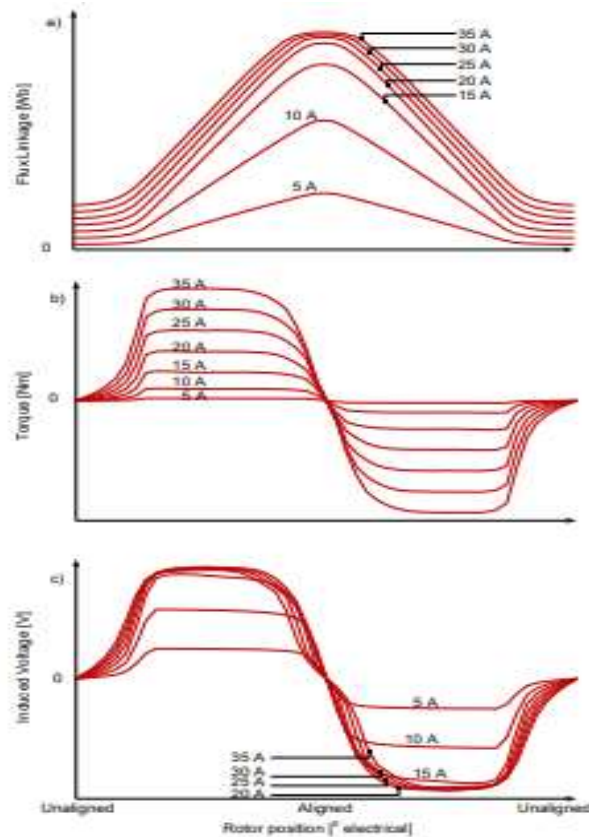


Fig. 2.7 (a) Flux linkage, (b) torque, and (c) induced voltage vs. current FEA data exported for LUTs [6]

The Simulink model is used for current control based on the specific characteristics of an SRM. To observe the dynamic performance of an SRM, this Simulink model calculates the dynamic characteristics of the machine at various operating conditions. This model must have high fidelity to capture the dynamic performance of an SRM accurately, but it must also be robust to give flexibility in control algorithms. This allows for rapid testing of many operating conditions which is extremely beneficial to SRM design.

For lower speed operation, the fundamental control strategy for SRMs involves -soft- or -hard- chopping for phase currents using Pulse Width Modulation (PWM). This is used to limit the current amplitude for voltage control purposes [48]. Each phase excitation is controlled via turn on and off conduction angles based on rotor position. For control purposes the electrical angle is a key consideration. Electrical angles are related to the number of rotor poles and number of phases of an SRM.

By convention, an unaligned rotor pole in a phase is referenced as 0 electrical degrees and aligned position is referenced as 180 electrical degrees. The relationship electric angle has with the number of phases and mechanical angle of the rotor is expressed in (2.18) where  $n_r$  is the number of rotor poles,  $\theta_r$  is mechanical angle of the rotor,  $k$  is the phase number from  $k = 0$  to  $k = m-1$  and  $m$  is the number of phases.

$$\theta_e = \text{mod}(n_r\theta_r + 180^\circ + \frac{k}{m}360^\circ, 360) \quad (2.18)$$

The use of electric angles for phase currents is useful when it comes to current control. The sequential order of excitations is the same current waveform, but phase shifted by  $\frac{360}{m}^\circ$ .

The phase currents behave based on the conduction angles, also named the turn on and turn off angles. Research has been conducted optimizing conduction angles to reduce torque ripple and improve SRM current control [6]. These conduction angles are crucial for the expected performance of SRMs.

The basic overview of the Simulink current controller can be seen in Fig. 2.8 for soft-switching control strategy. For continuous positive torque generation, the phase currents must be turned off before the inductance reaches its maximum. The turn on and off angles correspond to when the voltage is applied and reversed. As seen in Fig.2.8 the switching of the voltage is used to control the desired amplitude of the phase current in the hysteresis band region. Fig. 2.8 is simplified for a single-phase excitation, but for multi-phase operation, each phase is shifted for continuous torque generation as seen in the bottom continuous torque waveform profile.

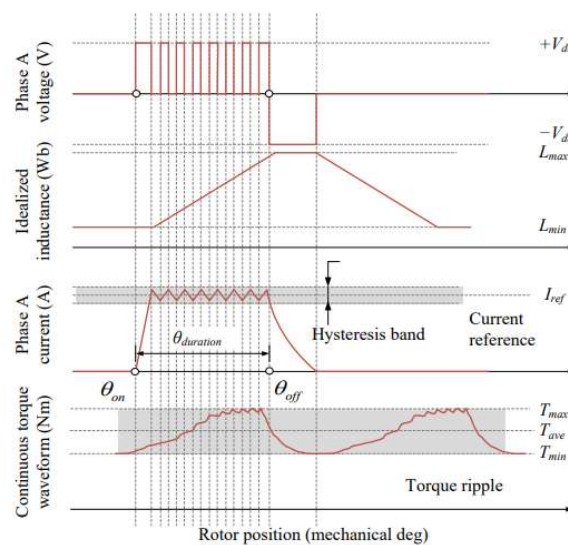


Fig. 2.8 Simulink voltage control for SRM operation [47]

## Chapter 3

# Vibration and Acoustic Noise Modelling and Analysis for Switched Reluctance Motors

This chapter outlines the modelling and analysis techniques for acoustic noise and vibrations of SRMs. Specifically, the techniques for decomposing and analysing radial forces generated by SRMs is explained. The fundamentals of vibrations and acoustic noise modelling for SRMs are outlined. Additionally, the flow of connections between multiphysics FEA simulations that are used for acoustic noise analysis is described. The details of FEA setup and meshing settings are further explained for best results for acoustic noise analysis. This chapter is concluded with an experimental validation of the FEA multiphysics flow using a four phase 8/6 SRM.

### 3.1 Electromagnetic forces

Electromagnetic force densities are generated in SRMs when the magnetic flux passes through the airgap. These forces are separated into two components: tangential forces and radial forces. The equations for these two forces are derived from Lorentz force law and are calculated using Maxwell Stress Tensor which can be seen below in (3.1) and (3.2).

$$F_t = \frac{1}{\mu_0} (B_r B_t) \quad (3.1)$$

$$F_r = \frac{1}{2\mu_0} (B_r^2 - B_t^2) \quad (3.2)$$

where  $B_r$  and  $B_t$  are the radial and tangential components of the magnetic flux density vector. For rotating machines, these forces can be modelled as force densities varying with time and space according to (3.3) and (3.4) :

$$p_t(t, \alpha) = \frac{B_r(t, \alpha) \times B_t(t, \alpha)}{\mu_0} \quad (3.3)$$

$$p_r(t, \alpha) = \frac{[B_r^2(t, \alpha) - B_t^2(t, \alpha)]}{2\mu_0} \quad (3.4)$$

where  $t$  is time and  $\alpha$  is angular position in degrees in the circumferential direction. The radial force density applied to the stator causes radial vibration of SRMs which is the main source of acoustic noise. To understand the behaviours and characteristics of the produced radial force densities, they are modelled with respect to time and position for identification of dominant temporal and spatial harmonics. The circumferential shape of a radial force density is classified according to spatial order  $\nu$ . Various spatial orders from -5 to +5 are shown in Fig 3.1. The sign of the spatial order is either negative or positive depending on the direction of rotation. As the absolute value of  $\nu$  increases, the number of bulges in the shape increases. The matching of spatial orders from the radial force density and the corresponding shape of vibration modes of an SRMs stator are responsible for resonance excitations.

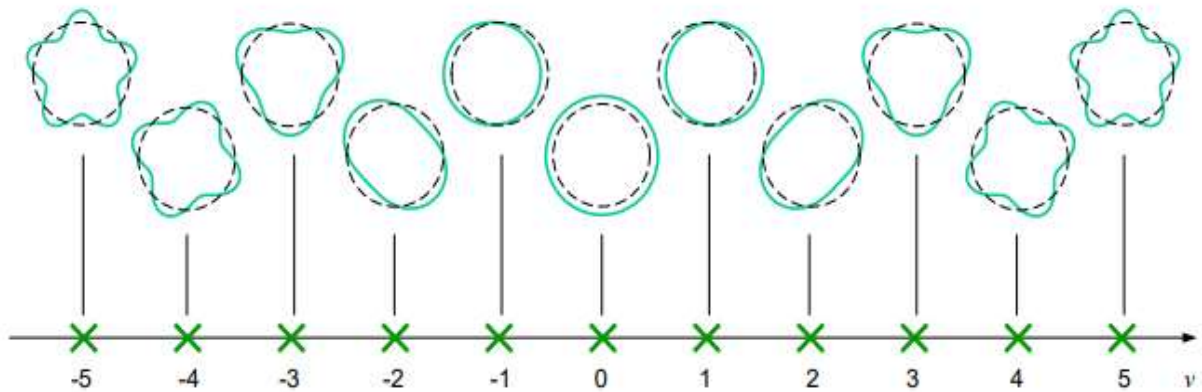


Fig. 3.1 Circumferential order relationship with shape [49]

Temporal harmonics are classified with temporal order  $u$ , and provide information regarding the circular motion of the radial force density wave along the stator's circumference, and the frequency of the spatial order. The temporal order is related to the mechanical frequency of the rotor as seen in (3.5) and is referred to as the forcing frequency in Hertz (Hz). The forcing frequency increases linearly with temporal order and rotor speed in revolutions per minute (rpm).

$$F_f = |u|f_{mech} = |u|\frac{rpm}{60} \quad (3.5)$$

The information contained within the spatial and temporal orders allows characteristics of a surface waveform to be analyzed. To explain, an example of a radial force density for a four phase 8/6 SRM is shown in Fig. 3.2.

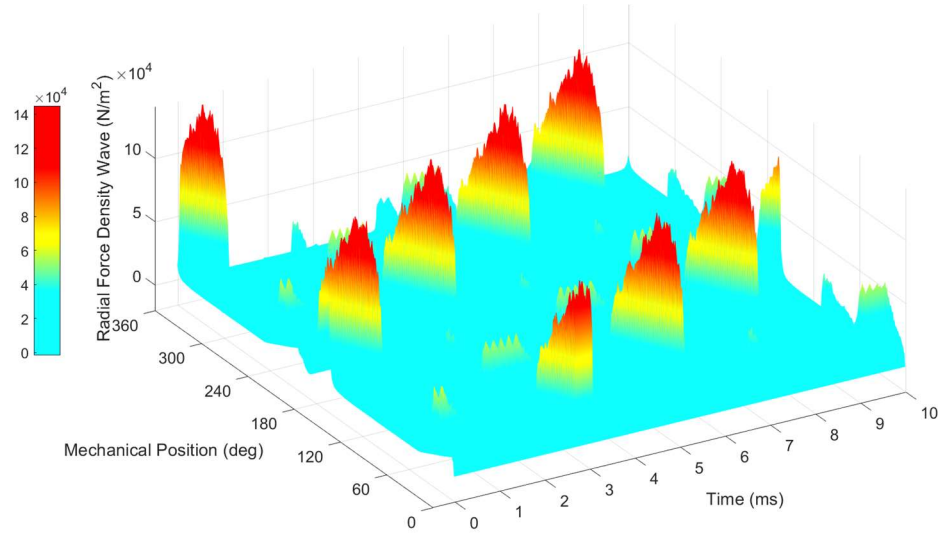


Fig. 3.2 Radial force density of a four phase 8/6 SRM

In this example, the rotor is moving in the CCW direction for one mechanical cycle. For one mechanical cycle, 8 radial force density peaks can be observed, one for each stator pole. These radial force densities produced by SRMs can be treated as time and space varying surface waveforms. For generalization, a surface wave can be described according to (3.6):

$$s(t, \alpha) = A \cos(2\pi u f_{mech} t + v\alpha + \varphi) \quad (3.6)$$

where  $A$  is the amplitude,  $f_{mech}$  is the mechanical frequency in Hz,  $t$  is time,  $\alpha$  is the angular circumferential position of the stator, and  $\varphi$  is the phase angle. Radial force densities can be modelled as a superposition of complex space and time varying surface waves according to their spatial and temporal order contents. These waveforms can be described according to (3.7):

$$s(t, \alpha) = \sum_{u=-\infty}^{\infty} \sum_{v=-\infty}^{\infty} [A_{u,v} \cos(2\pi u f_{mech} t + v\alpha + \varphi_{u,v})] \quad (3.7)$$

where  $A_{u,v}$  and  $\varphi_{u,v}$  are the amplitudes and phase angles for harmonics of each temporal order  $u$ , and spatial order  $v$ . By modelling the radial force densities in this manner, they can be decomposed into the series of cosine waves that contribute to the surface wave for their spatial and temporal harmonics. By conducting a 2D Fast Fourier Transform (FFT) on the radial force density waveform, the dominant harmonics are identified. A 2D FFT plot for one electrical cycle of a 4 phase 8/6 SRM is plotted in Fig.3.3.

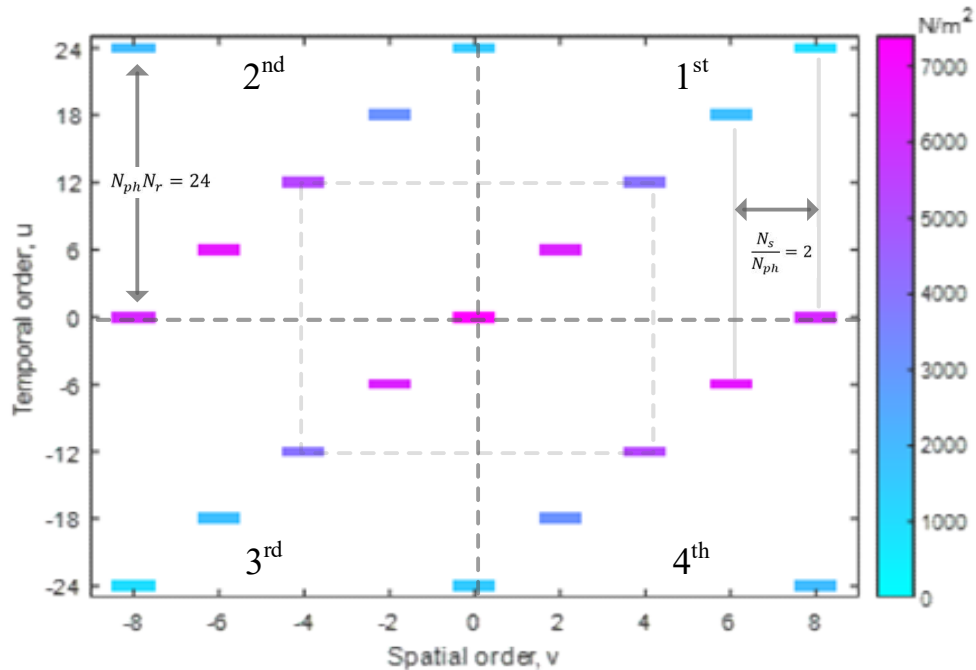


Fig. 3.3 Dominant radial force density harmonics for a four phase 8/6 SRM



The colour map is the radial force amplitude, in  $\text{N/m}^2$ , of the corresponding pressure waves. The temporal and spatial orders are symmetrically distributed in the four quadrants in Fig.3.3. These harmonics have half the amplitude of the corresponding surface wave in the time domain and the symmetry can be seen for the 1<sup>st</sup> and 3<sup>rd</sup> quadrants and 2<sup>nd</sup> and 4<sup>th</sup> quadrants. For example, the harmonic  $(u, v) = (6, 2)$  has a symmetric component  $(u, v) = (-6, -2)$  with the same amplitude. When spatial order  $v$  has the same absolute value  $|v|$ , the forcing waves have the same shape. When the forcing harmonics have the same temporal order absolute value  $|u|$ , they share the same forcing frequency. The  $(u, v) = (0, 0)$  harmonic refers to the DC component where  $u=0$  is a constant force applied to the stator and does not rotate.

The radial force density harmonic waveforms are rotating when they are applied to an SRM. The direction of rotation for the harmonics can be determined from the multiplication of the signs from the spatial and circumferential orders. For positive values, the rotational direction is negative or CW whereas negative values have a positive rotation or CCW. The directions are based on the rotation direction of the rotor. This is further explained in Fig. 3.4 for the rotation behaviours of harmonics in each quadrant based off a rotor rotating in the CCW direction with phase excitation in the CW direction.

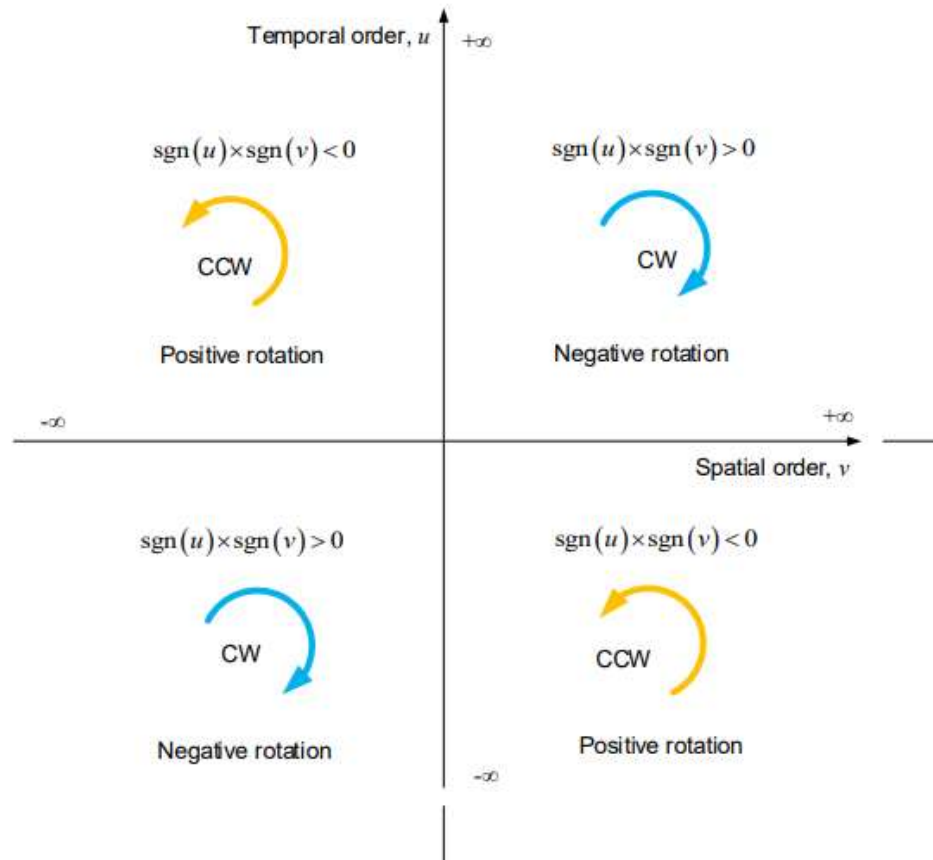


Fig. 3.4 Rotational directions of surface waves in all four quadrants [2]

The symmetric components are complex exponentials with positive and negative frequencies which are represented as spirals rotating in a complex plane (real and imaginary axis) [22]. Combining the symmetric components together cancels out the imaginary components and a surface wave that varies with time and position is the result. To illustrate, the symmetric components from Fig. 3.3 for  $v = \pm 6$  and  $u = \pm 18$  can be applied to (3.7).

$$\begin{aligned}
s_{18,6}(t, \alpha) &= \\
&\frac{A_{18,6}}{2} e^{j(2\pi * 18f_{mech}t + 6\alpha + \varphi_{18,6})} + \frac{A_{-18,-6}}{2} e^{-j(2\pi * 18f_{mech}t + 6\alpha + \varphi_{18,6})} \\
&= \frac{A_{18,6}}{2} [\cos(2\pi * 18f_{mech}t + 6\alpha + \varphi_{18,6}) \\
&\quad + j \sin(2\pi * 18f_{mech}t + 6\alpha + \varphi_{18,6})] \\
&\quad + \frac{A_{-18,-6}}{2} [\cos(2\pi * 18f_{mech}t + 6\alpha + \varphi_{-18,-6}) \\
&\quad - j \sin(2\pi * 18f_{mech}t + 6\alpha + \varphi_{-18,-6})] \\
&= A_{18,6} \cos(2\pi * 18f_{mech}t + 6\alpha + \varphi_{18,6})
\end{aligned} \tag{3.8}$$

where the amplitudes  $\frac{A_{18,6}}{2}$  and  $\frac{A_{-18,-6}}{2}$  are equal and the phase angles are assumed zero for simplification. For this example,  $+6\alpha$  indicates the force density waves travels in a negative direction with respect to the  $\alpha$ -axis, or decreases as time increases, to hold true the  $18f_{mech}t + 6\alpha = 0$  condition and results in the surface wave rotating in the clockwise direction with respect to the stator circumference [22]. For further understanding, an example surface wave with rotation characteristics can be seen in Fig. 3.5. This standing wave corresponds to  $A_{2,2} \cos(2\pi * 2t + 2\alpha)$ . As time increases from  $t_1$ - $t_2$ - $t_3$ , it can be observed that the peaks move in the negative direction of the  $\alpha$ -axis, which corresponds to CW rotation along the stator's circumference. Surface waves from harmonics in quadrants 1 and 3 would have similar characteristics to the behaviour of the surface wave presented in Fig. 3.5.

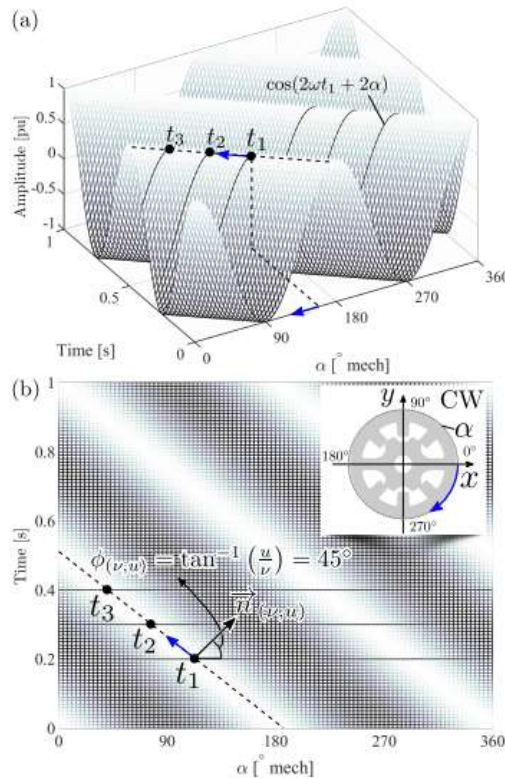


Fig. 3.5 First and third quadrant radial force density surface wave characteristics traveling in the CW direction of the stator circumference [22]

For each SRM design, certain patterns are expected for the dominant harmonics. Specifically, the number rotor and stator poles along with the number of phases are important factors when analyzing the dominant harmonics. The number of rotor poles per phase, or magnetic poles, will display the lowest spatial order of the radial force waves. For Fig. 3.3 the four phase 8/6 SRM has 2 magnetic poles and consequently the lowest spatial order is  $\nu = 2$ . The lowest temporal order is equivalent to the number of rotor poles, and rotates in the same direction as phase excitation. Additionally, the number of rotor poles and number of phases impacts the temporal order patterns based on the number of strokes

per cycle. For example, the four phase 8/6 SRM will have a pattern of every 24<sup>th</sup> temporal order for a given spatial order, this is due to  $N_r N_{ph} = 6 \times 4 = 24$ .

Generally, as temporal order increases, the amplitude of the harmonic decreases. To illustrate, the magnitudes of the first 4 spatial order harmonics seen from Fig. 3.3 are plotted in Fig. 3.6. These magnitudes correspond to the harmonics  $(u, v) = (0,0), (6,2), (12,4)$ , and  $(18,6)$ . This characteristic makes the overlap of lower stator natural frequencies a problem when it comes to SRM design, which will be discussed in Section 3.3.

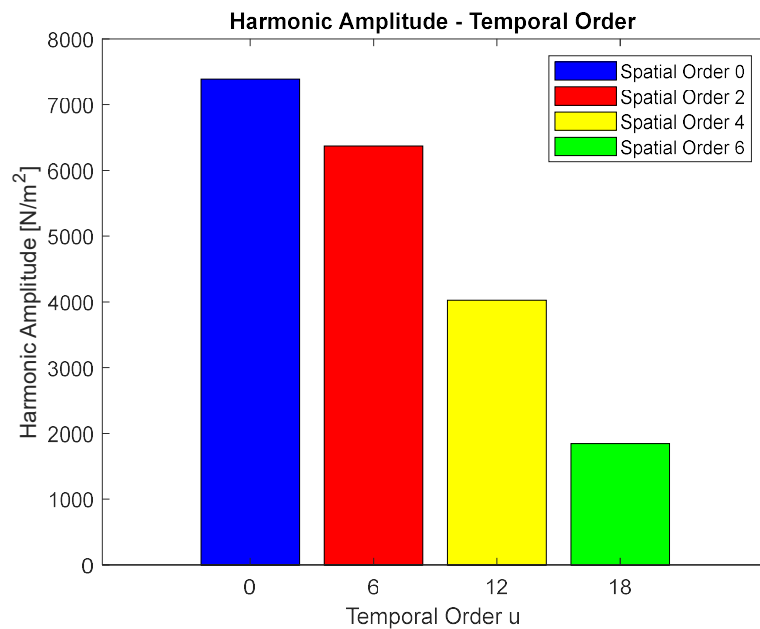


Fig. 3.6 Radial force density harmonic amplitudes vs. temporal orders

### 3.2 Mechanical Vibrations and Acoustic Noise

The fundamentals of vibrations and acoustic noise are outlined in this section. In particular, the fundamentals of vibrating systems along with the calculations of natural

frequencies and dynamic responses are discussed. Additionally, the simulation modelling considerations that best describe SRMs are outlined.

### 3. 2.1 Vibration Fundamentals:

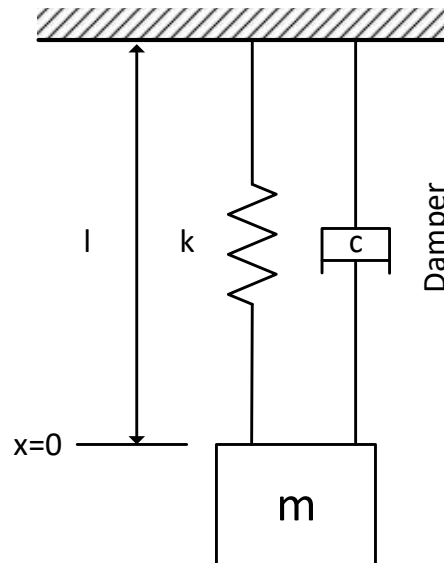


Fig. 3.7 Spring mass damper system

A simplified spring mass damper system can be seen in Fig. 3.7. In general, damped spring systems can be described according to (3.9), where  $m$  is the mass,  $c$  is the damping coefficient, and  $k$  is the stiffness of the spring.

$$m\ddot{x}(t) + c\dot{x}(t) + kx(t) = 0 \quad (3.9)$$

For FEA natural frequency analysis, this same system is analyzed without the damping factor consideration. In other words, for free undamped vibrations, a system can be described as (3.10):

$$[M]\{\ddot{u}\} + [K]\{u\} = \{0\} \quad (3.10)$$

where  $M$  and  $K$  are the mass and stiffness matrices, and  $\ddot{u}, u$  are acceleration and displacement, respectively. With the assumption of harmonic motion, displacement is described according to (3.11):

$$\{u\} = \{\phi_i\} \sin(\omega_i t + \theta_i) \quad (3.11)$$

The eigenvalue equation for the system then becomes (3.12):

$$([K] - \omega_i^2 [M])\{\phi_i\} = \{0\} \quad (3.12)$$

where  $\omega_i$  is the natural circular frequency and  $\phi_i$  is the eigenvector for mode shapes. This equation is solved by finding the determinants of the system, which results in solving for eigen value natural circular frequencies and corresponding eigenvector mode shapes. The natural frequency for a calculated mode can then be calculated by (3.13):

$$f_i = \frac{\omega_i}{2\pi} \quad (3.13)$$

When a periodic force,  $F$ , is applied to a system, the system becomes a driven damped harmonic oscillator. A picture of this can be seen in Fig. 3.8. To consider the dynamic harmonic response of the system, FEA governing equations expand upon (3.10) to include the damping matrix  $C$ , and the harmonic oscillating force as shown in (3.14):

$$[M]\{\ddot{u}\} + [C]\{\dot{u}\} + [K]\{u\} = \{F\} \quad (3.14)$$

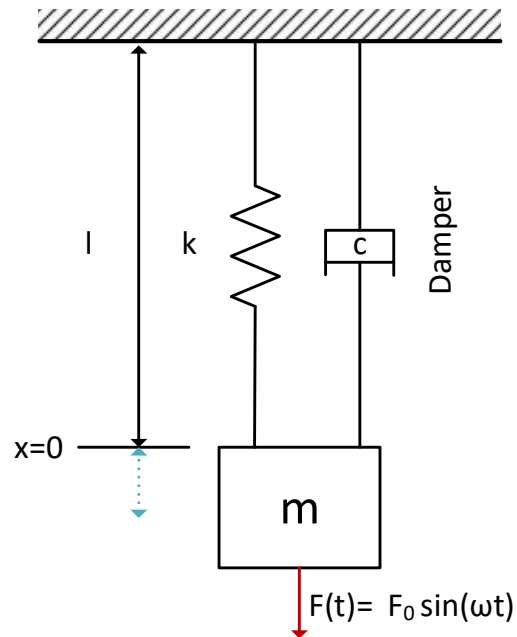


Fig. 3.8 Forced vibration damped system

For application to SRMs, the motor structure is considered as a forced damped spring mass system for modelling purposes. The electromagnetic force density harmonics from the motors tangential and radial forces can be considered as an applied periodic force to the SRM structure according to (3.15):

$$F(t) = F_0 \sin(\omega_f t) \quad (3.15)$$

where  $F_0$  is the force amplitude  $\omega_f$  is the angular forcing frequency and  $t$  is time. Additionally, forced damped spring mass systems expand upon (3.15) and are expressed as (3.16):



$$\ddot{x}(t) + 2\zeta\omega_n\dot{x}(t) + \omega_n^2x(t) = \frac{F_0}{m}\sin(\omega_f t) \quad (3.16)$$

where  $x(t)$  is the displacement of the mass,  $\omega_n$  is the natural frequency of the mechanical system,  $\omega_f$  is the forcing frequency of the harmonic and  $\zeta$  is the damping ratio.

### 3.2.2 Mode Shapes

The assembly of an SRM can have complex structures when including the stator, windings, housing and endcaps. These components will have many vibration modes that are free to deform in the axial, and circumferential directions. However, the characteristics of the electromagnetic force densities from the motor can excite vibration modes of specific components, in particular the stator and housing. To simplify the mode shapes of these structures, the stator and housings are modelled as cylindrical shells with mode shapes classified in relationship to the circumferential (*circ*) and axial (*ax*) directions. The range of circumferential mode shapes from *circ*= 0 to *circ*= 5 for a cylindrical shell are shown in Fig. 3.9:

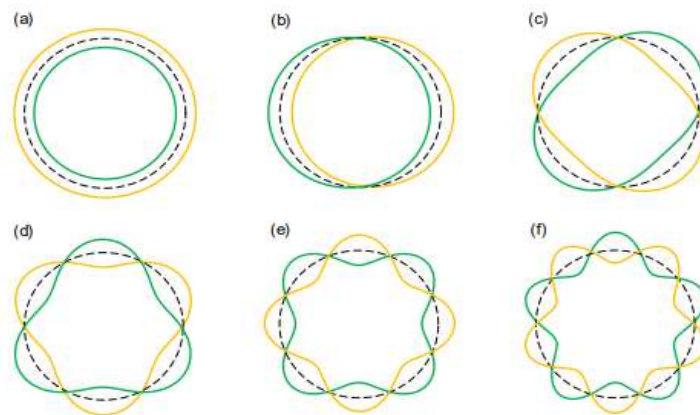


Fig. 3.9 Circumferential mode shapes for a cylindrical shell for *circ*=(a) 0 (b) 1 (c) 2 (d) 3 (e) 4 and (f) 5 [22]

The axial orders of cylindrical shell vibration modes are similar to the characteristics of a straight beam. The combination of circumferential order and axial order are represented using a 3D model of cylindrical shell as shown in Fig. 3.10.

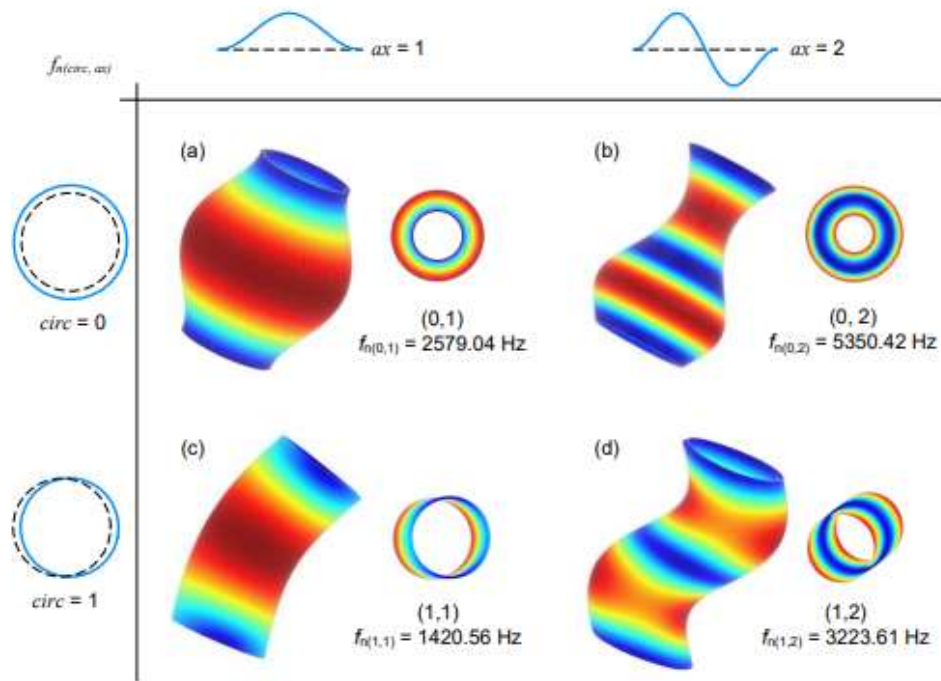


Fig. 3.10 Mode shapes of a cylindrical shell for circumferential and axial orders [50]

The classification of *circ* and *ax* order combinations allows for the identification of specific natural frequencies  $f_{n(circ,ax)}$ . The natural frequencies characteristics are dependent on the component's materials and connection between the components. Specifically, the mode shape of a cylindrical shell relies on the type of support constraints. Depending on an SRMs configuration, the stator can be clamped, supported or free on either end. The induced vibrations in the radial direction of an SRM create moments at the

stator-housing or stator-faceplate interfaces, which can rotate in one direction, but cannot translate in any direction. Clamped constraints can hold the moments created by the surface displacements and not allow rotation at the connection point whereas supported constraints do not resist moments but can resist horizontal and vertical forces. A free constraint means one end of the stator does not have a supported or clamped constraint.

### 3.3 Resonance Excitation

Identifying both the vibration modes of the SRMs structural components and the harmonic characteristics of the radial force density wave helps in identifying possible resonance excitations. Resonance excitation can occur in SRMs when a vibration mode shape matches the spatial order shape of the radial force density harmonics. Specifically, resonance excitation occurs when the circumferential order of a vibration mode matches the spatial order of the radial force density and the temporal order forcing frequencies overlap closely with the natural frequency of that vibration mode shape.

To illustrate, a four phase 8/6 SRM at 2000 rpm is used as an example. For this SRM, the vibration mode 2 for the stator is approximately 1845 Hz. From a 2D FFT seen in Fig.3.3, the spatial order  $\nu = 2$  has temporal harmonics every 24<sup>th</sup> order ( $N_r N_{ph}$ ) starting from 6 ( $N_r$ ). This pattern contains the 54<sup>th</sup> harmonic, which for an operating speed of 2000 rpm has a forcing frequency of 1800 Hz according to (3.5). This therefore overlaps closely with the natural frequency of mode 2 for the stator. This means at the 54<sup>th</sup> temporal order forcing frequency, there is a close overlap with the natural frequency of the stator along with a matching of spatial and circumferential order shapes. This is where resonance

excitation occurs and is the source of excessive and unwanted acoustic noise for SRMs. A visual representation of resonance overlap is outlined in Fig. 3.11.

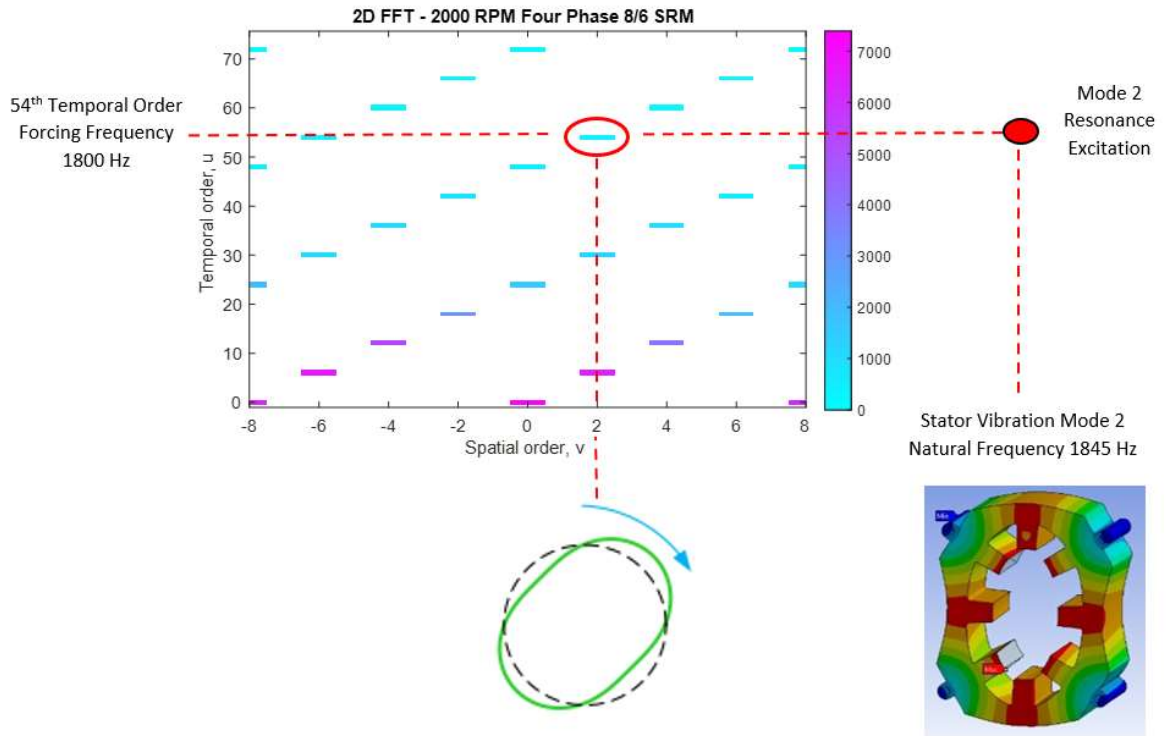


Fig. 3.11 Radial force density harmonics resonance excitation of vibration mode 2 for a four phase 8/6 SRM

When conducting acoustic noise analysis for an SRM design, the pole configuration will determine the lowest spatial mode for resonance excitation possibilities. For example, a three phase 24/16 SRM will have the multiples of 8 for the spatial orders according to  $N_s/N_{ph}$  which can be seen in Fig. 3.12. Generally, the higher the vibration mode, the higher the natural frequency. This means higher vibration modes will be harder to excite for the same speed as their natural frequencies will be very high. To minimize resonance

excitation, higher stator pole/phase ratios are desired, as in the 24/16 design. This will also increase the fundamental frequency and the dimensions of the motor. For all internal rotor SRMs, mode 0 will exist which is commonly referred to as the breathing mode due to expansion and contraction behaviour.

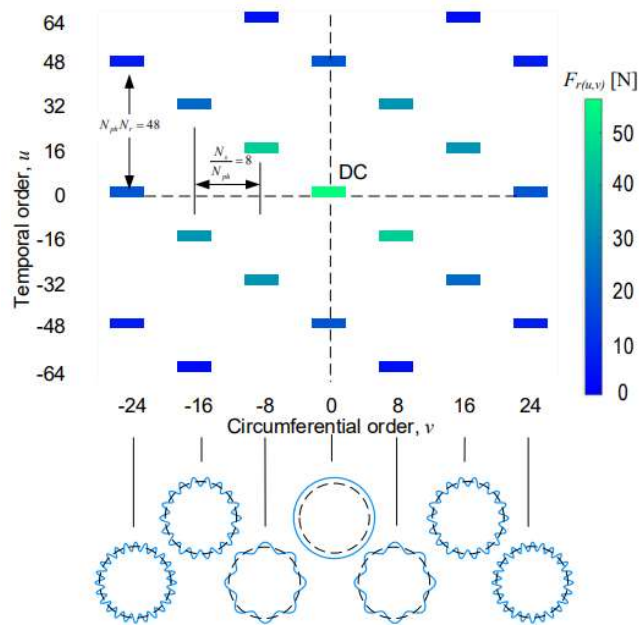


Fig. 3.12 Radial force density harmonics for a 24/16 SRM [50]

### 3.4 Mechanical Modelling Considerations

The accuracy of vibration and acoustic noise simulations depend on an accurate mechanical model. To ensure highest possible accuracy, detailed 3D mechanical models need to be designed to replicate as close to an actual prototype SRM as possible. This requires the use of accurate connections of components including the stator, the windings,

the housing and any endplate or endcaps of the SRM system for natural frequency calculation.

For accurate estimation of stiffness, small gaps are modelled between the bolt connections of components. For example, the bolt connections between the housing and endcaps have a 2mm gap where only the bolt faces are in contact with the end plate. This is to replicate reality, where only the bolt interfaces will replicate a bonded contact and not the entire face of the housing-endplate connection. A view of the contacts used for an SRM assembly is shown in Fig. 3.13.

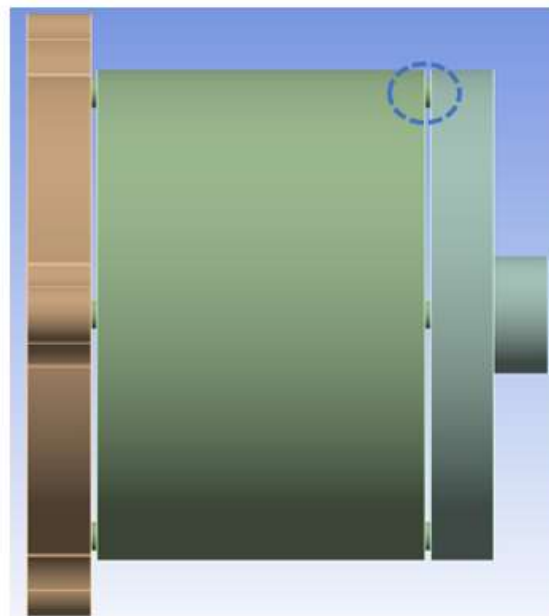


Fig. 3.13 Bolts contacts used in mechanical modelling of connections for SRM assemblies

Additionally, the contact between the stator and housing is a critical aspect. For SRMs two common practices are used to assemble these components, bolted or interference press

fit. The bolt contacts allow for easier motor disassembly from the housing, and each stator lamination is also bolted together. The interference fit is assembled by heating the housing for expansion before installing the stator core by press fit. For interference fit assemblies, the stator laminations can use bond coating substances, such as SURALAC™ 9000 by Cogent, to bond the lamination sheets together, which reduces the vibration of the stator core and eliminates the need for bolts or welds between laminations [2].

The windings have lumped mass effect on the stator poles including stiffness and damping. The coil windings geometry is therefore modelled accurately for correct volume and mass. Additionally, the coils must be modelled as a solid component, otherwise, excessive, and unrealistic natural frequencies will be calculated for each individual coil component as depicted in Fig. 3.14.

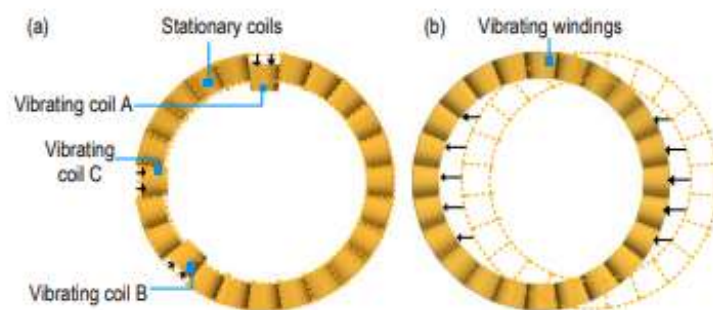


Fig. 3.14 Vibration modes of individual coils vs. combined windings [50]

In reality, only the coils of the same phase will be connected, but for 3D modelling purposes they are all assumed to be integrated and will therefore make the coils vibrate as a whole instead of individually. For computation simplicity, small, complicated geometries on the

housing and endcaps such as cooling inlets/outlets are removed as they require much finer mesh and increase computation time significantly. Additionally, the mass and stiffness of the design are the most important properties for the accuracy of the model, so the main dimensions and masses of the housings and endcaps need to be kept the same for most accurate results.

### **3.5 Damping Ratio Losses**

The calculation of the modal damping ratio  $\zeta$  is of particular importance for modelling considerations in SRMs. As the system vibrates from the induced electromagnetic forces, a portion of the mechanical energy is lost due to the damping of the structure. This dissipation of energy is referred to as damping loss and is broken down into three subcategories: structural damping, joint damping and acoustic damping loss. The structural loss can be considered as a type of hysteresis loss which changes with material dimensions and geometries. The joint damping loss comes from the connections and interfaces between components in the system and the acoustic damping loss comes from a radiation loss from the SRM surfaces to the surrounding air.

For NVH modelling, the components considered are the stator, windings, housing, and endcaps. The rotor, shaft and rotating inner components are not used for mechanical analysis as the vibration of the stator and housing is the major source of acoustic noise for internal rotor SRMs [2]. The connections between components along with the damping losses are outlined in Fig. 3.15 for an experimental test setup of an SRM [2].



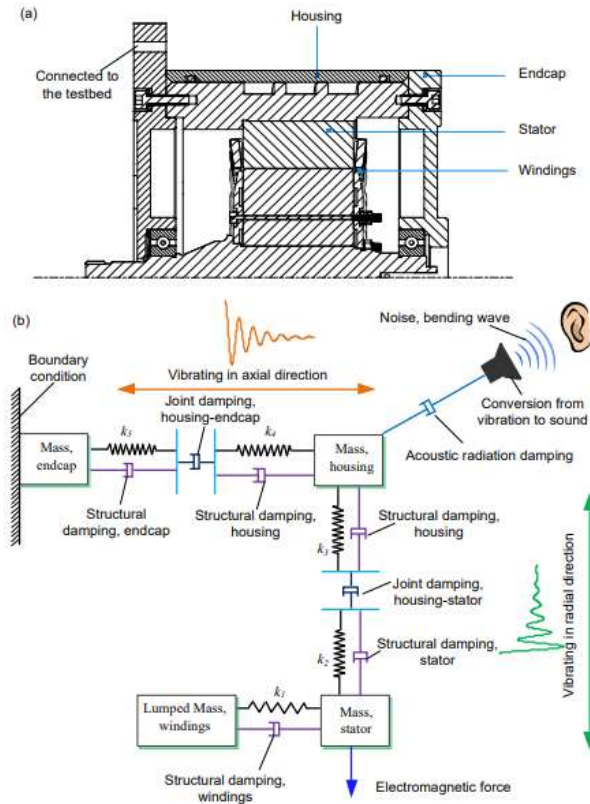


Fig. 3.15 (a) Assembly connections for an SRM and (b) system damping losses [2]

For numerical modelling of vibrations and acoustic noise in the FEA simulations, the modal damping ratio used is estimated using the natural frequencies of excited modes. The damping ratio is estimated according to (3.14) where  $f_{circ}$  is the natural frequency of the stator circumferential mode that is excited. If multiple modes are excited in the acoustic noise simulation, multiple damping ratios are considered for each natural frequency that is excited.

$$\zeta_{circ} = \frac{1}{2\pi} (2.76 \times 10^{-5} f_{circ} + 0.062) \quad (3.14)$$

The damping ratio consideration is an important factor in the vibration analysis as without including damping ratios, no losses are assumed and estimated values can be much larger. Additionally, slight changes in the damping ratio can also result in large differences in results. For example in [50], the vibration analysis for a 24/16 SRM was conducted using damping ratios of 0.02 and 0.06 and results showed large differences in the calculated surface displacements of the housing. The most accurate estimation of damping ratios would be obtained by conducting an impact hammer test on a SRM setup. An impact hammer modal test would show natural frequency spikes along with the decay rates for specific excitations to obtain specific damping ratios.

### **3.6 Acoustic Noise Modelling**

Sound is referred to as a mechanical pressure wave that propagates through a medium, like air, and causes disturbances throughout the medium until it reaches an observer. The speed at which sound propagates depends mostly on the physical characteristics of a particular medium. For all NVH analyses conducted for SRMs, this medium is air which has a speed of sound of 343 m/s at room temperature. Sound is referenced in acoustic pressure in Pascals and is often measured using decibels. A visualization of sound propagating through a medium can be simplified by visualizing uniform beads attached to springs as in Fig. 3.16.

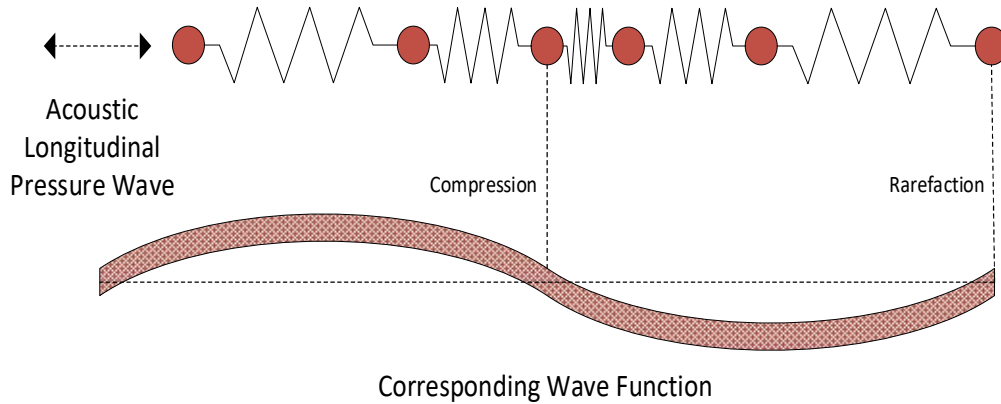


Fig. 3.16 Longitudinal acoustic pressure wave visualization

Noise is defined as unwanted sound. Therefore, the analysis of acoustic noise for SRMs implies unwanted sound produced by the motors. Acoustic noise analysis itself is a special type of fluid analysis. In three dimensions, the wave equation used for sound is defined according to (3.15):

$$\nabla^2 p = \frac{1}{c^2} \frac{\partial^2 p}{\partial t^2} \quad (3.15)$$

where  $p$  is pressure,  $c$  is the speed of sound,  $t$  is time and  $\nabla$  is the Laplacian operator which is defined as (3.16):

$$\nabla^2 p = \frac{\partial^2 p}{\partial x^2} + \frac{\partial^2 p}{\partial y^2} + \frac{\partial^2 p}{\partial z^2} \quad (3.16)$$

To simplify, the one-dimensional solutions satisfying the sound equation are complex waves according to (3.17), where  $A$ ,  $k$  is any real number and  $v$  is wave speed.

$$p(\vec{r}, t) = Ae^{ik(x-vt)} \quad (3.17)$$

The FEA software's involved in the calculation of acoustic noise for SRMs use the fluid equations to solve for various analysis such as sound pressure level, sound power level and sound intensity. For SRMs, noise is a result of vibrations from the motors surface which cause small fluctuations in the surrounding air. Measurements can be made based on proximity and location from the vibrating source and quantified as Sound Pressure Level (SPL) or as an energy of sound rate emitted by the source as Sound Power Level (SWL). SPL is defined according to (3.18) where  $P$  is acoustic pressure and  $P_{ref}$  is the referenced pressure both in Pascals (Pa). Typically,  $P_{ref}$  is 20  $\mu$ Pa for and the SPL is measured in decibels (dB).

$$SPL = 20\log\left(\frac{P}{P_{ref}}\right) \quad (3.18)$$

Additionally, sound power level, SWL, is defined according to (3.19) where  $W$  is sound power and  $W_{ref}$  is the referenced sound power both in Watts (W). Typically,  $W_{ref}$  is  $10^{-12}W$  and the SWL is also measured in dB.

$$SWL = 10\log\left(\frac{W}{W_{ref}}\right) \quad (3.19)$$

Acoustic noise can be difficult to quantify without hearing the produced sounds. To provide an interpretation of SPL, Table. 3.1 presents the calculated sound pressure levels, along with the sound pressure and sound intensity from commonly heard sounds.

Table.3.1 Reference sound pressure levels, sound pressures and sound intensities [51]

Noise sources and distance measured	Sound Pressure Level (SPL)	Sound Pressure	Sound Intensity
Jet aircraft, 50m	140 dB	200 Pa	100 W/m <sup>2</sup>
Chainsaw, 1m	110 dB	6.3 Pa	0.1 W/m <sup>2</sup>
Diesel truck, 10m	90 dB	0.63 Pa	0.001 W/m <sup>2</sup>
Curbside of high traffic road, 5m	80 dB	0.2 Pa	0.0001 W/m <sup>2</sup>
Vacuum cleaner, 1m	70 dB	0.063 Pa	0.00001 W/m <sup>2</sup>
Conversational speech, 1m	60 dB	0.02 Pa	0.000001 W/m <sup>2</sup>
Quiet library	40 dB	0.002 Pa	0.00000001 W/m <sup>2</sup>
Hearing threshold	0 dB	0.00002 Pa	0.000000000001 W/m <sup>2</sup>

To analyze the SPL or SWL produced by an SRM, many features of an acoustic environment need to be considered. Firstly, an acoustic near field needs to enclose the assembly components of the SRM. The near field is modelled as a surrounding sphere which will be meshed appropriately depending on desired frequency spectrums. The meshing specifications will be outlined in detail in section 3.8. The size of the near field is important for accurate simulations. Specifically, the distance from the SRM housing to the edge of the near field should be at least one wavelength according to the largest wavelength desired in the analysis. The largest wavelength is calculated based on the minimum frequency simulated according to (3.20), where  $\lambda$  is the wavelength,  $c$  is the speed of sound in air and  $f_{min}$  is the minimum simulated frequency.

$$\lambda = \frac{c}{f_{min}} \quad (3.20)$$

Additionally, the acoustic environment needs a radiation boundary defined to determine the acoustic far-field. As the acoustic near field will be filled with finite elements, the far-field will be defined with infinite elements. Infinite elements have an exponential term in its shape function which is best to describe the unbounded property of air [51]. Lastly, the vibrating surfaces of the assembly are coupled with an interface between the structural and acoustic environment. The acoustic environment features can be visualized as in Fig.3.17:

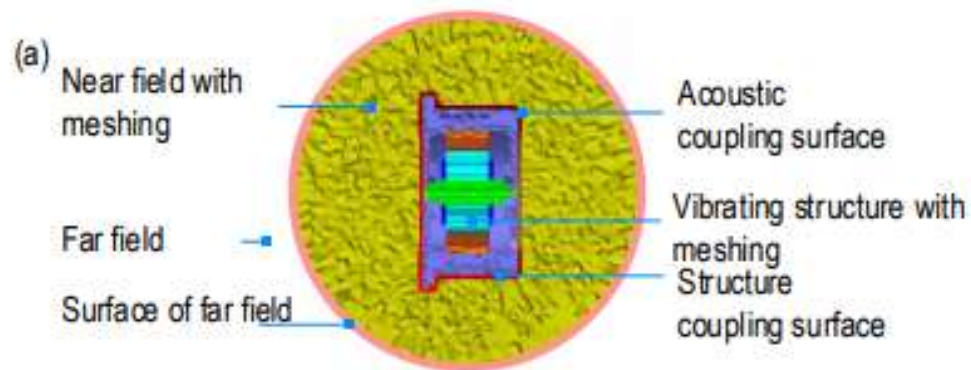


Fig. 3.17 Acoustic environment interface [50]

Once the required boundary conditions are set up, virtual microphones can be placed in various locations to measure SPL. The positions of the microphones can be placed according to industry standards such as ISO 3744, where 20 microphones are positioned as seen in Fig. 3.18. The combinations of the calculated SPL from the surrounding microphones cannot be directly summed together as sound pressure level is measured in decibels on a logarithmic scale. Therefore, for total SPL calculation (3.21) is used for multiple frequencies where  $SPL(f)$  is the SPL calculated at a specific frequency.

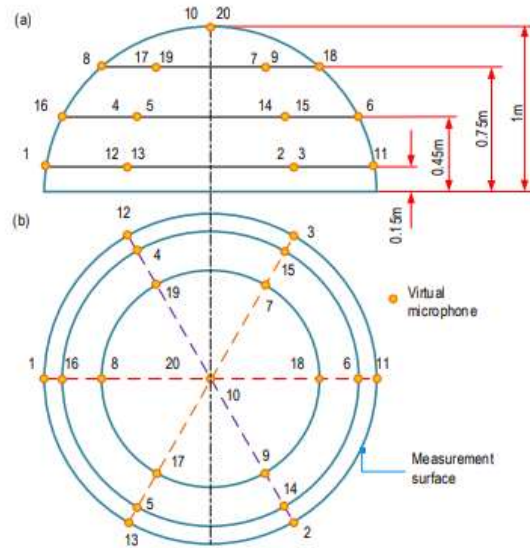


Fig. 3.18 Virtual microphone locations according to ISO 3744 standard [50]

$$SPL_{total} = 10 \log_{10} \left[ \sum 10^{\frac{SPL(f)}{10}} \right] \quad (3.21)$$

### 3.7 Multiphysics FEA Network

To accurately model acoustic noise produced by SRMs, multiple analyses need to be coupled together. Specifically, three main analytical models are used: an electromagnetic model, a structural model and an acoustic model. The electromagnetic model simulates the transient behaviours of SRMs to generate the electromagnetic forces produced by the motor. The structural model uses the components of the motor assembly and their respective material properties to calculate the natural frequencies of the system. In order to create the forced vibration response of the SRM system, the electromagnetic simulation needs to be coupled with the structural components. The electromagnetic forces are coupled

in an FEA environment and mapped to the influenced components of the SRM. For internal rotor SRMs the nodal forces are mapped to the stator as the forces are directly applied to the stator teeth. The superposition of natural frequency calculations with the harmonically varying nodal force loads from the EM simulation generate a forced vibration response of the stator, housing, and assembly components. The generated velocities of each structural component serve as the input to the acoustic model. The velocities are mapped to the components in the acoustic FEA environment, where the acoustic near field and acoustic radiation boundaries are setup. Once these FEA simulations are coupled as outlined, the estimation of acoustic noise for SRMs can be analyzed. A general overview of the connections between FEA modules is shown in Fig. 3.19. The acoustic noise modelling process is facilitated using connections in ANSYS Workbench modules. These modules include Maxwell 2D, Modal, Harmonic Response and Harmonic Acoustics which are outlined in the legend of Fig. 3.19.

The FEA multiphysics flow in Fig.3.19 starts with the 2D motor geometry, which is then exported to CAD design to replicate all of the involved motor assembly components. The 2D motor geometry and 3D CAD assembly serve as the initial inputs that start the whole FEA flow process. In addition to FEA simulations an additional step is involved in the acoustic noise analysis procedures [22, 50]. Once the electromagnetic simulation is concluded, the force density wave is exported to MATLAB for post processing. The characteristics of the electromagnetic forces are then decomposed using the 2D FFT analysis which was outlined in section 3.1. By identifying the spatial and temporal harmonic contents of the force waveform, the acoustic noise results can be verified and



further understood. Peaks in SRM sound pressure level results are cross verified to see if they match excited natural frequencies of an SRMs stator at dominant spatial and temporal orders that have the same shape and forcing frequencies. This extensive procedure allows for accurate acoustic noise modelling for SRMs. In addition, the analysis of electromagnetic force characteristics develops a better understanding of the underlying causes to acoustic noise and vibration issues that SRM designs may have.

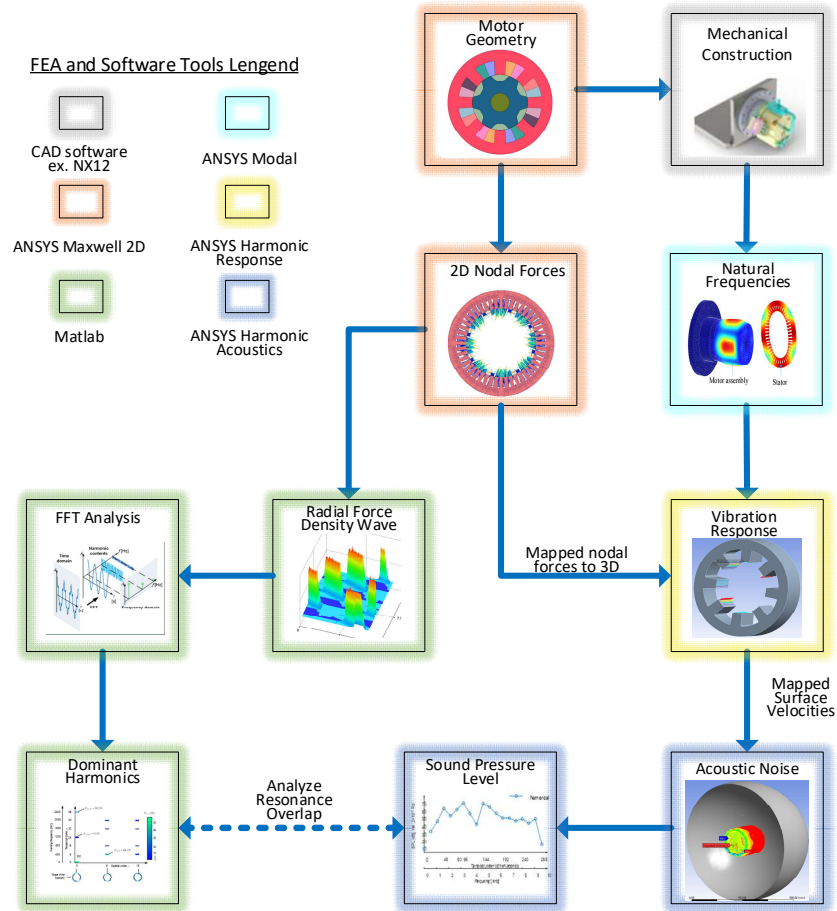


Fig. 3.19 Multiphysics FEA network of connections for SRM acoustic noise analysis

### 3.8 FEA Module Considerations

Each FEA simulation requires unique setup considerations including geometry, environment, meshing and analysis settings. To further explain the considerations that are included in the acoustic noise FEA network, this section will outline important considerations for each major FEA module.

The electromagnetic 2D simulation serves as the dynamic numerical tool which allows a machine design engineer to analyze a design's performance. For the FEA toolchain the calculation of the nodal forces is the most important role for the electromagnetic simulation. The calculation of these nodal forces includes both tangential and radial forces as defined in (3.1), and (3.2). Although the simulation is analyzed in 2D, the capabilities of ANSYS Maxwell allow the nodal forces to be extrapolated and mapped to the 3D structural environment. An example of the nodal forces mapped to an SRM's stator teeth can be seen in Fig. 3.20.

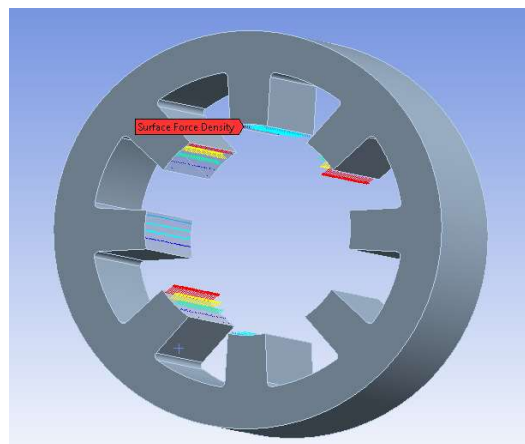


Fig. 3.20 Mapped 3D nodal forces to SRM stator teeth

Additionally, the meshing involved in the electromagnetic simulation is an important analysis consideration. Most importantly, fine, high quality mesh should be used in the active areas of an SRM design. These areas include the airgap, stator/rotor poles and boundary edges between components. The exact specifications of mesh sizing are outlined in [50], where the number of divisions for mesh elements and mesh element size are related to the airgap's circumferential and radial lengths along with the rotor and stator pole sizes. An extremely high-quality mesh has an ideal aspect ratio of 1, however the design engineer must make a judgment call considering computation cost for simulation time of the model. To decrease the computation cost, coarser sized mesh is used for areas furthest from the airgap, including the shaft and outer stator yoke. The important consideration is to have high quality mesh in the airgap region, while also keeping the aspect ratio of the mesh between 1-10. For an example 2D electromagnetic mesh, an 8/6 SRM meshed geometry can be seen in Fig. 3.21.

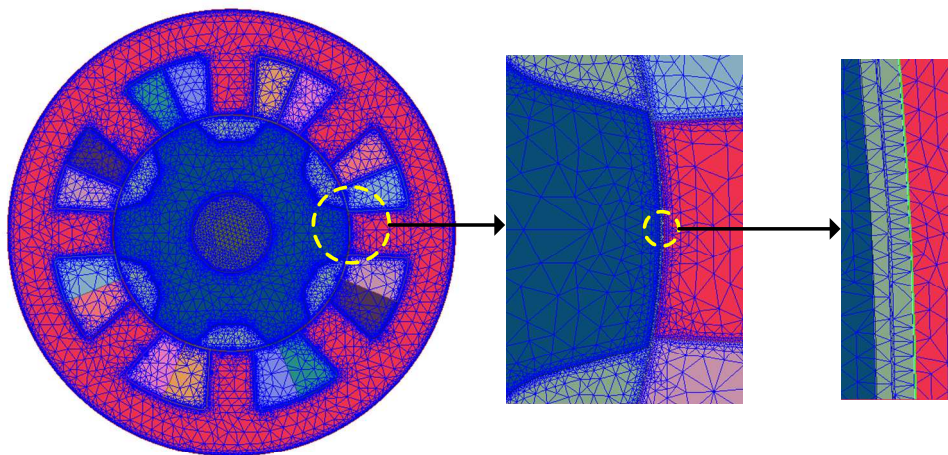


Fig. 3.21 2D electromagnetic meshing

The structural model used for natural frequency and vibration simulations requires a different set of meshing criteria. From [50], structural mesh is determined from the bending wavelength from the maximum frequency simulated along with the material properties of the components used. The required element size is expressed as (3.22):

$$\epsilon = \frac{1}{n} \times \lambda_b \quad (3.22)$$

where  $n$  is the number of elements per wavelength and  $\lambda_b$  is the bending wavelength. For linear element types  $n$  should be between 8 to 10 and for quadratic elements  $n$  should be 4 to 6. The bending wavelength is defined as (3.23):

$$\lambda_b = \frac{c_b}{f_{max}} \quad (3.23)$$

where  $f_{max}$  is the maximum frequency and  $c_b$  is the speed of the bending wave according to (3.24):

$$c_b = (1.8 \times c_L \times T_h \times f_{max}) \quad (3.24)$$

where  $T_h$  is the thickness of the housing and  $c_L$  is the speed of the longitudinal sound wave according to (3.25):

$$c_L = \left\{ \frac{E}{\rho \pi (1 - \nu^2)} \right\}^{0.5} \quad (3.25)$$

where  $E$  is the Young's Modulus,  $\rho$  is the density and  $\nu$  is the Poisson's ratio of the housing material. In addition to proper element size, the connections between components must be meshed appropriately for accurate results. For example, the element nodes at boundary conditions that are bonded together should match for best results Fig. 3.22 shows the stator pole/windings meshed interface.

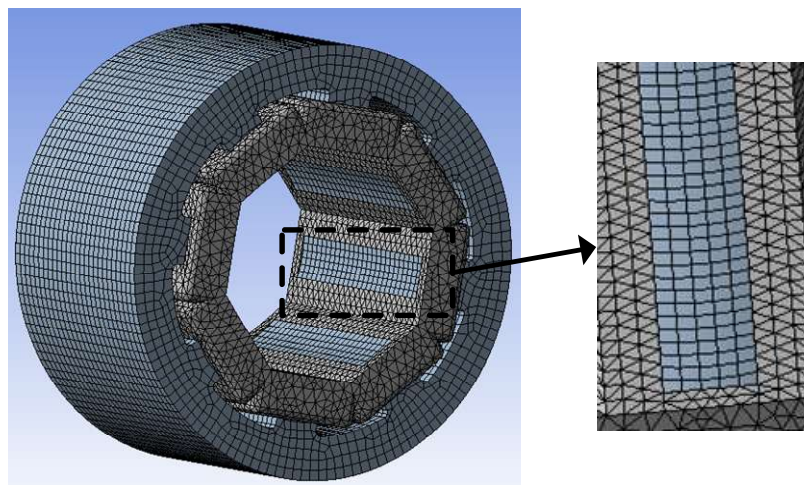


Fig. 3.22 Stator and windings mesh interface

The acoustic FEA domain needs specific meshing requirements based on the frequencies simulated. In particular, the acoustic noise simulations can be computationally expensive as meshing specifications need to meet requirements for both the minimum and maximum frequencies simulated. As explained in section 3.6, the near field minimum distance must be at least one wavelength thick for the largest wavelength (smallest frequency), but additionally the mesh element size must be fine enough to accurately capture the size of the smallest wavelengths (largest frequency). The element size is determined by (3.26):

$$\epsilon = \frac{c}{n f_{max}} \quad (3.26)$$

where  $c$  is the speed of sound and  $n$  is the number of elements per wavelength. Depending on the frequency range simulated, the computation time required to run the acoustic noise FEA analysis can vary drastically. To illustrate the extensive mesh element sizing required in the acoustic near field the mesh can be seen for an SRM model that simulated a range of frequencies from 700 Hz to 7500 Hz in Fig. 3.23:

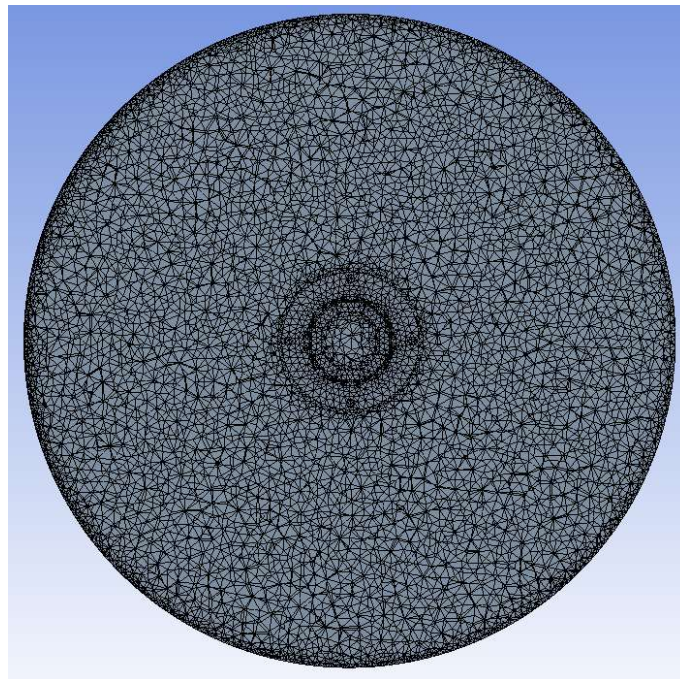


Fig. 3.23 Cross sectional view of the acoustic near field mesh

### 3.9 Experimental Validation of the Multiphysics Vibroacoustic Model

To validate the acoustic noise FEA multiphysics toolchain, a four phase 8/6 SRM was used for experimental results. The machine is rated at 5kW with a base speed of 6000 rpm,

and 300 V DC link voltage. The experimental setup includes an induction motor running in speed mode for the applied load. The inverter used is a four-phase asymmetric bridge converter. For acoustic measurement, a microphone is placed 1m directly above the motor in the radial direction, aligned with one of the mounted bolts as seen in Fig.3.24. The sound was recorded using an audio interface, which then uses a MATLAB algorithm to acquire the acoustic noise generated. A Fourier transform is applied to the measured sound pressure to obtain the results in the frequency domain and converts the amplitudes of the harmonics into decibels (dB) according to (3.27), where  $p_{ref}$  is 20 uPa and  $p$  is the measured sound pressure.

$$SPL = 20 \log_{10} \left( \frac{fft(p)}{p_{ref}} \right) \quad (3.27)$$

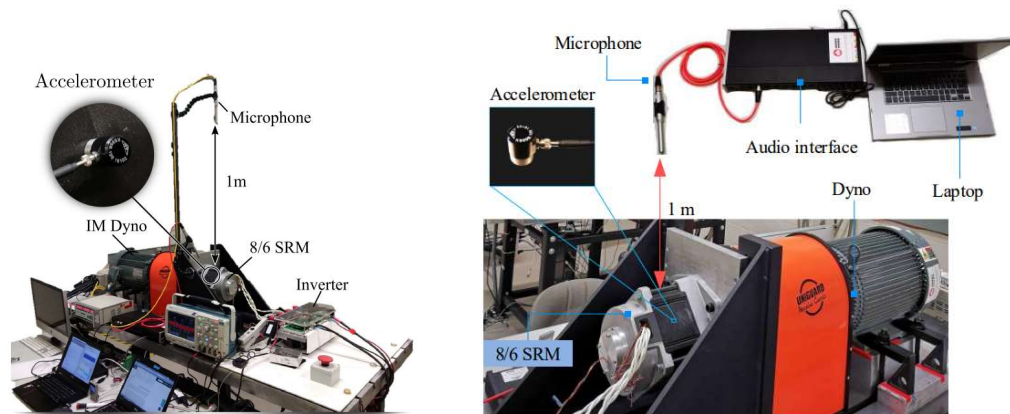


Fig. 3.24 Experimental setup for acoustic noise measurement of the four phase 8/6 SRM

[22,50]

The stator-housing assembly is modelled to replicate the experimental setup for proper calculation of the systems natural frequencies. An exploded view of the assembly design can be seen in Fig. 3.25.

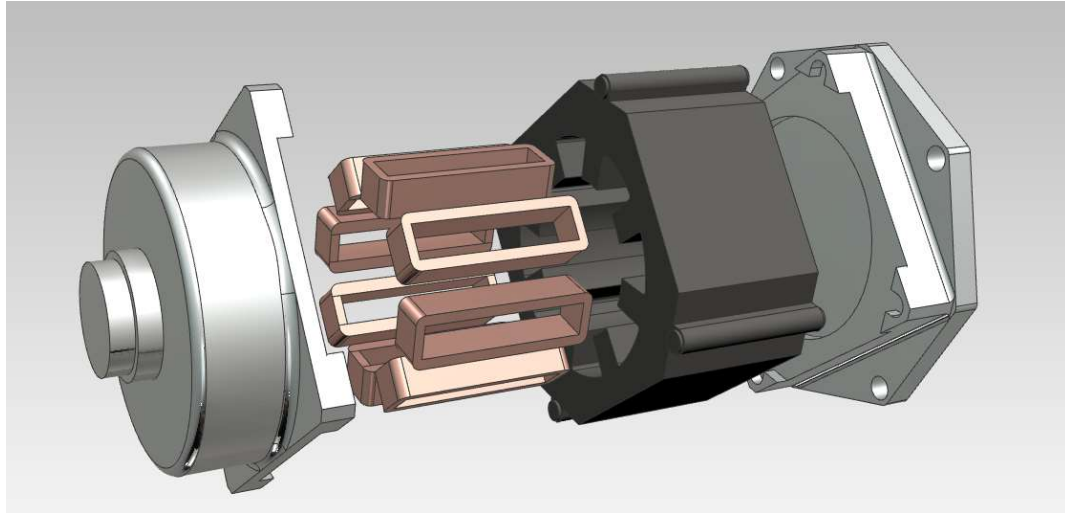


Fig. 3.25 Stator-housing assembly CAD model for the 8/6 SRM

The critical natural frequencies of this motor correspond to the shapes of the stator's vibration modes. Specifically for this motor, the natural frequency of mode shape 2 is of particular importance. This is because the four phase SRM contains two pole excitations for one phase, which results in a dominant oscillating spatial order 2 radial force wave. The numerical FEA and experimental stator vibration mode 2 natural frequencies match very well. From FEA analysis mode (2,1) was found to be 1845.8 Hz and mode (2,2) was found to be 2451 Hz which compare well to the experimentally found mode (2,1) frequency of 1884 Hz and mode (2,2) frequency of 2435 Hz. These two stator mode shapes from FEA analysis are outlined in Fig. 3.36.



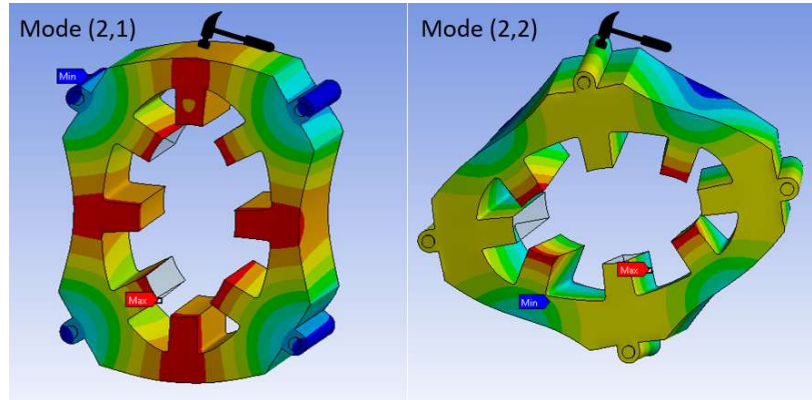


Fig. 3.26 FEA calculated vibration mode's for the 8/6 SRM

The vibration modes were experimentally found from an impact hammer test. The experimental setup used an accelerometer mounted on the outer surface of the stator to measure the response of the surface acceleration and can be seen in Fig 3.24. When the stator is struck in the middle of the stator lamination, a spike appears for mode (2,1) and a spike in the hammer test appears for mode (2,2) when the stator is struck on the bolted corner. The corresponding frequency-domain response of the hammer test can be seen in Fig 3.27.

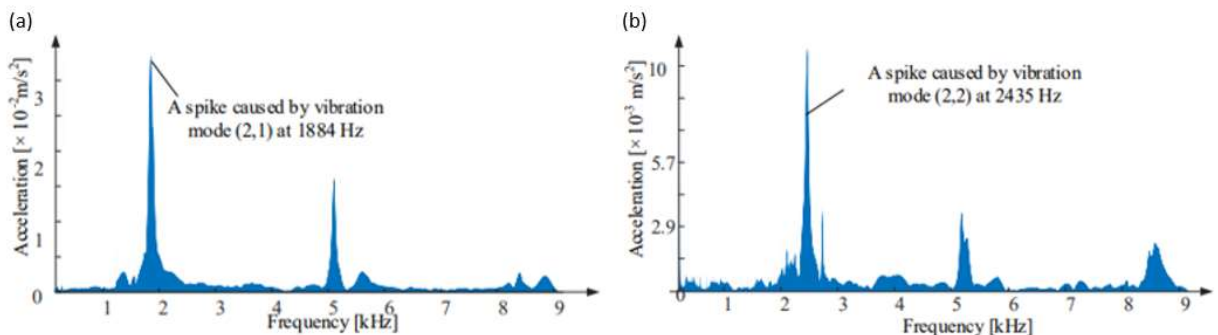


Fig. 3.27 Impact hammer test frequency-domain response when (a) struck in middle of stator lamination and (b) struck on the bolted corner

The natural frequencies of both mode (2,1) and mode (2,2) correspond to the lowest spikes seen by the hammer tests. The lowest natural frequency spikes are the vibration modes that will have the lowest decay rates for a time-domain damped oscillation. In comparison, the higher natural frequency spikes will decay to almost zero after a few time-domain cycles. This means that the response of the lower spikes will dominate the oscillations for a much longer period in the time-domain cycles. [53].

These natural frequencies were calculated using ANSYS modal and were coupled with the nodal forces from the ANSYS Maxwell 2D EM simulation. The operating point simulated for experimental validation was 2048 rpm for 5 Nm reference using a gaussian current input from [22] for one electric cycle which is shown in Fig. 3.28.

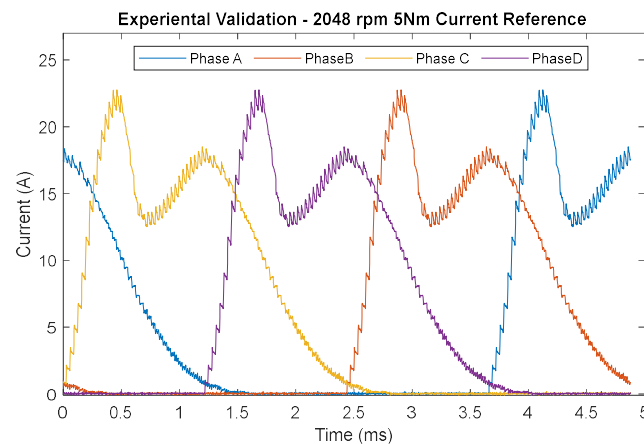


Fig. 3.28 Phase currents for one electric cycle at 2000 rpm 5 Nm reference

The combined FEA simulations generate the forced vibration response and calculate the SPL produced by the motor using the acoustic noise modelling techniques explained earlier in this chapter. The simulated SPL is then compared to the experimentally calculated SPL

from the same microphone position. Both SPLs share peak characteristics and trendlines of dominant frequencies. Specifically, the peak values at dominant frequencies match well for the numerical and experimental SPLs. These experimental results have been compiled in both [22,50] for comparison to the obtained FEA results and plotted in Fig. 3.29. As seen in Fig. 3.29, at 1843 Hz, the numerical results calculated 63.24 dB compared to the measured 57.98 dB. Additionally, at 2253 Hz and 2662 Hz the numerical results calculated 43.374 dB and 43.418 dB compared to the measured 46.91 dB and 45 dB. Additionally, in Table.3.2 the highest SPLs from [22,50] are compared to the FEA results.

These peak SPL frequencies occur from the excitation of the stator's vibration modes ( $circ,ax$ ) = (2,1) and (2,2). Specifically, the forcing frequency at 1843 Hz is the  $(u, v) = (54^{th}, 2)$  temporal order harmonic of the radial force density from this motor and is very close the mode (2,1) natural frequency of 1884 Hz. Similarly, forcing frequencies 2253 Hz and 2662 Hz are the  $(66^{th}, 2)$  and  $(78^{th}, 2)$  temporal order radial force harmonics which are close to the stator's vibration mode (2,2). Furthermore, a qualitative analysis for the excitation of the stator's vibration mode 2 can be visualized through the near field directivity plots seen in Fig.3.30 at 1843 Hz and 2662 Hz. These results match well and serve as validation of the FEA modelling used for acoustic noise analysis for this 8/6 SRM.

Table 3.2 Experimental SPL vs. FEA calculated SPL

Experimental Validation	(54 <sup>th</sup> ,2) order 1843 Hz	(66 <sup>th</sup> ,2) order 2253 Hz	(78 <sup>th</sup> ,2) order 2662 Hz
[22] Experimental Results	57.98 dB	46.91 dB	45.00 dB
[50] Experimental Results	58.00 dB	49.00 dB	48.00 dB
FEA Numerical Results	63.24 dB	43.37 dB	43.42 dB

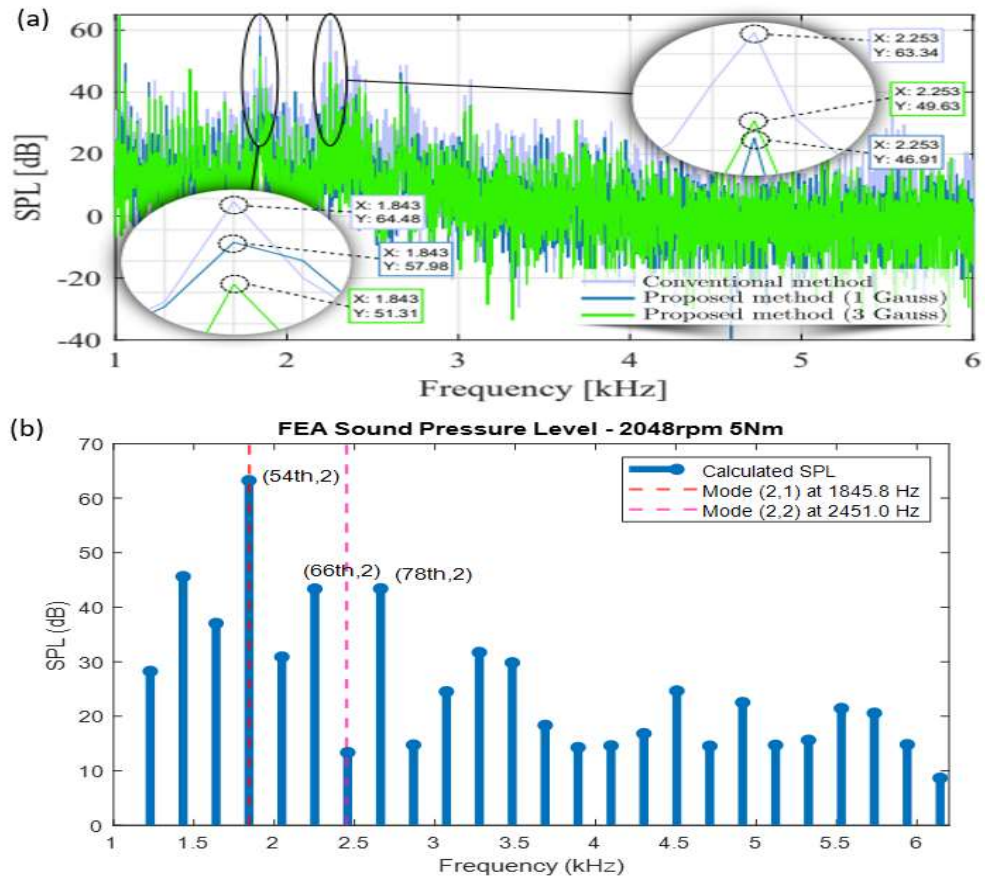


Fig. 3.29 (a) Experimental SPL results from [22] and (b) FEA calculated SPL results

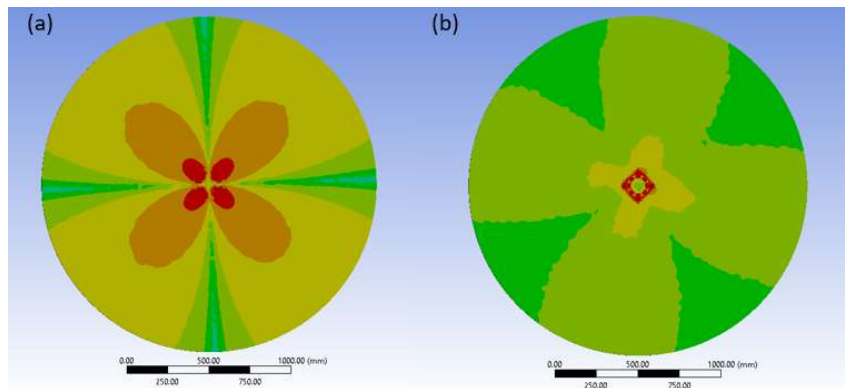


Fig. 3.30 Acoustic noise near field directivity plots (a) mode (2,1) resonance at 1843 Hz and (b) mode (2,2) resonance at 2662 Hz

## Chapter 4

# Structural Design Techniques in SRMs for Acoustic Noise and Vibration Reduction

This chapter analyzes various structural design modifications to reduce acoustic noise and vibration in a switched reluctance machine. The structural modifications are investigated on a four phase 8/6 SRM. The designs considered are inspired by an in-depth literature review on previous documented design strategies for vibration and acoustic noise reduction of SRMs. As acoustic noise reduction is a multifaceted problem, the considered designs are broken down into two broad categories: stator-housing modifications and rotor modifications.

The stator-housing modifications include variations of the stator along with the housing and assembly fixtures that make up the entire motor model. The structural design modifications aim to increase the stiffness of the motor assembly. By increasing stiffness, the natural frequencies will increase and reduce resonance overlap with radial force excitations. Targeting an increase in stiffness also aims to reduce the impact induced vibrations have on acoustic noise production.

The rotor modifications include design changes that alter the electromagnetic characteristics of the SRM. These design modifications are much more sensitive to the operational characteristics of SRMs and require optimized solutions for the best trade off between acoustic noise reduction and electromagnetic performance. These modifications

include the introduction of notches and windows to the rotor laminations. The goal of these design changes is to reduce the amplitude of produced radial forces to minimize vibrations of the motor assembly while preserving as much electromagnetic performance as possible.

#### 4.1 Baseline Motor Design

Before any design considerations are evaluated, a baseline model was established that serves a reference for torque, radial force, vibration, and acoustic noise performance. All designs considered start with the stator and rotor components of the four phase 8/6 SRM presented in Fig. 4.1.

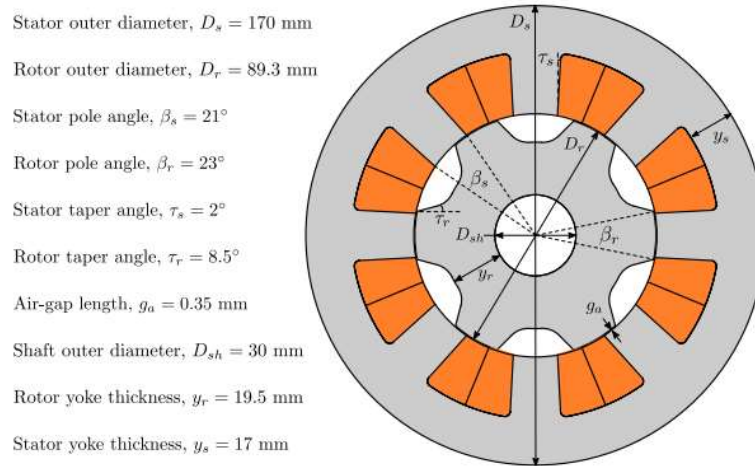


Fig. 4.1 Baseline 8/6 SRM stator and rotor dimensions [53]

The axial stack length of the stator and rotor laminations is 90 mm and a simplified 20 mm thick cylindrical shell housing along with an end cap and a mounting plate are used for the motor's enclosure. The stator is connected to the housing with an interference press fit contact. The interface between the housing and endcaps uses four bolt connections to

connect the components. Additionally, four flange mounts are used to mount the entire assembly system. The exploded baseline assembly can be seen in Fig. 4.2.

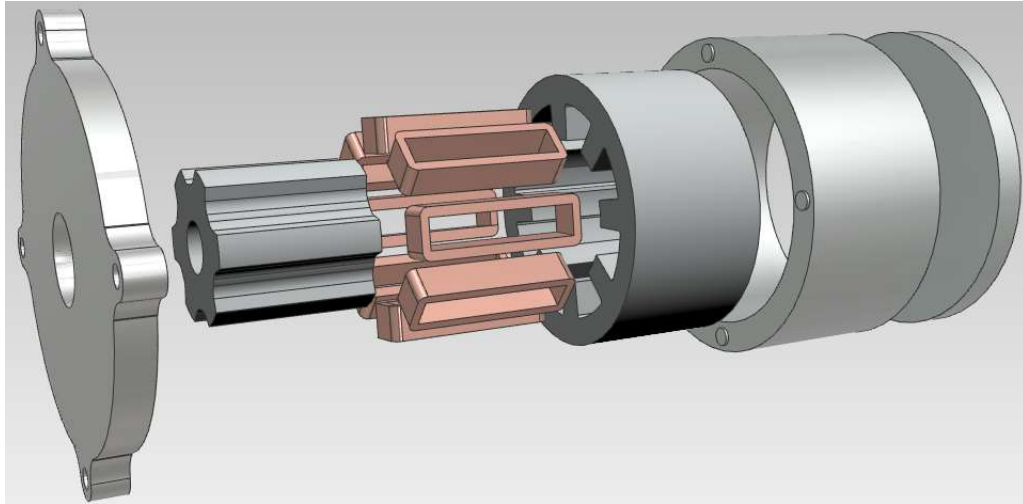


Fig. 4.2 Exploded view of the baseline 8/6 motor assembly

The materials used for the assembly include copper for the windings, aluminum for the housing and end caps and electric steel lamination for the rotor and stator. The material properties for each component used are displayed in Table 4.1. It should be noted that the properties of the copper windings are adjusted based on assumptions outlined in Chapter 3, to accurately model the mass and stiffness of the windings while also accounting for the slot fill factor and insulation.

Table 4.1 Material properties for the baseline 8/6 SRM assembly

Component	Density (kg/m <sup>3</sup> )	Young's modulus (GPa)	Poisson's ratio
Electric Steel Lamination	7267.5	176	0.285
Housing and Endcaps	2700	68.9	0.33
Coil windings	4908	12	0.3

Before modifications are made to any components, the electromagnetic, structural, vibration and acoustic noise analysis are conducted at a desired operating condition. To ensure the motor operating condition takes saturation effect into account, a constant current value of 21.21A.

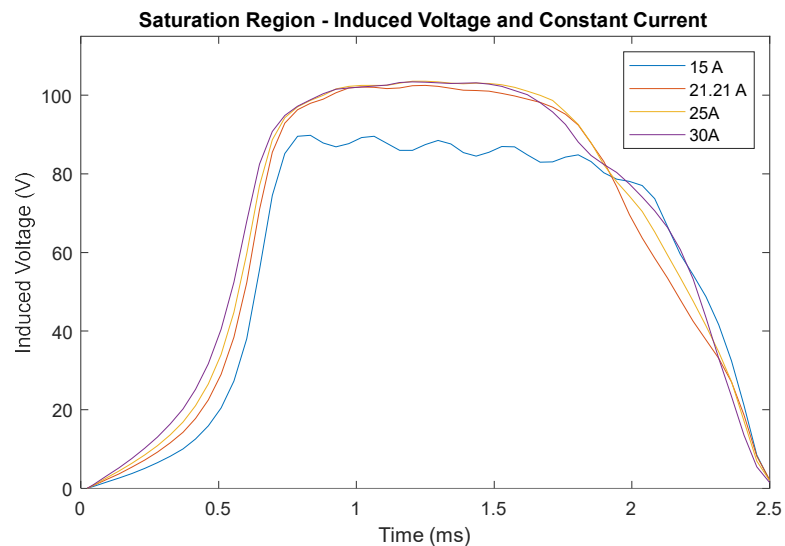


Fig. 4.3 Induced voltage vs. constant current

As seen in Fig. 4.3 increasing the current past 21.21 A results in very similar induced voltage for this motor meaning that it is in the saturated region. Using a single phase constant current excitation, LUTs are obtained from Ansys Maxwell for the Simulink control model. These include the torque, induced voltage and flux linkage and data as shown in Fig. 4.4.



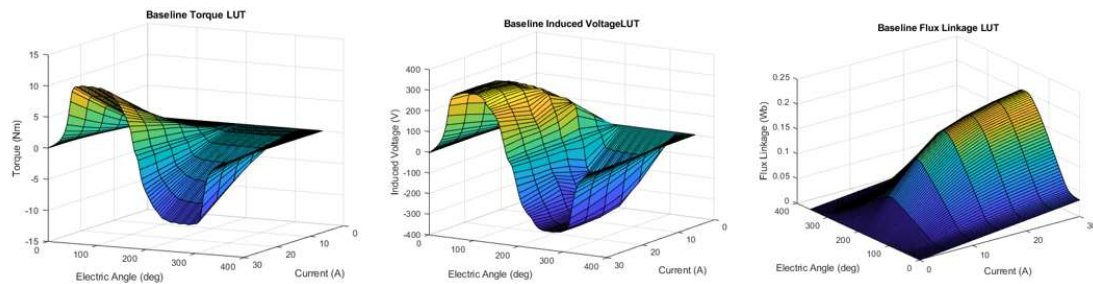


Fig. 4.4 Torque, Induced Voltage and Flux Linkage LUTs

The dynamic Simulink model obtains the phase current references based on hysteresis control voltage chopping that was introduced in Chapter 2. The operating condition chosen is 2000 rpm, with a 21.21 A current reference. The conduction angles were chosen to be turn on 0 electric degrees and turn off 135 electrical degrees. These values were chosen for a generic torque reference. As the focus of this thesis is on mechanical design, alterations to current control techniques have not been investigated for acoustic noise reduction. Therefore, the comparison of design candidates needs a normalized operating condition with the same current reference. By defining these operating condition variables in the dynamic model, the same produced current waveform can be used to analyze the dynamic characteristics of each model and compare performance indicators. The produced phase current waveform from the Simulink model can be seen in Fig. 4.5 (a) which serve as the baseline dynamic reference for the performance of all the modified designs. The simulations are run for one electric cycle to simulate the excitation of each phase. The produced torque for the baseline model has an average value of 6.99 Nm and 57.00% torque ripple at 2000 rpm, which can be seen in Fig 4.5 (b).

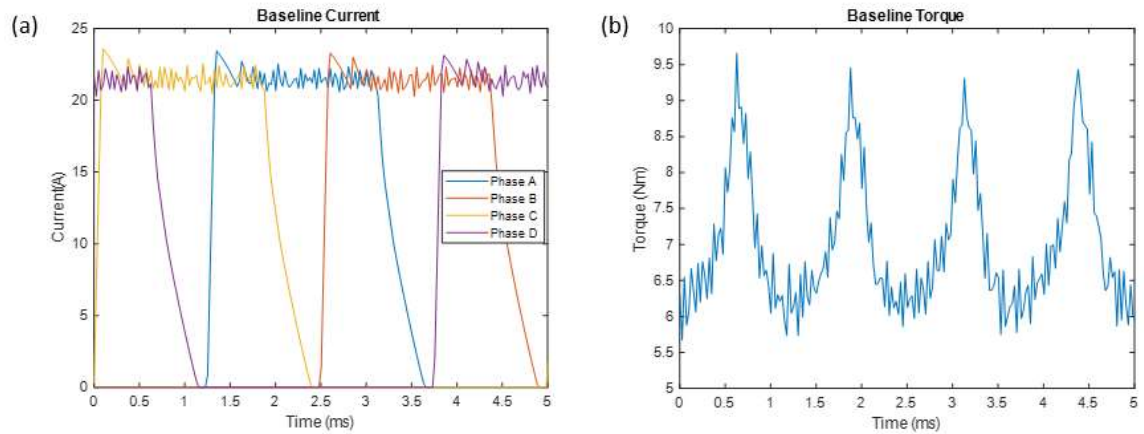


Fig. 4.5 Dynamic phase currents and torque for the baseline 8/6 SRM at 2000 rpm

Additionally, the produced radial force densities are analyzed to understand the components from the dynamic simulation. A 2D FFT is conducted to analyze the dominant spatial and temporal harmonics as shown in Fig. 4.6.

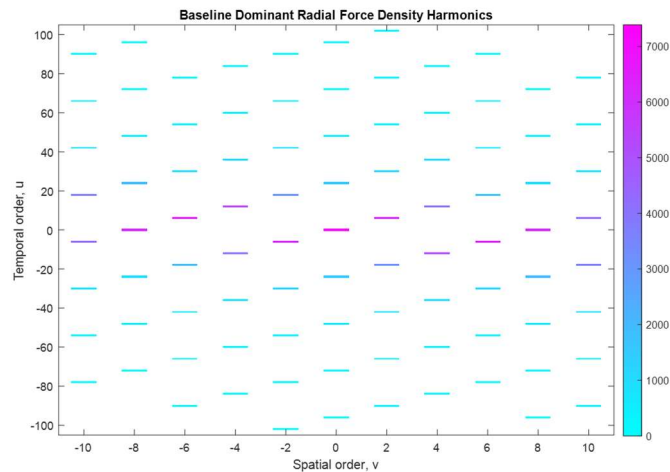


Fig. 4.6 Spatial and temporal decomposition of radial force density harmonics

The 3D assembly was then used in the FEA flow presented in Chapter 3 to calculate the natural frequencies, vibrations, and acoustic noise of the baseline model. The resulting

mode (2,1) natural frequencies occurred at 3030 Hz and 3551 Hz which can be seen in Fig. 4.7. The vibration mode 2 is the most important structural mode for this design as the characteristics of the four phase 8/6 SRM excite two stator poles per phase, producing an oscillating oval shape of the radial force density. This is reflected for dominant harmonics with a spatial order of  $\nu = |2|$  in Fig.4.6. Specifically, when the spatial order  $\nu = |2|$  harmonics have temporal order frequencies that match closely to the natural frequency of mode 2, this can cause resonance excitation which results in excessive vibrations and acoustic noise for this motor.

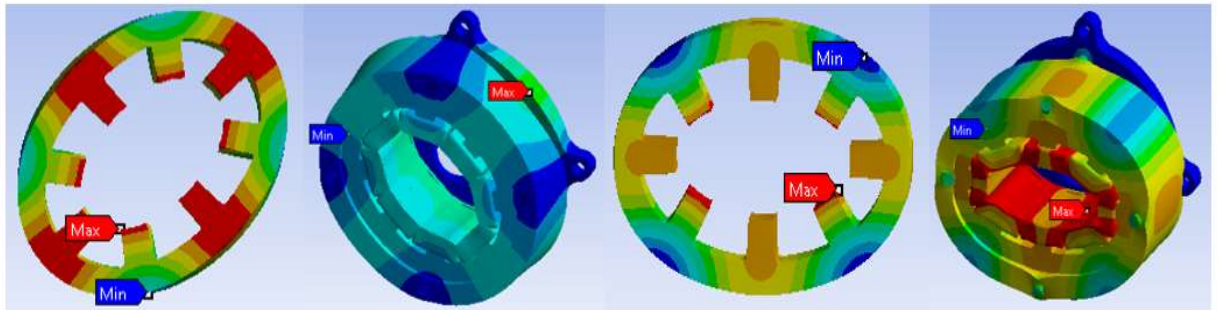


Fig. 4.7 Mode (2,1) natural frequencies of the baseline 8/6 stator

The harmonic response vibration simulation calculates the deformation and von-mises stress of the stator. The maximum deformation observed was  $0.123 \mu\text{m}$  and the maximum stress on the stator was  $0.284 \text{ MPa}$ . The deformation pattern and stress distribution for the maximum deformation frequency of  $2600 \text{ Hz}$  are displayed in Fig.4.8.

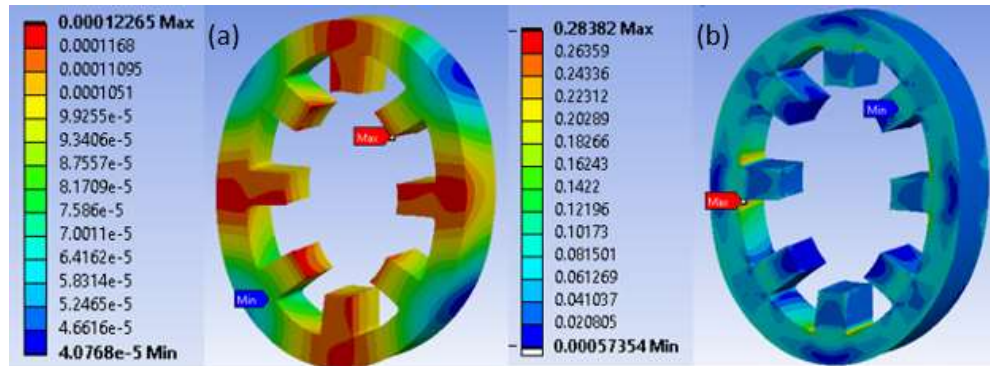


Fig. 4.8 (a) Deformation and (b) stress contour from the forced vibration simulation at 2600 Hz

The vibration results show the stator's mode 2 is excited by the imported nodal forces. The surface velocities of the assembly components were imported to calculate the acoustic noise of the motor. The acoustic noise was measured from a virtual microphone placed 1m away from the motor assembly. At the baseline operating condition, the acoustic noise results are displayed in Fig. 4.9.

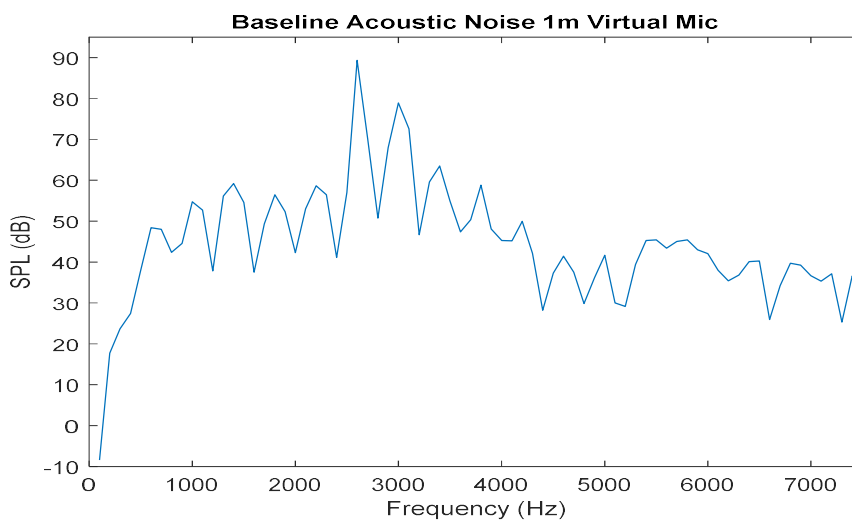


Fig. 4.9 Acoustic noise SPL results for the baseline 8/6 SRM

The maximum SPL of 89.3 dB occurs at 2600 Hz and the second peak of 78.94 dB occurs at 3000 Hz. Both of these frequencies cause high acoustic noise due to resonance excitation of the stator's vibration mode 2. These two frequencies, 2600 Hz and 3000 Hz correspond to the  $u = 78^{\text{th}}$  and  $90^{\text{th}}$  temporal order frequencies at this operating speed. When compared to the dominant radial force density harmonics in Fig. 4.10 it can be seen that the spatial order  $v = |2|$  has harmonics at the  $78^{\text{th}}$  and  $90^{\text{th}}$  temporal order. The shape of the radial force density wave along with the frequency of the dominant temporal orders match closely to the natural frequency of 3030 Hz for this motor.

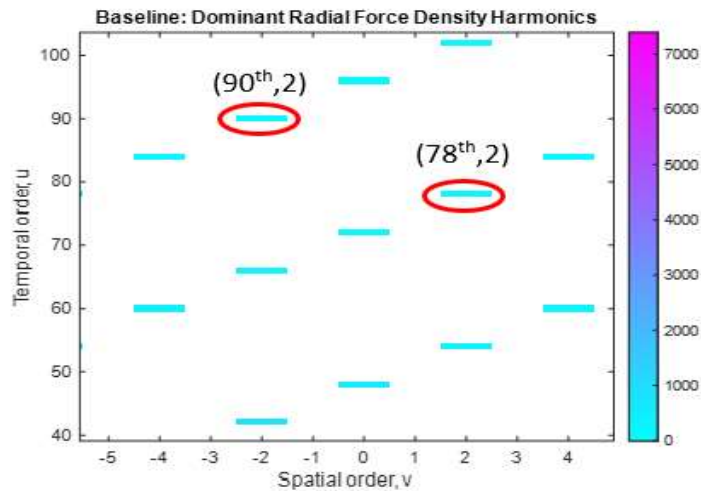


Fig. 4.10 Radial force density harmonics (78,2) and (90,2) that excite vibration mode 2 of the baseline 8/6 SRM

The total SPL for this design is 89.89 dB when all frequency points are totalled using (3.21) for this operating condition at 2000 rpm. These results serve as the baseline design for comparison when design modifications are made. The following section applies

strategic design considerations with the goal to reduce the peak characteristics and total SPL for this motor at this operating condition.

Based on the NVH results from the baseline model it was evident that this motor needed to target an increase in stiffness for the structural design. The amplitude of the resonance excitation SPL can be decreased by pushing the natural frequencies higher to avoid resonance excitations caused by the lower radial force density harmonics that have higher amplitudes.

## **4.2 Stator-Housing Assembly Considerations**

The first structural consideration was the assembly contact between the stator and the housing. For SRMs two common practices are used to assemble these components: bolted and interference press fit. In the first iteration of design comparisons, the housing and stator systems were compared for a natural frequency analysis with a press fit assembly and with a bolted assembly. Both designs were compared for natural frequency analysis. For this SRM, vibration mode 2 is of particular importance as spatial order 2 produced by the motor operation is the lowest natural frequency overlap for resonance excitations that can cause high acoustic noise levels. Vibration mode (2,1) natural frequencies for the bolted assembly were calculated to be 2242.2 Hz and 2298.2 Hz compared to the press fit natural frequencies of 3030.0 Hz and 3551.7 Hz. The shapes of the two results can be seen in Fig. 4.11.

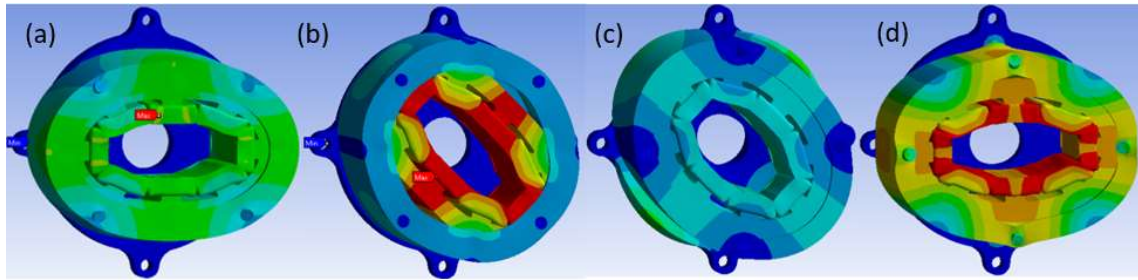


Fig. 4.11 Bolted contact modes (2,1) natural frequencies (a) 2242.2 Hz and (b) 2298.2 Hz vs. interference press fit contact modes (2,1) (c) 3030Hz and (d) 3551.7 Hz

From this analysis it was concluded the press fit stator assembly is the stiffer candidate. The lower natural frequencies from the bolted assembly will allow high amplitude harmonics to overlap and create resonance which will result in higher vibrations and acoustic noise. Compared to the bolted assembly, the surface area in contact between the stator and housing in the press fit assembly is significantly higher, which increases the overall design stiffness. Additionally, the bolted assembly shows mode (2,1) of the stator behaves more independently from the housing compared to the mode (2,1) of the press fit assembly that match shape with the housing. For both designs there exists two natural frequencies for mode (2,1) due to the variation in stiffness for the areas aligned with the housing bolts and unaligned with the housing bolts. From these conclusions, the next iteration in the stator design process uses designs considering interference press fit assembly systems.

### 4.3 Stator Yoke Modifications

Modifications to stator yoke shape influence the natural frequencies of the system along with the assembly stiffness. From the literature, SRM stators showed increased stiffness

when the stator outer yoke shape was a regular polygon that matched the number of corners to the number of stator poles. For this reason, a few variations of octagon stator shapes were investigated. The various design candidates were analyzed to compare the impacts of geometry changes, particularly to the natural frequency of the dominant vibration mode 2 of the stator. A 20 mm thick housing that matches the shape of each stator yoke design is used to normalize the comparison of each design. This is done to simplify the assembly procedure and to account for the varying stator yoke thickness for each design. The various stator shapes are shown in Fig. 4.12.

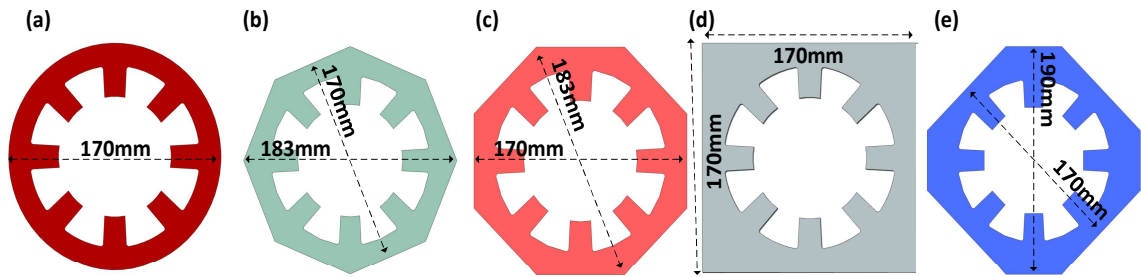
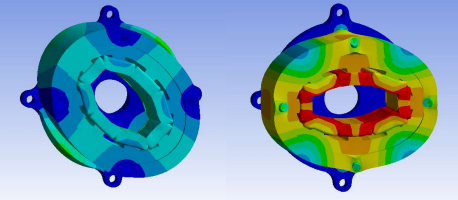
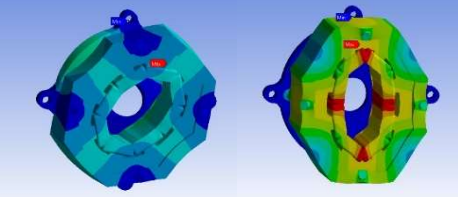
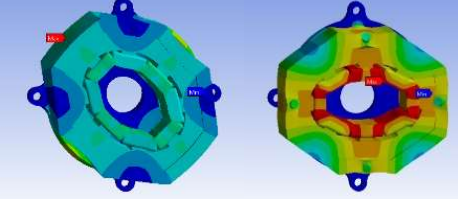
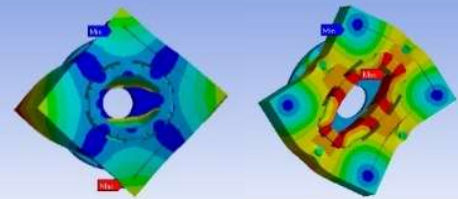
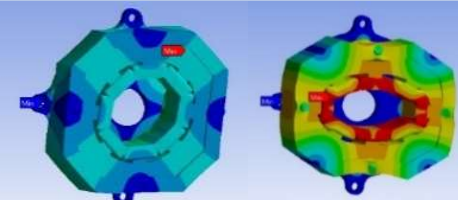


Fig. 4.12 Stator yoke shape designs (a) octagon I (b) octagon II (c) square (d) hybrid octagon

The FEA calculated natural frequencies using the assembly with each stator design were compiled. The vibration mode 2 natural frequencies of each stator design are shown in Table 4.2. Additionally, the mass of each stator is an important design consideration and each stator design is composed of the same electric steel lamination material. In Table 4.2, the mass, mode 2 natural frequency and corresponding shape of each stator design is presented.



Table 4.2 Stator yoke designs and corresponding mode 2 natural frequencies

Design	Stator Mass	Mode 2 Natural Frequencies	Mode 2 Shapes
Baseline	7.48 kg	3030 Hz and 3551 Hz	
Octagon I	8.16 kg	3013.9 Hz and 3485 Hz	
Octagon II	8.16 kg	3063.8 Hz and 3543.7 Hz	
Square	11.54 kg	3103.8 Hz and 3450.4 Hz	
Hybrid Octagon	9.69	3170.8 Hz and 3578.5 Hz	

To understand the impact these designs have on acoustic noise production, the octagon II and hybrid octagon designs were chosen to run vibration and acoustic noise analysis.

Octagon I design was ignored as octagon II had better natural frequency results for the same size stator and the square design was not considered as the increase in stator size is too significant to be a practical option (4.06 kg increase from baseline). The deformation and stress results from both simulations can be seen for 3000 Hz in Fig. 4.13. Octagon II had a maximum deformation is  $0.089 \mu\text{m}$  whereas the hybrid octagon had a maximum deformation of  $0.114 \mu\text{m}$ . Similarly, the maximum stress for octagon II is  $0.548 \text{ MPa}$  whereas the maximum stress for the hybrid octagon is  $0.379 \text{ MPa}$ . For comparison, the maximum baseline deformation is  $0.123 \mu\text{m}$  and the baseline maximum stress on the stator was  $0.284 \text{ MPa}$  at  $2600 \text{ Hz}$ .

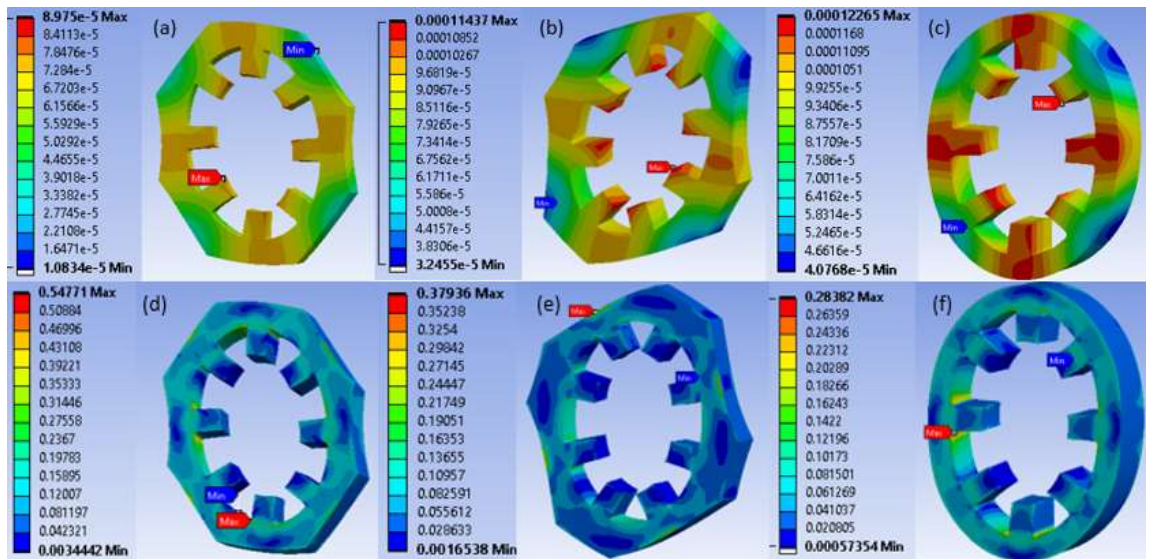


Fig. 4.13 Deformation contour plots for (a) octagon II (b) hybrid octagon and (c) baseline and stress contour plot for (d) octagon II (e) hybrid octagon and (f) baseline

The increase in natural frequencies for these two designs help reduce the acoustic noise produced by the motor, but also the shapes of the stator's impact the way the forces

propagate through the assembly to produce vibrations and noise. Both designs show significant decrease in vibrations and acoustic noise when compared to the baseline design. From the vibration analysis, the distribution of stator deformations for both the octagon II and hybrid square designs in Fig. 4.13 are more uniform than the baseline design in Fig.4.8. This means the oscillations of the stators will experience a less dynamic response than the baseline stator when excited by the imported nodal forces. Additionally, the modified square performs better for vibration and acoustic noise reduction in comparison to octagon II. This is attested to the higher natural frequencies of mode 2. The acoustic noise results comparisons can be seen in Fig. 4.14.

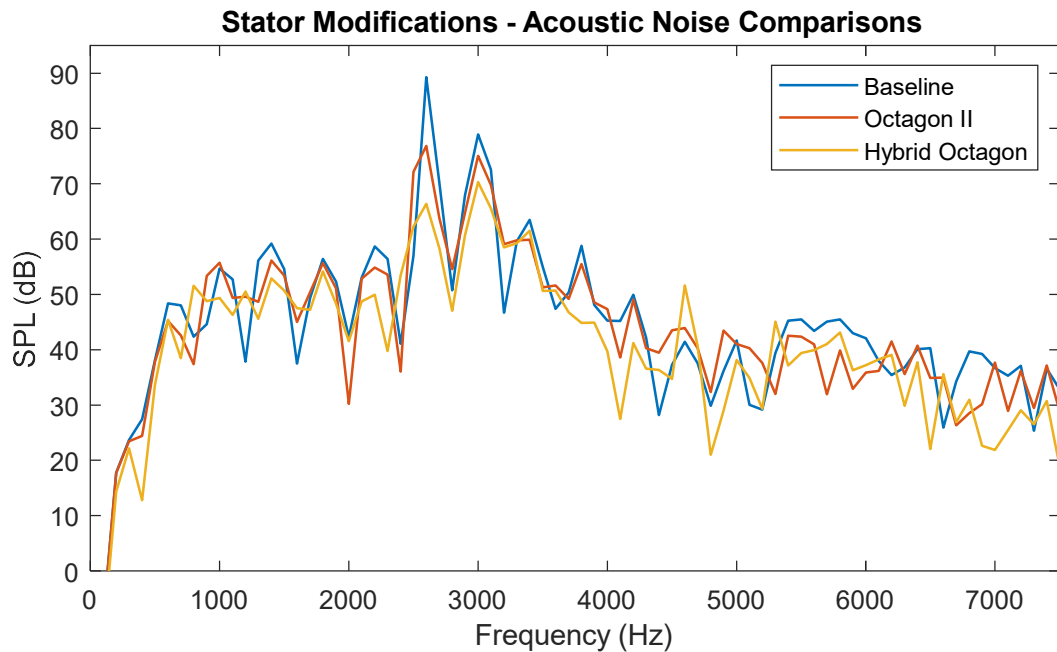


Fig. 4.14 Total SPL comparison for octagon II and hybrid octagon designs vs. baseline

Compared to the baseline design, octagon II reduces the peak value of the produced SPL from 89.30 dB to 76.81 dB, but these peaks both occur at the same frequency of 2600 Hz

since both designs have similar mode 2 natural frequencies. The hybrid octagon design reduces the maximum SPL from 89.30 dB to 70.28 dB and pushes the peak frequency to 3000 Hz as the mode 2 natural frequencies are higher than both the octagon II and baseline designs. The significance of mode 2 resonance for acoustic noise is reflected in Fig.4.14 as the two highest SPLs produced by all three designs correspond to the dominant 78<sup>th</sup> and 90<sup>th</sup> temporal order harmonics outlined in Fig. 4.10, at forcing frequencies of 2600 Hz and 3000 Hz.

In summary, the acoustic noise of the four phase 8/6 SRM can be significantly reduced by modifying the stator yoke shape, specifically if the octagon II or hybrid octagon designs are used. Table 4.3 outlines the performance criteria evaluated for the designs compared to the baseline model. Although the best design shape from this analysis is concluded to be the hybrid octagon, the increase of mass must be considered when choosing the best overall design candidate.

Table 4.3 Evaluated performance criteria for the evaluated stator yoke designs

Design	Avg. Torque	Max. Radial Force	Peak SPL	Total SPL
<b>Baseline</b>	6.998 Nm	1633.514 N	89.30 dB @ 2600 Hz	89.89 dB
<b>Octagon II</b>	7.010 Nm	1635.809 N	76.81 dB @2600 Hz	80.73 dB
<b>Hybrid Octagon</b>	7.011 Nm	1635.778 N	70.28 dB @ 3000 Hz	74.40 dB

For each design, the mass of the rotor and the end plates remain constant, but due to increased stator circumference and size, the corresponding stator and housing mass increases for the modified designs. The mass comparison between each design can be

compared to the baseline design in Table 4.4 below. The stator and rotor material are comprised of the same lamination material as the baseline design and the housing and end caps are made from aluminum.

Table 4.4 Total assembly mass for modified stator yoke designs

Design	Rotor Mass	Endcaps Mass	Stator Mass	Housing Mass	Total Mass
<b>Baseline</b>	2.84 kg	3.79 kg	7.48 kg	3.35 kg	17.46 kg
<b>Octagonal 1</b>	2.84 kg	3.79 kg	8.16 kg	3.51 kg	18.30 kg
<b>Octagonal 2</b>	2.84 kg	3.79 kg	8.16 kg	3.51 kg	18.30 kg
<b>Square</b>	2.84 kg	3.79 kg	11.54 kg	4.27 kg	22.44 kg
<b>Hybrid Octagon</b>	2.84 kg	3.79 kg	9.69 kg	3.74 kg	20.06 kg

As outlined in table 4.4, although the best design candidate for highest natural frequencies is the hybrid octagonal, the design increases 2.6 kg to achieve this result. Depending on the application, mass and torque density may be important design considerations. These conclusions allude to the need for a stiffer design with minimal increase in mass.

From the analysis conducted on the various stator shapes, the lowest mode 2 natural frequency resulted from the mode shape that exist in-between the four bolt fixtures of the housings. For reference in Table 4.2, the lowest natural frequency for the mode 2 shapes of all designs have bulges in-between the four housing bolts. Consequently, for the baseline design, the highest acoustic noise occurred at 2600 Hz from the excitation of the stator's lowest mode 2 natural frequency of 3030 Hz in-between the bolts. For this reason, the

impact of increasing the number of bolted contacts from the housing to the end plates was investigated.

#### 4.4 Fastener Component Considerations

To understand the impact the housing-endplate bolted contacts have on the natural frequencies of the assembly system, the number of bolts for the baseline design was increased. Two designs used the same size of bolts but increased the number from 4 to 8 and 16. The resultant stiffness of the system increased significantly. This can be quantified by the increase in natural frequency from the increase in bolts as seen in Table 4.5. All geometries are kept consistent to ensure that the only impact on system natural frequencies are the number of bolts.

Table 4.5 Mode (2,1) natural frequencies of increased bolt designs

Design	Mode (2,1) Natural Frequencies
Baseline (4 bolts)	3030 and 3551 Hz
8 bolts	3486.2 and 3617.9 Hz
16 bolts	3769.4 and 3974.1 Hz

The increased stiffness from the higher number of bolts dramatically increase the mode 2 natural frequencies. Although highest natural frequency is desired, the manufacturing complexity of these designs also needs to be considered. With the increase in number of bolts comes an increase in manufacturing and production cost to machine or manufacture the bolt holes. Similar SRM assemblies use minimal bolt contacts, for example in [2], where a 24/16 SRM used 6 bolts connections to assemble the housing to the end plates. For this

reason, the design was chosen to limit the number of bolts to 8. The 8 bolts were chosen to be aligned with the stator poles of the SRM. This was done to increase the stiffness in regions behind the stator poles, which experience the most radial force from the motor's operation and therefore propagate the most vibrations through to the housing.

In a similar way, the stiffness of the system was investigated by analyzing the impact the number of flange mount bolts have on natural frequencies. Likewise, the manufacturing complexity from increasing the number of flange mounts must also be considered. For this reason, the number of flange mounts was increased to 8 to match the number of bolts in the housing, which is similar to what was done for the 24/16 SRM in [2], where 6 bolts and 6 flange mounts were used. The increase in fastener components is shown in Fig. 4.15 and the natural frequency results can be seen in Table 4.6.

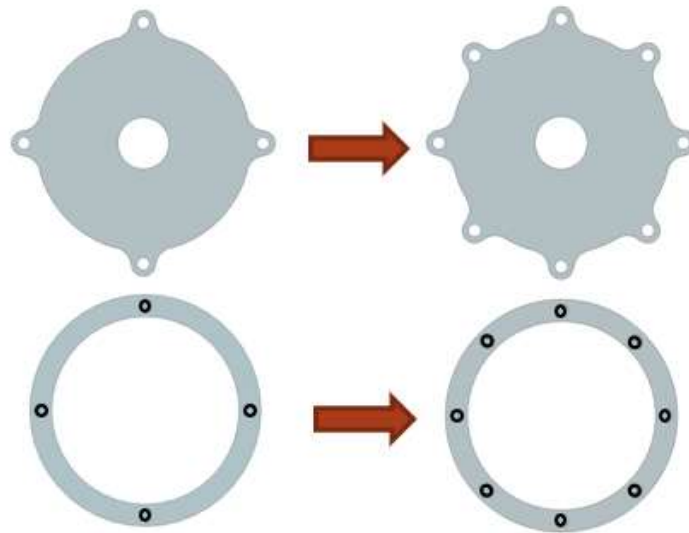


Fig. 4.15 Increased fastener components

Table 4.6 Mode (2,1) natural frequencies of an additional flange mount design

Design	Mode 2,1 Natural Frequency
Baseline	3030 Hz and 3551 Hz
4 bolts, 4 flange mounts	
8 bolts, 4 flange mounts	3486.2Hz and 3617.9 Hz
8 bolts, 8 flange mounts	3622.8 Hz and 3623.2 Hz

The addition of four flange mounts increases the lowest mode 2 natural frequency by 136.6 Hz. This will reduce the excitation of mode 2 as higher temporal harmonics with a lower pressure amplitude will overlap with this increased natural frequency. The temporal order harmonic magnitude pattern was shown previously in Chapter 3, in Fig. 3.6. An increased mode 2 natural frequency means the overlap for resonance will occur at a higher temporal order harmonic forcing frequency with  $v = 2$ , which will have a lower pressure magnitude and will reduce the acoustic noise when compared to the baseline model.

#### 4.5 Stator Back Iron Notches

The last stator- assembly modification investigated was the introduction of notches to the stator back iron. The notch design included a cut 5mm deep at the center of the arc into the back iron and spans  $16^\circ$  (24mm). The width of the notch was decided by extending the stator pole lines to where they meet the outer circumference of the stator. The design of the notches can be seen in Fig. 4.16. The notches were specifically introduced in areas where flux is negligible to minimize the impact on EM performance. As shown in Fig. 4.17 the baseline flux lines can be seen in the stator back iron for one phase excitation and is compared the flux lines for the modified stator notches. The notched design showed the same average torque as the baseline model within 0.05% and slightly reduced the produced



maximum radial force. These torque and radial force results are compiled in Table 4.7 for both the single-phase static simulation and for the dynamic simulation.

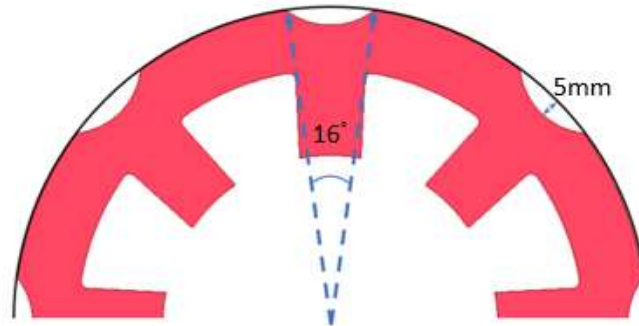


Fig. 4.16 Stator back iron notch design

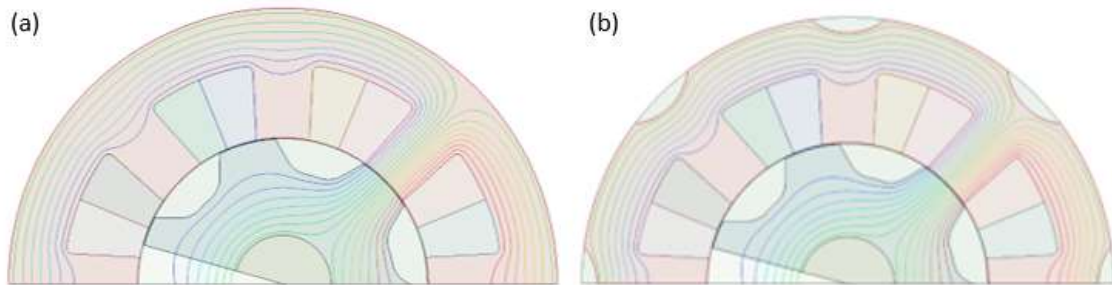


Fig. 4.17 Flux line comparison between (a) the baseline stator and (b) the notched back iron stator

Table 4.7 EM performance of the notched back iron design

Design	Static Avg. Torque	Static Max. Radial Force	Dynamic Avg. Torque	Dynamic Max. Radial Force
Baseline	4.1053 Nm	1792.01 N	6.9989 Nm	1633.51 N
Stator back iron notched design	4.1043 Nm	1788.73 N	6.9955 Nm	1630.36 N

These notches are located along the shortest path the radial forces travel to propagate from the stator teeth to the housing enclosure. By reducing the stator surface area directly

in contact with the housing at these points, the propagation of vibrations to the housing can be reduced in attempt to reduce acoustic noise. However, the mode 2 natural frequencies for the notched back iron design are slightly lower than the baseline. They are 3028.4 Hz and 3434.2 Hz respectively compared to the baseline's natural frequencies of 3030 Hz and 3551 Hz. The introduction of the notches alters the deformation transmission from the stator outer circumference to the housing. A visualization of this property can be seen in the deformation contour plot in Fig. 4.18, where the deformations of the housing in the areas behind the notches behave much differently than the baseline design. As a result, the peak acoustic noise is reduced. In the comparative plot seen in Fig. 4.19, similar characteristics can be seen for the peak values, although the maximum SPL is reduced from 89.3 dB to 81.88 dB. This brings down the total SPL of the notched design to 84.25 dB, a 5.63dB reduction from the baseline design.

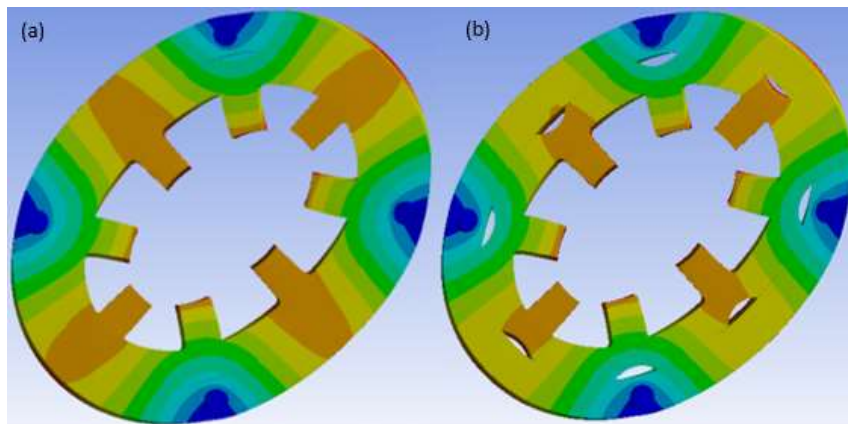


Fig. 4.18 Deformation contour plot for the (a) baseline design and (b) notched stator back iron design

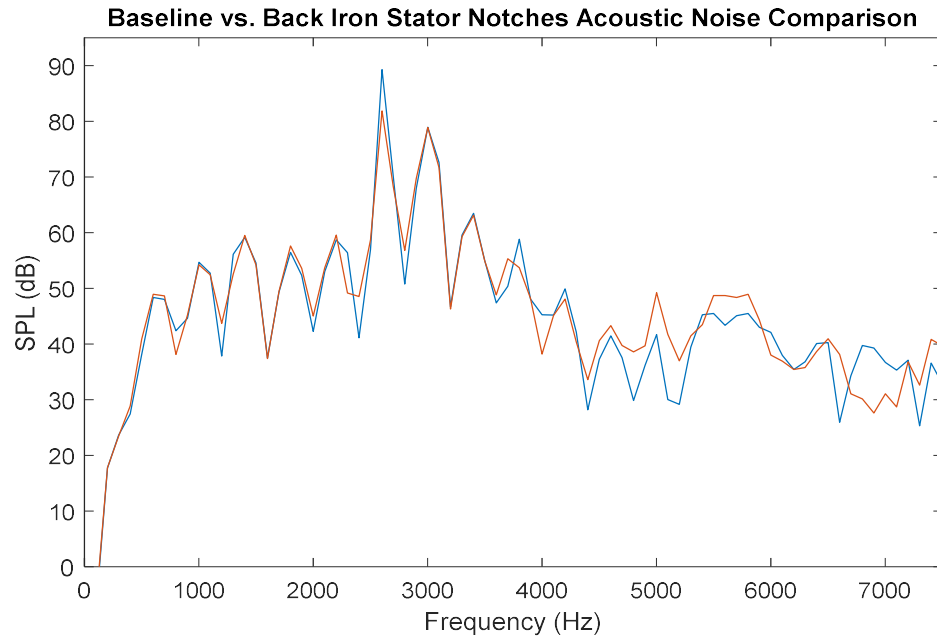


Fig. 4.19 Acoustic noise SPL comparison for notched stator back iron design

The purpose of the investigated designs was to test the best structural modifications from literature to compare the impact on performance for the motor. From the analysis a few conclusions can be made for the best design candidates:

1. An interference press fit stator-housing assembly is stiffer than a bolted connection and will result in higher assembly natural frequencies.
2. Increasing the number of bolted connections between the housing and endplates along with increasing the number of flange mounts will improve stiffness significantly. Although higher stiffness significantly reduces acoustic noise, complexity in manufacturing increases when the number of bolts and flange mounts are increased, therefore total number should be limited.

3. Altering the stator yoke to an octagon shape with corners unaligned with the stator poles will increase stiffness and improve acoustic noise without impacting performance. However, increase in total mass must be considered.
4. Introducing notches to the stator back iron can reduce emitted acoustic noise as they modify the vibration pathway from stator to housing. These notches also have minimal impacts on performance as the generated flux in the notched areas is negligible from the baseline design.

## **4.6 Rotor Modifications**

The second group of design modifications investigated include geometric changes that alter the radial force production of the motor. These modifications include the introduction of notches and windows to the rotor, along with altering the shape of the rotor pole. The EM performance of the motor is sensitive to these designs as they alter the generated flux characteristics. The goal of these modifications is to reduce the produced vibrations and acoustic noise by reducing the magnitude of radial force. However, if acoustic noise reduction is the only goal, motor performance will be significantly sacrificed to achieve low noise. Therefore, in this design procedure, the main goal of these techniques is to reduce the produced radial forces while maintaining EM performance as much as possible.

The evaluation of these designs modifications initially starts by using single phase constant current excitation, or static simulations. This is done to reduce computational time and to eliminate acoustic noise simulations for every possible design change considered. The generated torque and radial force produced by the baseline motor design at the 2000

rpm and 21.21 A operating condition can be seen in Fig. 4.20. The average torque production and maximum radial force produced serve as a baseline measure for all design iterations.

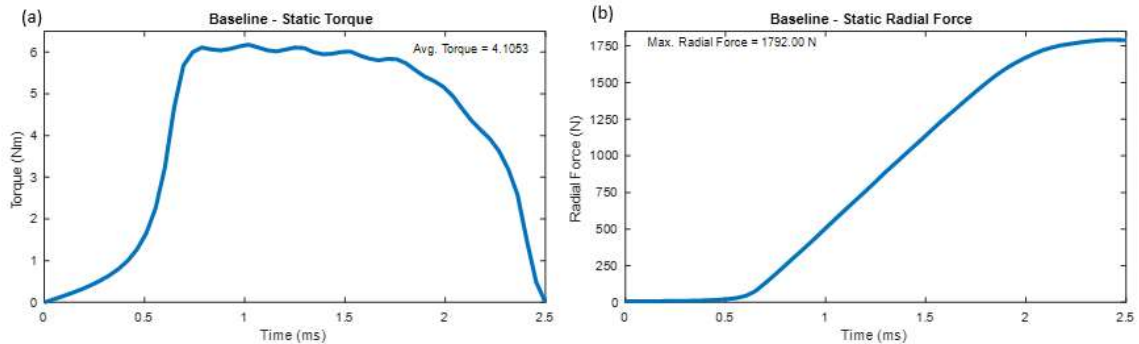


Fig. 4.20 Baseline design static characteristics (a) torque and (b) radial force

To keep track of any performance loss for radial force reduction, a performance ratio (PR) was established according to (4.1). This PR allows for a comparative metric to analyze the trade off ratio between radial force reduction and torque loss compared to the baseline model. Additionally, the highest PRs provide the designs that achieve a relatively higher reduction in radial force for a relatively lower torque reduction.

$$PR = \frac{\% \text{ Max. Radial Force Reduction}}{\% \text{ Avg. Torque Reduction}} \quad (4.1)$$

The first technique investigated was the introduction of windows to the rotor poles. From literature, windows varied in shape, size and location. The pole designs first tested a few basic geometries. These geometries are shown in Fig. 4.21 (a) a square, (b) a triangle (c) a circle, along with two oval designs, one pointing towards the rotor shaft (d) oval I and the

other stretched horizontally across the rotor pole (e) oval II. Each window was kept the same distance from the airgap for each design, and the dimensions of the shapes were aimed to be as similar as possible by approximating the area of all shapes to be  $4\text{mm}^2$ . The various window geometries can be seen in Fig. 4.21.

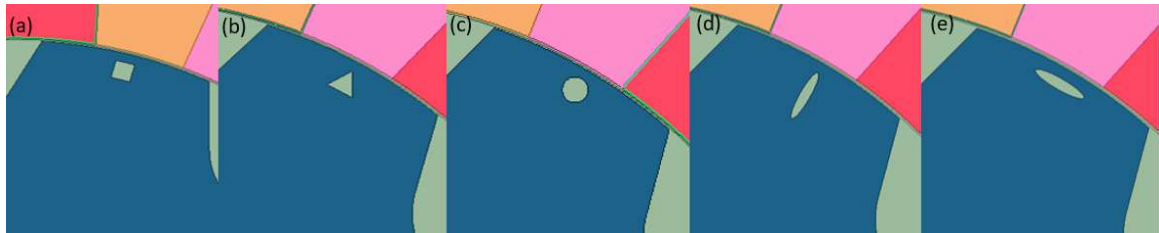


Fig. 4.21 Various rotor window geometries (a) square (b) triangle (c) circle (d) oval I (e) oval II

The dip in the torque profile is a result of the flux density loss from the introduction of the windows. From Fig. 4.22 and Fig. 4.23, it was concluded that for the same size and distance from airgap, the circular window is the best shape as it has the highest PR. The reason for the circle being the best shape is because the smooth edges make smoother flux profiles around the window and avoid tight corners like for the triangle and square geometries. Additionally, it was observed that the wider windows resulted in more torque loss and lower performance ratio. This is due to the increased perpendicular obstruction of the flux in those locations of the rotor pole.

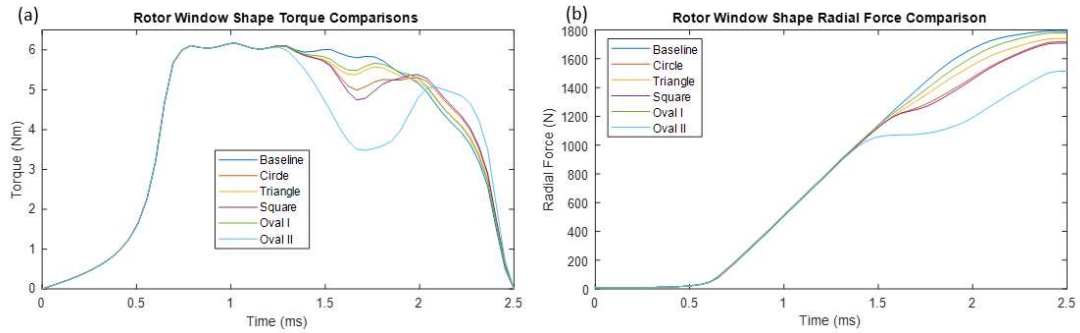


Fig. 4.22 Rotor window performance comparisons for (a) torque and (b) radial forces

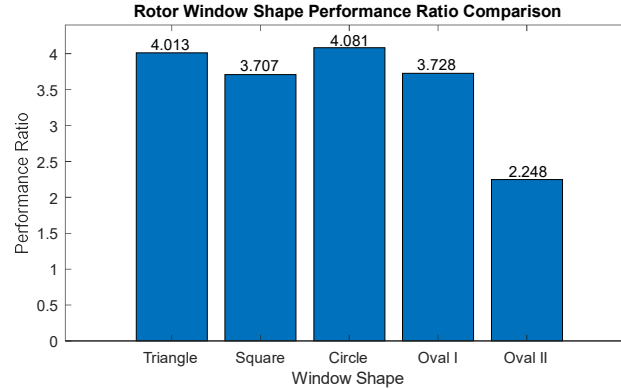


Fig. 4.23 Performance ratio comparison for various window shapes

Once the circle was determined as the best shape for the rotor window, the same window was applied to the stator poles. For the same size circle and same distance from the airgap, the stator windows had a more drastic impact to both torque loss and radial force reduction than the rotor. However, the performance ratio for the same window is worse for the stator. These results can be visualized in Fig. 4.24, where the percent decrease in both torque and radial force along with the performance ratios can be compared for a circular rotor and stator window with 1mm radius and 1mm away from the airgap.

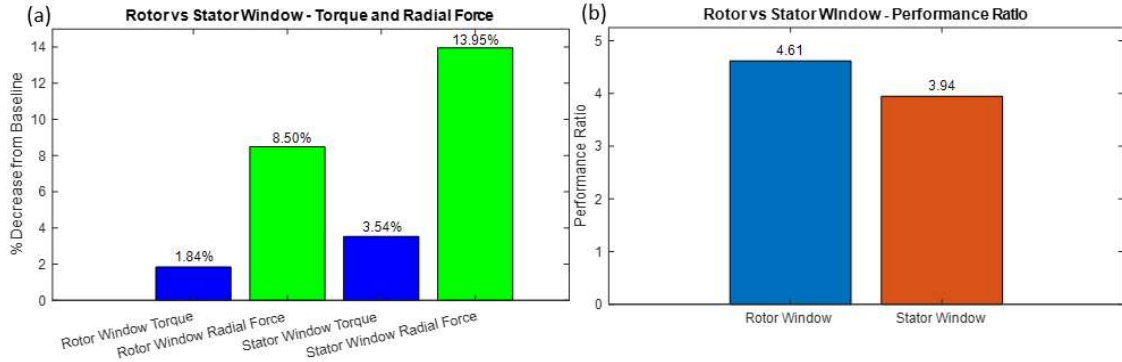


Fig. 4.24 Rotor vs. stator window comparisons (a) torque and radial force reductions (b) performance ratios

Additionally, the impact of proximity to the airgap was analyzed by parameterizing the distance from the center of the circles window to the outer edge of the rotor. Keeping the size of the window consistent, the position for the windows in the rotor, stator and both windows combined were swept from 1mm-16mm. The stator and rotor geometries with the windows can be seen in Fig. 4.25, along with the parameter dimensions. The performance ratio for the rotor window is superior until the windows are 10mm or further away from the airgap. At that distance from the airgap, the rotor windows have negligible impact on either torque or radial force production. Additionally, for each of the locations, the decrease in torque and radial force produced is higher for the stator windows and combination of both windows. The results are compiled in Fig. 4.26.



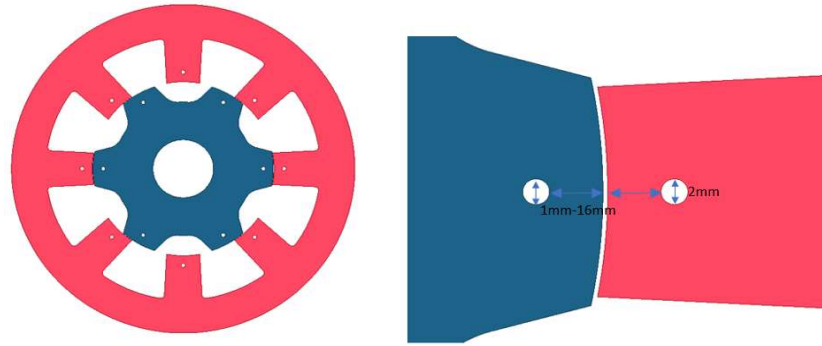


Fig. 4.25 Stator and rotor laminations with parametric circular windows

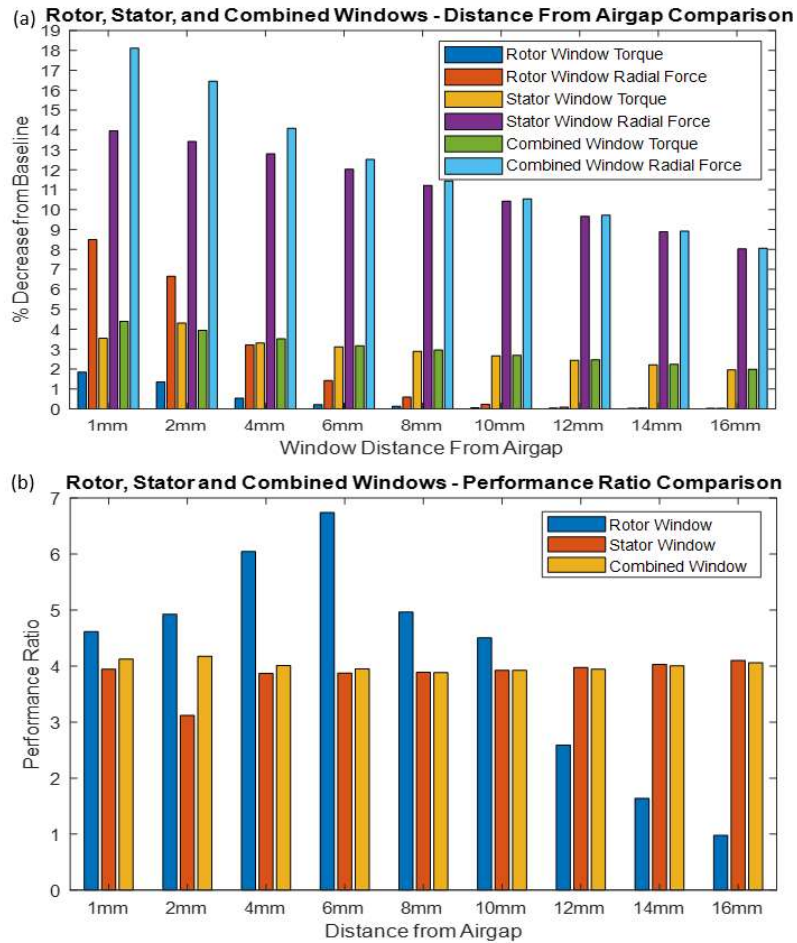


Fig. 4.26 Rotor, stator and combined circular window design comparisons based on proximity to the airgap (a) torque and radial force decreases and (b) performance ratios

This comparative analysis allows for each design to be compared for their performance ratio and respective decrease in both torque and radial force. These results indicate that the trade off for radial force to torque loss is much better for the rotor window, reflected by the higher performance ratios. Specifically, the rotor windows can reduce radial force 8.5% with only a 1.84% reduction in torque production at the 1mm location. In comparison, when the stator and combined windows decrease torque by 1.98%, they only decrease radial forces by 8.05% at the 16mm location. This means, regardless of location, for the same size window, the rotor window will reduce radial forces more while minimizing torque loss.

#### **4.7. Rotor Pole Tip Modifications**

In addition to the introduction of windows to the SRM geometry, rotor pole modifications were investigated. Overall, the performance capabilities of these designs in comparison to the window investigations are less desirable. Nonetheless, these designs were analyzed as many variations are possible. The geometry of the various designs included notches to the rotor pole surface, addition of a rotor rib and manipulating rotor pole geometry. The various types of tested designs are shown in Fig. 4.27.

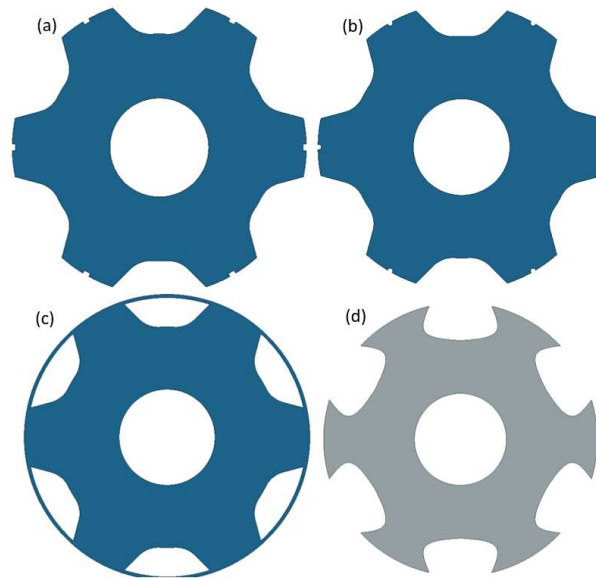


Fig. 4.27 Various rotor laminations with pole modifications (a) rectangular pole surface notch (b) semi-circular pole surface notch (c) rotor rib (d) curved rotor poles

The surface notches for both rectangular and semi-circle shapes are used, both with a 2 mm wide opening and 1 mm depth into the rotor pole. These surface notches impacted the torque production of the SRM significantly due to the change of effective airgap in these regions. The introduction of rotor ribs to improve SRMs was often mentioned in literature [54]. From the addition of a 1 mm rotor rib, the performance for the motor was observed to decrease significantly. Additionally, a unique curved rotor pole geometry was investigated in the literature [37,40]. Based on the observed literature, the pole dimensions were increased from arc angle of  $23^\circ$  to  $34.5^\circ$ .

Each of these designs were run at the operating point of 2000 rpm with a reference current of 21.21 A, which is the same point used in the investigation of rotor windows in Section 4.6. It was observed that none of these designs had performance criteria as effective

as the windows for radial force reduction. Additionally, other complications may come with the design of the rotor ribs and curved pole designs. The rotor rib design would require rotor stress analysis to ensure structural integrity would be preserved for the thin rib. Also, the complexity involved in the shaping of the curved pole shapes would require modifications to the control techniques when the motor is excited with dynamic currents. The torque, radial force and performance ratios for each design are compared in Figs. 4.28 and 4.29.

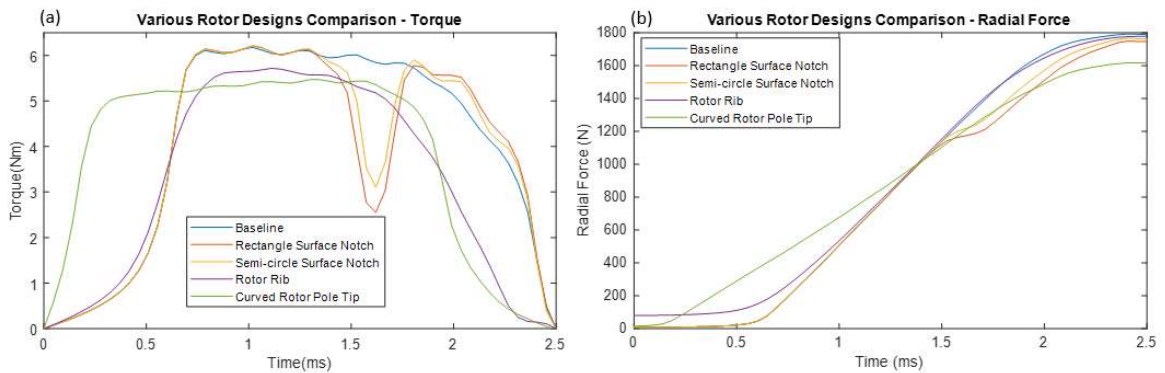


Fig. 4.28 Comparison of the various rotor modifications (a) torque and (b) radial force

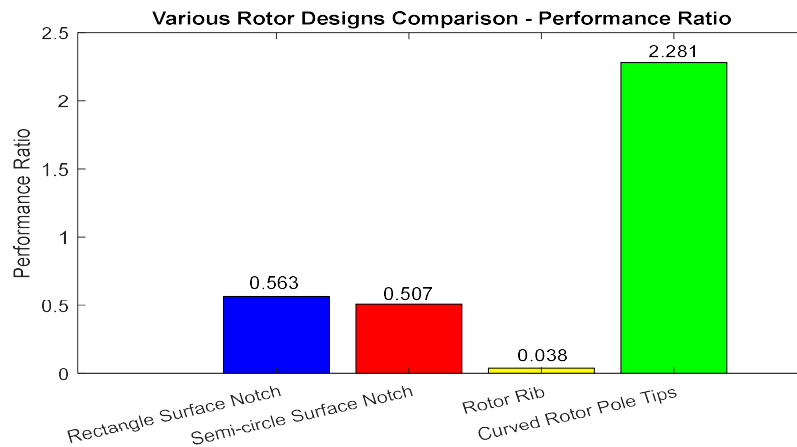


Fig. 4.29 Performance ratio comparison of the various rotor modifications

From the comparative analysis conducted in this section, a few conclusions can be made:

1. The best shape for a rotor window in terms of best performance ratio is a circle.
2. For a circular window of same size and proximity to the airgap, rotor windows have higher performance ratios and a higher impact on the reduction of radial forces for the same amount of torque loss as windows on the stator.
3. Introducing notches on the tips of rotor poles decreases performance significantly as the effective airgap is increased in those regions.
4. Introducing circular windows in the rotor pole is the most effective design to decrease radial forces and minimize torque loss in comparison to the various rotor geometry and modifications investigated in this chapter.

This chapter outlined an extensive comparative review for many design modifications investigated on a four phase 8/6 SRM. The method of comparative analysis used in this chapter allowed many designs to be analyzed for their performance and acoustic noise reduction capabilities. The goal of this chapter was to conclude the best design strategies for stator and rotor modifications which can then be further improved upon using optimization techniques or considerations for specific applications.

## **Chapter 5**

# **Acoustic Noise Reduction in the 8/6 SRM Using Structural Design Methods**

This chapter extends upon the best design techniques investigated in Chapter 4 to create design solutions that decrease the acoustic noise produced in a four phase 8/6 SRM. Modifications to the stator-housing system aim to reduce acoustic noise with a minimal increase in the assembly mass. The modifications to the rotor aim to reduce the radial force magnitude while preserving torque performance as much as possible. This is done using parametric modelling to sweep for ideal location and sizing for circular windows and geometries introduced to the rotor. The flowchart for the procedures of design strategies implemented in this chapter are organized in Fig. 5.1.

### **5.1 Stator-Housing Design**

The stator-housing investigations in Chapter 4 concluded the best design techniques for modifications to the stator-housing system to reduce acoustic noise. Specifically, the increase in number of bolts and flange mounts resulted in significant increase of stiffness in the system. Additionally, the stator back iron notches and octagonal shapes of the stator yoke improved the acoustic noise performance of the machines well. Although significant acoustic noise reduction was achieved by a few designs, one critique of the methods is how much extra mass they add to the system. Therefore, this section aims to improve upon those

investigated techniques with minimal mass increase. Two designs were improved upon and compared to the original baseline design.

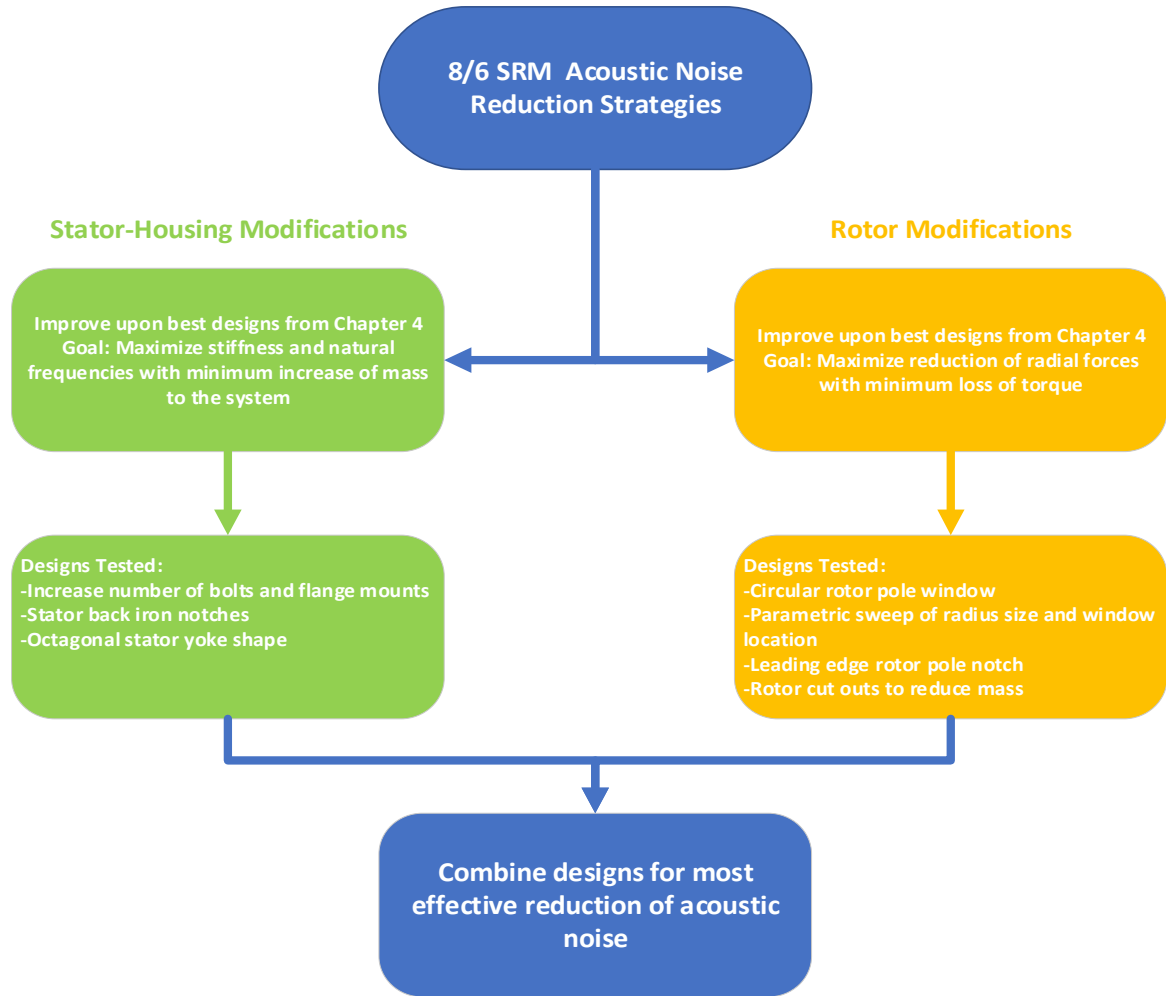


Fig. 5.1 Acoustic noise reduction strategies flowchart

Design I: The first design considered combined the increase in bolts and flange mounts with stator back iron notches. With the systems mass in consideration, the stator's outer diameter was increased from 85 mm to 86.75 mm to make the stator's mass with the cut-

outs as equal to the original stator mass as possible. An exploded view of the considered design is shown in Fig. 5.2.

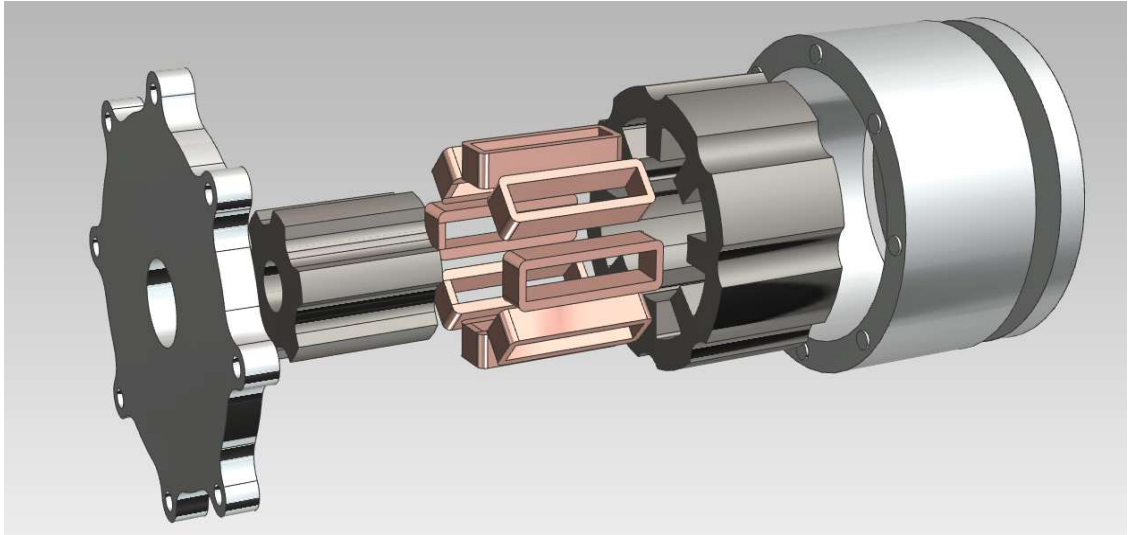


Fig. 5.2 Exploded view of Design I

When compared to the baseline design, this design has significant improvement in stiffness and acoustic noise reduction. The natural frequencies of mode 2 increased to 3491.6 Hz and 3492.5 Hz from the baseline design's 3030 Hz and 3551 Hz, which can be seen in Fig. 5.3. An observation from this analysis is the introduction of 8 bolts makes the system stiffer and more uniform for the housing areas aligned with the stator teeth. As a result, the vibration mode (2,1) is calculated for two very similar natural frequencies that are close together. This differs from the previous investigated designs with the 4 bolts as two mode (2,1) natural frequencies existed far apart from each other. This was due to the system having higher stiffness in the areas aligned with the 4 bolts and lower stiffness in the areas that did not have the bolt support.



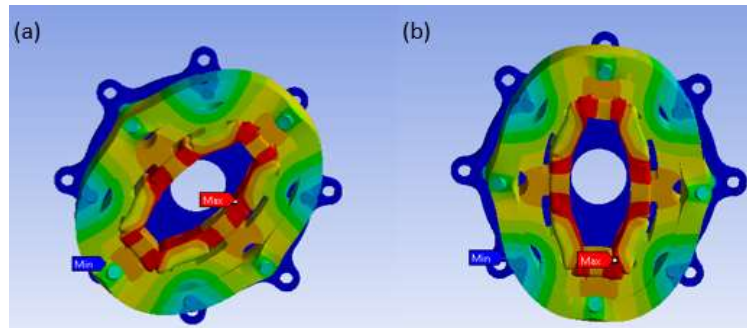


Fig. 5.3 Design I vibration mode (2,1) at (a) 3491.6 Hz and (b) 3492.5 Hz

Design II: The second design considered the octagonal shape of the stator, but with minimal mass increase. The back iron area for Design II increased only in the regions behind the winding slots of the baseline stator with outer radius of 85 mm. This geometry was made by overlapping the smallest regular octagon shape with the original stator outer radius of 85 mm. Similar to Design I, stator back iron slots are included, along with the use of 8 bolts and 8 flange mounts. This design resulted in a minor increase of 0.39 kg in stator mass compared to the baseline design. However, the stiffness of Design II was significant as the natural frequencies further increased to 3586.4 Hz and 3587.8 Hz from the baseline design's 3030 Hz and 3551 Hz and can be seen in Fig. 5.4.

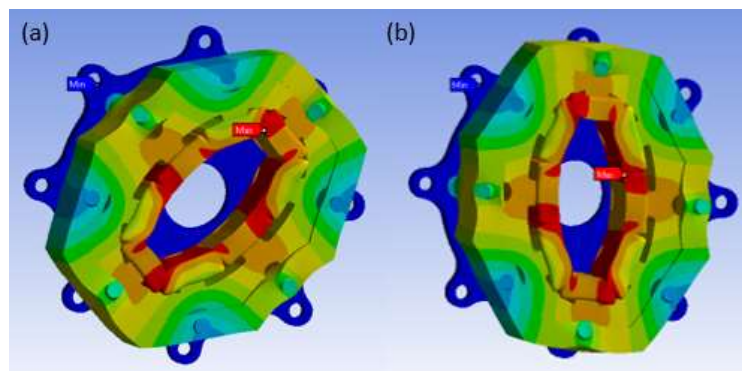


Fig. 5.4 Design II vibration mode (2,1) at (a) 3586.4 Hz (b) 3587.8 Hz

For acoustic noise performance comparison, both Design I and II were simulated at the same dynamic operating condition as the baseline designs. The EM performance of the motor did not change using these design candidates. Both designs had significant reductions in produced acoustic noise due to their increased stiffness. The maximum SPL was reduced from baseline 89.3 dB to 71.24 dB and 67.78 dB for Designs I and II respectively. Additionally, the total SPL reduced from 89.89 dB to 76.27dB and 73.88dB. The acoustic noise comparisons can be viewed in Fig. 5.5. It was observed that the characteristics of the produced acoustic noise also change due to the shift in mode 2 natural frequencies as the peak for Design I and II occurs at 3400 Hz. This frequency corresponds to the (102<sup>nd</sup>,2) radial force density harmonic as seen in Fig. 5.6. This illustrates the effectiveness of pushing natural frequencies higher as higher potential overlapping harmonics will have lower amplitude. The baseline design has maximum SPL at 2600 Hz and a second peak at 3000 Hz which correspond to the (78<sup>th</sup>,2) and (90<sup>th</sup>,2) harmonics. For comparison, the amplitudes of the (78<sup>th</sup>,2) and (90<sup>th</sup>,2) harmonics are 154.45 N/m<sup>2</sup> and 127.64 N/m<sup>2</sup>, compared to an amplitude of 95.40 N/m<sup>2</sup> for the (102<sup>nd</sup>,2) harmonic.

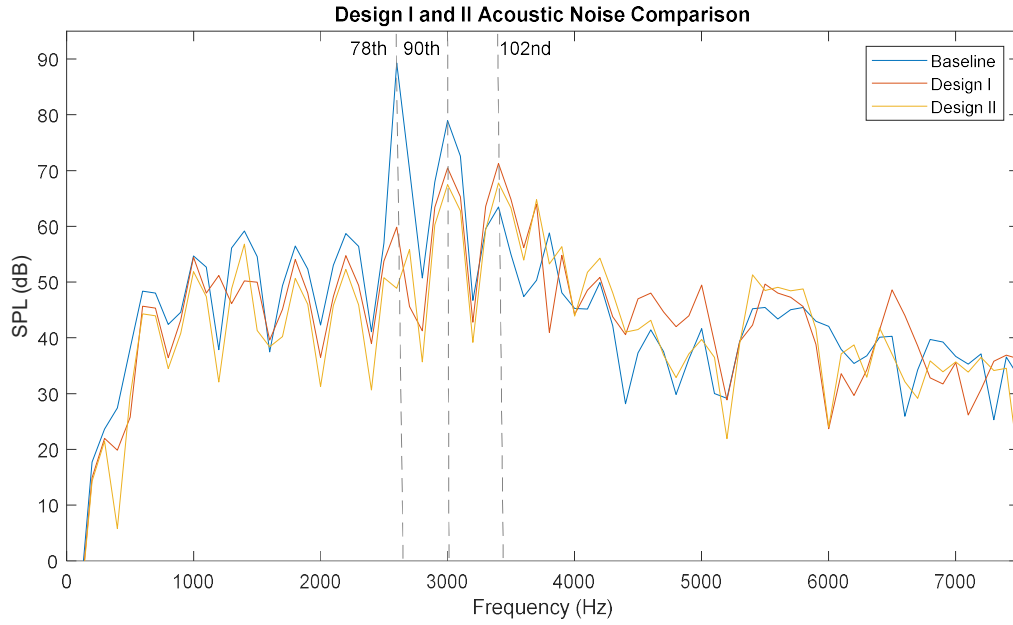


Fig. 5.5 Acoustic noise comparisons for Designs I and II

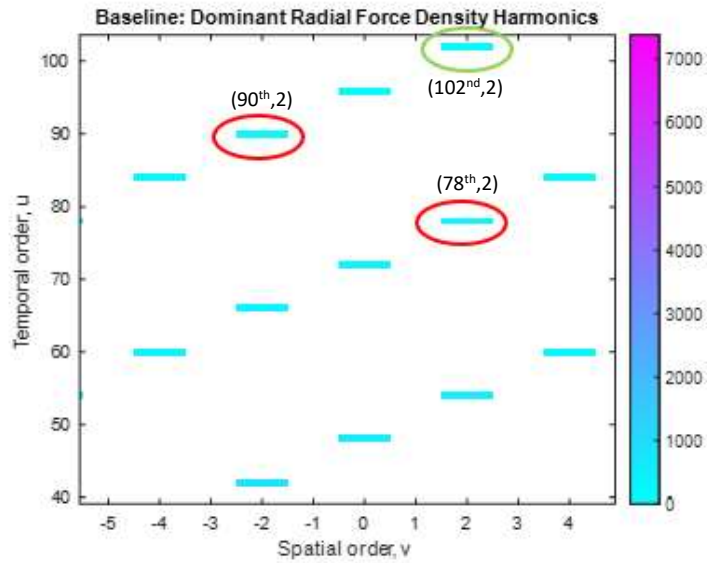


Fig. 5.6 Radial force density harmonics responsible for resonance overlap and peak acoustic noise

The goal of these designs was to achieve lower acoustic noise produced by the motor for the same operating condition, while minimizing the increase in mass. These design candidates were effective at reducing acoustic noise, while also adding minimal mass to the original design. A comparison for the total mass of Designs I and II can be seen in Table 5.1 which includes the rotor, stator, housing, and end plate components. Ultimately, Design II is considered as the more effective design, as the acoustic noise reduction improvement is significant for only a 0.67 kg increase in mass.

Table 5.1 Designs I and II component and total mass comparison

Design	Rotor Mass	Stator Mass	Housing Mass	Endcaps Mass	Total Mass
Baseline	2.84 kg	7.48 kg	3.36kg	3.79kg	17.47kg
Design I	2.84 kg	7.48 kg	3.42 kg	3.89kg	17.64kg
Design II	2.84 kg	7.87 kg	3.53kg	3.89kg	18.14kg

## 5.2 Rotor Modifications for Acoustic Noise Reduction

### 5.2.1 Iteration I

Once the best stator design was determined from Section 5.1, further rotor window investigations were conducted. Firstly, a parametric analysis was applied to the sizing and position of the circular window. A parametric sweep for all possible combinations within defined constraints was conducted in Maxwell using the same operating condition as previously investigated in Chapter 4, which is 2000 rpm at a current reference of 21.21 A. The goals for the sweep targeted a 1.25% or less decrease in average torque while achieving 5% or greater decrease in radial forces. These goals were chosen to try to achieve

performance ratios of 4.0 or higher, which from the initial parametric sweeps conducted in Chapter 4 is a good cut-off value for high trade-offs between torque and radial force reduction. The parameter variables chosen to sweep for include the radius of the circle and the distance from the center of the window to the airgap. The variables for the radius of the circle range from 0.5 mm to 3 mm by steps of 0.25 mm. The variables for distance from airgap ranged from 1 mm to 4 mm by 0.25 mm. The torque and radial force profiles from the results of the various combinations from the parametric sweep are shown in Fig. 5.7.

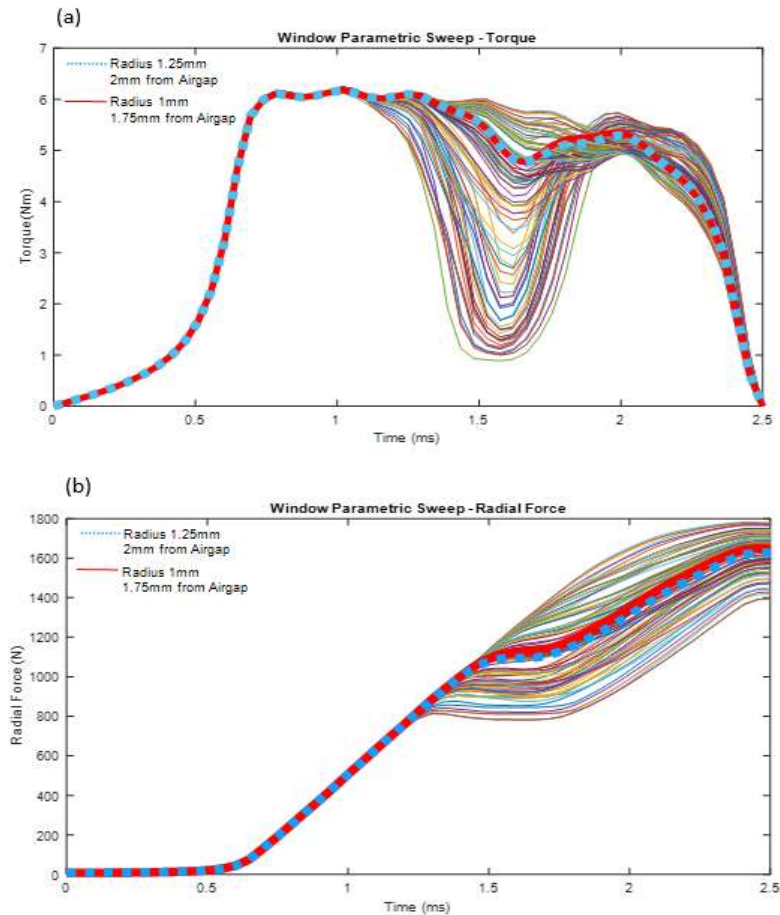


Fig. 5.7 Parametric sweep for size and location of the circular rotor window (a) torque (b) radial force

From the parametric simulations, the best combination of parameters included a circle radius of 1.25 mm at a distance of 2 mm from the airgap. This resulted in an average torque of 4.0491 Nm, a 1.24 % reduction while reducing the maximum radial force to 1694.93 N, a 5.44 % reduction for a performance ratio of 4.39. Up to this point all rotor modification simulations have been conducted using single phase static simulations for simplicity and lower computation cost. The best design was then tested with the dynamic currents that were shown in Fig. 4.5 in Chapter 4 for 2000 rpm. The dynamic simulation resulted in an increase in both torque loss and radial force reduction due the dynamic behaviour of the current control. For the best design chosen with a radius of 1.25 mm at a distance of 2 mm from the airgap, the average torque for the dynamic simulation resulted in a 3.99% loss in torque for a 13.2% decrease in radial forces. The comparison to the baseline dynamic torque and radial force profile is shown in Fig. 5.8.

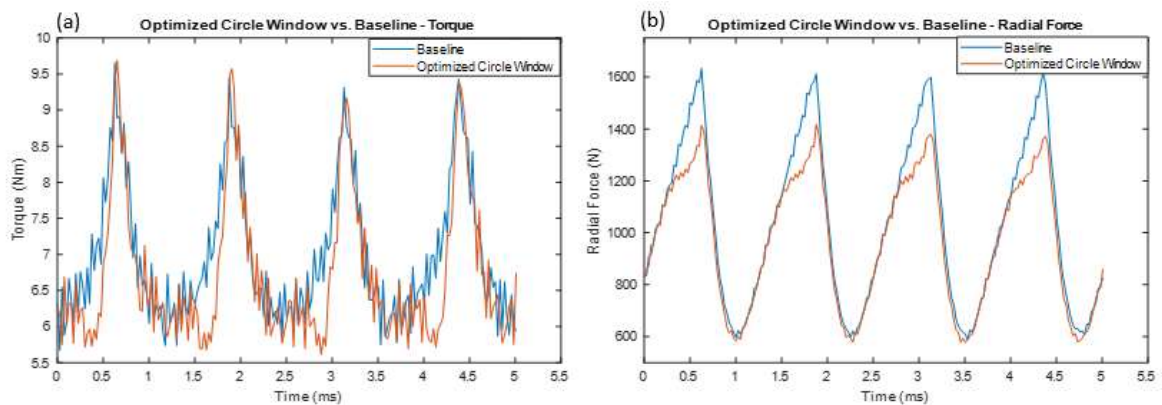


Fig. 5.8 Dynamic EM results for the optimal circular rotor window (a) torque and (b) radial force

It was evident that the impacts of the torque and radial force losses intensified in the dynamic simulation compared to the static analysis, as the performance ratio for the dynamic simulation dropped to 3.31. When both torque profiles were compared to the dynamic current it was observed that the decrease in torque comes from the slower build up to maximum torque during the phase overlap as a result of the circular window in the rotor. The torque profile overlapped with the phase currents can be seen in Fig. 5.9.

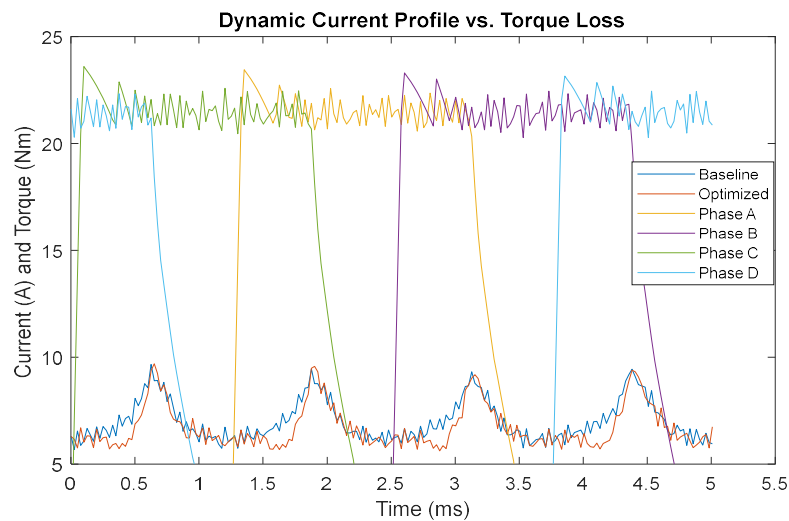


Fig. 5.9 Dynamic current profile vs. torque

### 5.2.2 Iteration II

As the dynamic simulations amplified the torque loss from the static simulations, further investigations were necessary for a better design. Specifically, it was decided to have stricter goals from the static simulations as the losses are amplified in the dynamic simulations. The results from the first iteration were then reviewed for the best combination of parameters with 1% or less loss in torque with the highest performance ratio. The best

combination with less than 1% loss in torque included a radius of 1 mm at 1.75 mm distance from the airgap. The torque loss was 0.835% with a 3.424% decrease in radial forces for a performance ratio of 4.098. Although the static torque loss is less than 1%, further investigations were conducted to see if any additional radial force could be reduced without sacrificing much torque.

Based on [55], a technique used for reducing torque ripple in SRMs introduces a notch on the leading edge of an SRM. The goal of this design is to reduce the fringing flux based on the modification to the SRMs inductance profile. To analyze this technique, a notch was introduced to the leading edge of the rotor pole with the best circular window design. For simplicity, the same dimensions of the circular window at the center of the pole were used but the window was offset towards the leading edge of the rotor (CCW) to notch the corner and as shown in Fig. 5.10.

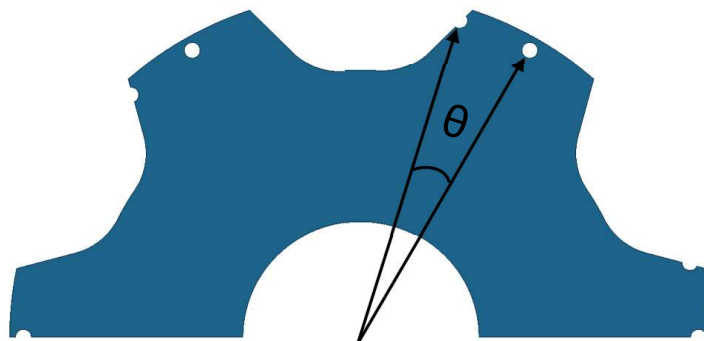


Fig. 5.10 Introduced notch to the leading edge of the rotor pole

The offset angle  $\theta$  was then parametrically swept from  $11.5^\circ$  from the center of the pole to  $13.5^\circ$  by  $0.25^\circ$  increments to study the impact on torque and radial forces. The best result



came from an offset angle of  $13^\circ$ , the swept results for torque and radial forces can be seen in Fig. 5.11.

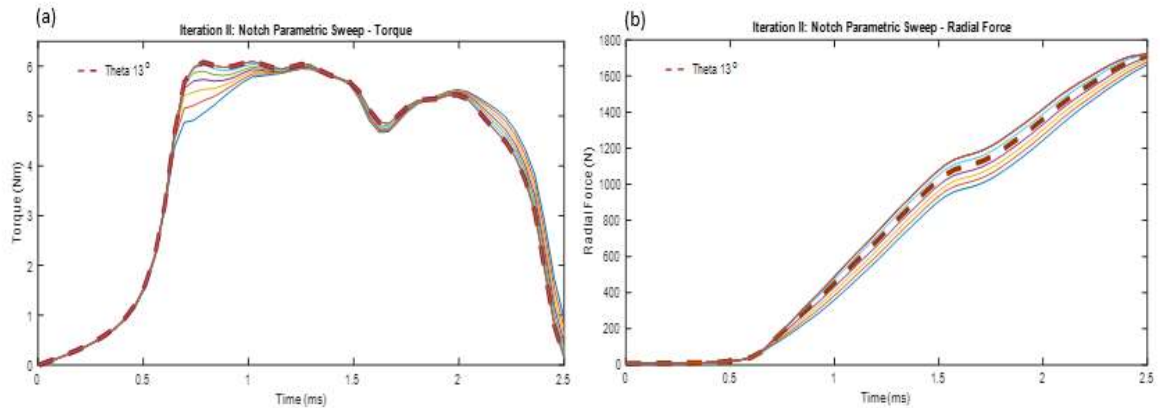


Fig. 5.11 Parametric sweep for the angle of the leading edge notch (a) torque (b) radial force

For the best notch located at a  $13^\circ$  offset, the resulting loss in torque was 0.864% with a 3.89% decrease in radial force having a performance ratio of 4.498. This is a higher performance ratio than the best circular window option from iteration I while also keeping the torque loss under 1%. The resulting dynamic current simulations with this design performed better than the initial single circle window design. The dynamic simulation resulted in a torque loss of 4.07% but managed to obtain a 16.32% decrease in radial force, achieving a performance ratio of 4.01. This is significantly better than the single circle window design which had a performance ratio of 3.31. The dynamic torque and radial force profiles for the baseline, single circle window and notched designs are seen in Fig. 5.12. By observing Fig. 5.12, it can be seen that the iteration II torque profile matches very similarly for iteration I, yet the radial force for iteration II is noticeably decreased.

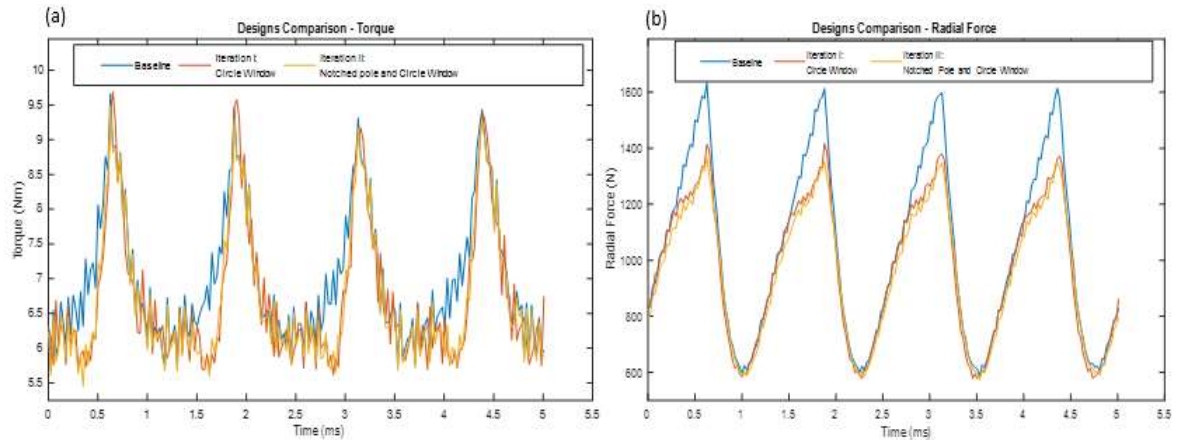


Fig. 5.12 Dynamic simulation comparisons for iterations I and II (a) torque and (b) radial force

### 5.2.3 Rotor Mass Reduction

The final modification made to the rotor geometry was to decrease the mass of the motor assembly. Rotor cut-outs can be made close to the shaft that have minimal impact on performance [56]. Multiple iterations were made for choosing the size and location of the cut-outs, with the goal of minimally impacting the torque. The final chosen cut-out design has dimensions as outlined in Fig. 5.13 and is symmetrically replicated 6 times around the rotor. The average torque from the static simulation without the cut-outs was 4.0698 Nm, compared to an average torque of 4.0665 Nm with the cut-outs, less than a 0.09% decrease. Similarly for the dynamic simulation the torque for the designs without the cut-outs is 6.7168 Nm, whereas the torque for the design with the cut-outs was 6.7125 Nm.

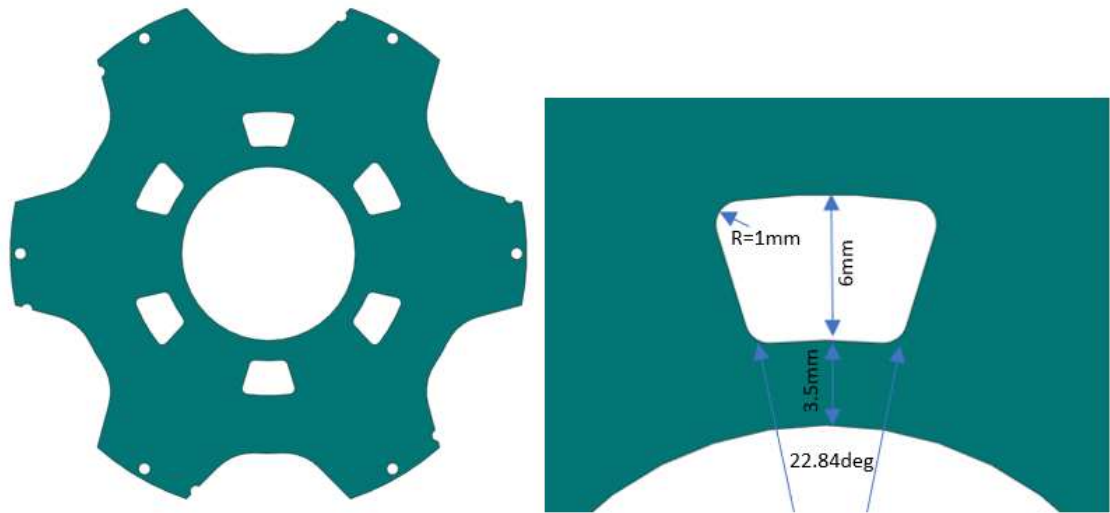


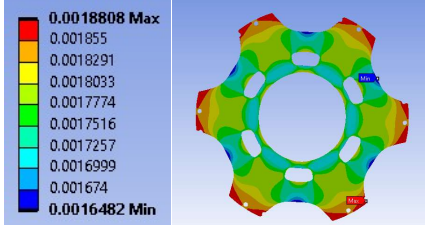
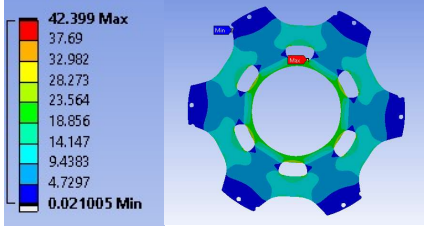
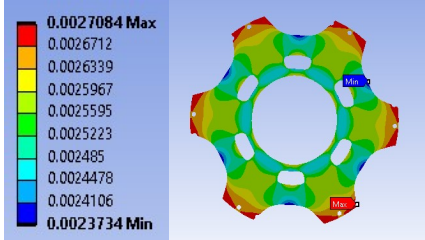
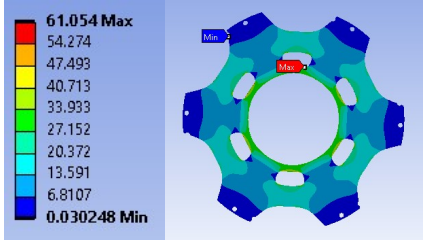
Fig. 5.13 Rotor lamination with cut-outs to reduce mass

An important consideration for implementing these design changes is to evaluate the impact on rotor stress and deformation. This SRM design has as small airgap of 0.35 mm, so radial deformation with these design considerations should not exceed 0.035 mm, or 10% of the airgap [57]. The maximum von-mises stress should also not exceed the yield stress of the rotor lamination material, which for this rotor lamination material of 35H300 is 520 MPa. Both criteria are to ensure no motor failures would occur due to the rotor modifications. Specifically, if the deformation exceeds the airgap size, it could cause rotor collision with the stator and if the yield stress exceeds maximum allowable limits, cracks could form and cause the rotor material to fracture [56].

To validate these rotor modifications will not result in failure of the motor, a steady state structural FEA analysis was conducted on a rotor lamination of 0.35 mm. The analysis was conducted at 12000 rpm and 14400 rpm which is the maximum speed and burst speed

(1.2x) of the motor. These are both very aggressive speeds for the motor as it would never operate over 12000 rpm, but to illustrate the robustness of the design the specifications are simulated at these high speeds. For both speeds, the maximum deformation and stress are well below the acceptance criteria and validate that these rotor modifications will not cause any mechanical failures. The maximum deformations for 12000 rpm and 14400 rpm are 1.8  $\mu\text{m}$  and 2.7  $\mu\text{m}$  respectively along with the maximum von-mises stress of 42.39 MPa and 61.05 MPa. These results can be seen in Table 5.2.

Table 5.2 Rotor lamination deformation and stress analysis

Speed	Deformation (mm)	Von-mises Stress (MPa)
12000 rpm		
14400 rpm		

### 5.3 Final Design Modifications

For the final design, the best stator-housing assembly from Section 5.1 is combined with the rotor modifications made in Section 5.2. The assembly components can be seen in the exploded view in Fig. 5.14.

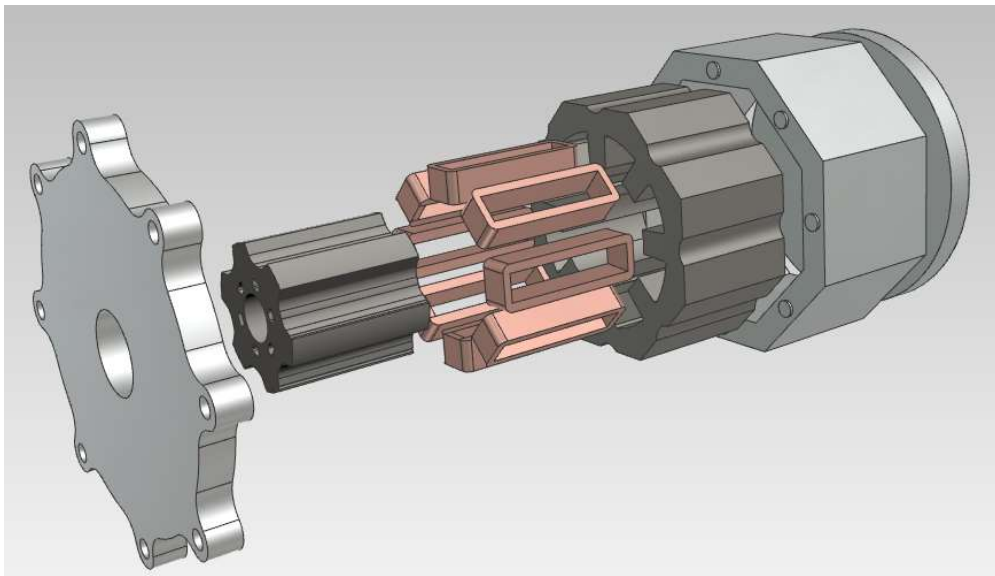


Fig. 5.14 Exploded view of the Final Design for the 8/6 SRM

The goal of this design was to significantly decrease the acoustic noise produced by the motor while preserving performance as much as possible. Additionally, many considerations have been made to increase the stiffness of the system with a minimal increase in mass. This design was evaluated to compare many performance criteria. Specifically, torque, radial force, SPL, and total assembly mass were the main evaluated criteria when designing this motor. The following results illustrate the success this design had at accomplishing these goals.

In comparison to the baseline original design, this design reduces the maximum acoustic noise SPL from 89.30 dB to 67.14 dB, which is more than a 22 dB or 24.82% decrease. Similarly, the total SPL of the motor was reduced from 89.89 dB to 72.33 dB, a 17.56 dB or 19.53% decrease. The total mass of the design is 17.93 kg, only 0.46 kg heavier than the initial baseline design. The torque generated at the 2000 rpm operating condition saw a reduction of average torque from 6.99 Nm baseline design to 6.70 Nm, a 4.148% decrease. Therefore, this design was able to achieve almost a 20% decrease in acoustic noise by adding only 0.46 kg of mass and while only losing 4% of torque at this operating condition. The resulting acoustic noise SPL along with the torque and radial force waveforms can be seen below in Figs. 5.15 and 5.16.

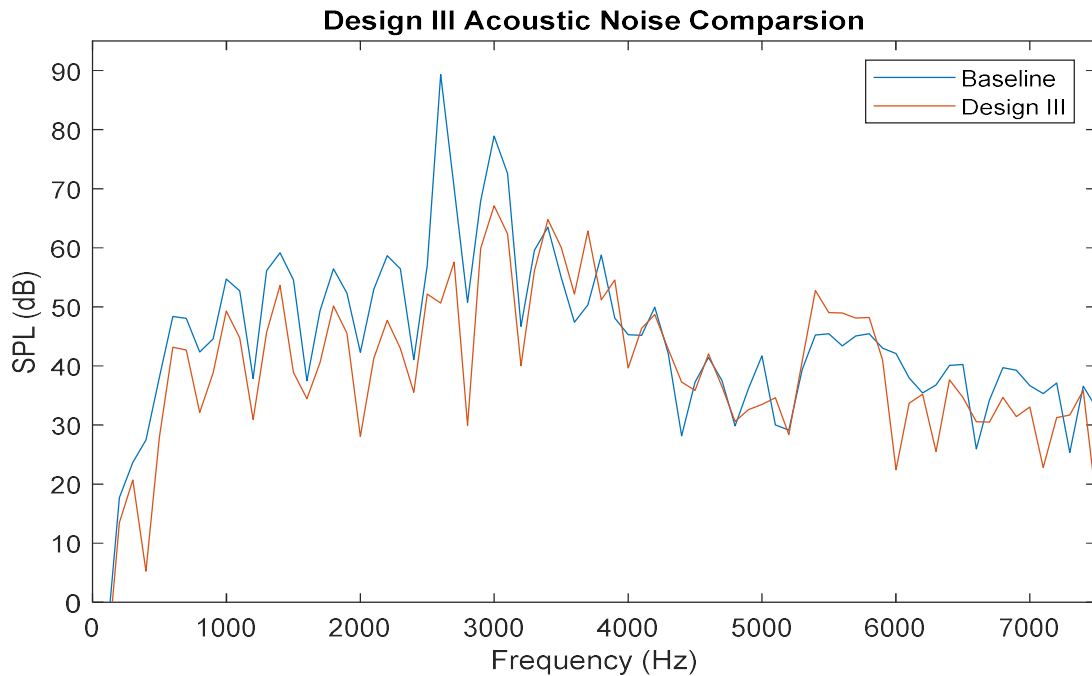


Fig. 5.15 Acoustic noise comparison of the Final Design to the baseline design of the 8/6 SRM

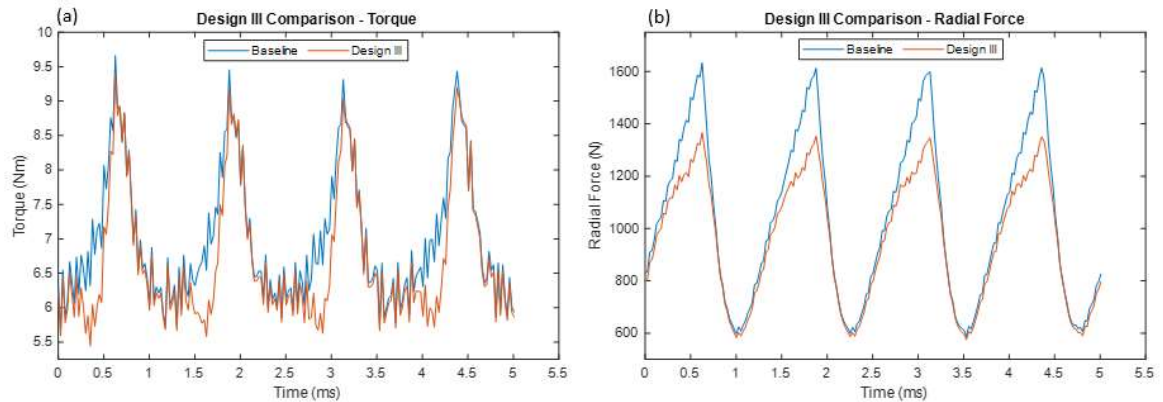


Fig. 5.16 Final Design EM performance analysis (a) torque and (b) radial force

The focus of this thesis was on mechanical design: therefore, the phase currents have remained the same for all designs to normalize results. However, this 4% loss in torque is easily regained with a slight increase in referenced current magnitude or current control. For example, if the referenced phase currents are increased from an RMS value of 15 A (21.21 A) to an RMS value of 15.45 A (21.85 A) using the same current control technique with the same conduction angles, the torque loss can be completely mitigated.

For final evaluations of the proposed design, performance characteristics are compared for Designs I, II, III and IV. Design IV is simply Design III with the modified phase current RMS value. The following characteristics are outlined in Table 5.3: Average Torque, Torque Ripple, Maximum Radial Force, Total SPL, Torque per RMS Current, Total Assembly Mass, and Torque Density.

Table 5.3 Performance evaluations for the best 8/6 SRM designs

Design	Average Torque	Torque Ripple	Maximum Radial Force	Acoustic Noise (Total SPL)	Torque/RMS Current	Total Assembly Mass	Torque Density (Nm/Kg)
Baseline	6.99 Nm	57.00%	1633.51 N	89.89 dB	0.80	17.48 Kg	0.39988
Design I	6.99 Nm	56.83%	1632.94 N	76.27 dB	0.80	17.64 Kg	0.39626
Design II	6.99 Nm	55.99%	1634.91 N	73.88 dB	0.80	18.14 Kg	0.38533
Design III	6.70 Nm	59.00%	1367.24 N	72.32 dB	0.77	17.94 Kg	0.37346
Design IV	7.01 Nm	59.12%	1400.93 N	72.38 dB	0.78	17.94 Kg	0.39074

In comparison to the baseline motor design, Design III improves the acoustic noise of the four phase 8/6 SRM best of all design candidates. However, to supplement the loss in torque, Design IV can achieve the same average torque as the baseline design while also significantly decreasing the produced acoustic noise. Furthermore, Design IV has a better torque per RMS current and torque density compared to Design III.



## Chapter 6

# Conclusions and Future Work

### 6.1 Thesis Summary

Although switched reluctance machines possess significant advantages over permanent magnet and induction machines for automotive applications, they fall short in a few areas that have prevented their implication thus far. The operational characteristics of SRMs are known to create high torque ripple and high acoustic noise which are both undesirable for traction applications. For this reason, design techniques can be implemented to reduce the acoustic noise produced by these machines. In this thesis, design techniques that increase structural stiffness and reduce the magnitude of produced radial forces are thoroughly investigated.

In Chapter 2, the fundamental operating characteristics of SRMs have been outlined and the modelling techniques for the non-linear operation of SRMs is explained. This chapter provides a base understanding of how SRMs behave.

In Chapter 3, the fundamentals of acoustic noise production for SRMs are explained. This includes the fundamentals of modelling and analyzing radial forces, vibrations and acoustic noise produced by SRMs. The radial force analysis outlined in Chapter 3 breaks down how spatial and temporal components of radial force density waves can cause resonance excitations of SRMs natural frequencies which create excessive vibrations and acoustic

noise. Additionally, an extensive network of multiphysics FEA simulations used to analyze acoustic noise is introduced. The FEA acoustic noise modelling techniques are verified from experimental results with a four-phase 8/6 SRM.

Based on inspiration from an extensive literature review, Chapter 4 applies the NVH FEA toolchain to analyze and compare existing techniques for SRM acoustic noise reduction. By defining a baseline design for a four phase 8/6 SRM, design modifications are applied to the SRM to reduce acoustic noise. Two categories of design considerations were investigated separately: stator-housing modifications and rotor modifications. The goal of the modifications made to the stator-housing system were to increase the stiffness of the motor assembly to increase natural frequencies and reduce resonance excitations by changing the stator yoke shape and investigating various assembly contact constraints. The rotor modifications aimed to reduce the magnitude of the produced radial forces by introducing notches and windows to the rotor poles. Through a means of comparative analysis, it was determined that octagonal stator yoke shapes and an increase in bolt contacts will significantly improve the stiffness of an SRM design while the introduction of a circular shaped window is the most effective rotor modification in terms of radial force reduction and torque loss trade offs. Additionally, it was found that introducing notches to the stator back iron yoke reduces the propagation of vibrations from the stator outer circumference to the housing surface due to reduced contact surface area. The application of these designs was analyzed with both static single phase EM simulations and dynamic conditions to compare to the baseline design.

Finally, once the best design strategies were determined from Chapter 4, Chapter 5 continues by improving the acoustic noise and vibration performance of an 8/6 SRM using the best candidates. Specifically, the goals for the final designs introduced in chapter 5 included reducing acoustic noise with minimal increase in total assembly mass. The introduction of stator back iron notches and an octagonal stator yoke shape proved to be the most effective stator design. The stator-housing connections modifications included increasing the number of bolt and flange mount connections to significantly increase the stiffness of the design. The rotor pole circular windows size and location based on proximity to the airgap are iteratively designed using parametric sweeps. A leading-edge pole notch is introduced to the rotor to further increase the radial force reduction of the design. The combinations of various window and notch designs targeted a performance ratio of 4.0 or higher with the goal to maintain 1% or less torque loss for the static simulations. Both design techniques applied to the motor are combined to compare the dynamic performance of the four phase 8/6 SRM at 2000 rpm to the original design. The results found that the best design was able to achieve a 17.57 dB reduction (19.54%) in total SPL while losing only 4.15% torque. Additionally, a simple current control modification is suggested to regain the lost torque.

Every proposed design in Chapter 5 resulted in significant improvements on the acoustic noise produced for SRMs and are combinations of the best practices as determined by an extensive comparative analysis in Chapter 4. Although this thesis focused on the acoustic noise reduction of a four phase 8/6 SRM at 2000 rpm, the implemented design techniques outlined in this thesis provide excellent direction on potential solutions to reduce acoustic

noise issues for various types of SRMs. Additionally, the methodologies implemented to understand the fundamental behaviours of radial forces combined with the natural frequencies of an SRM and how they relate to acoustic noise production serve as an outstanding reference for any engineer interested in improving SRMs.

## **6.2 Future Work**

As the proposed design shows promising results in regards to acoustic noise reduction, further research is required to find optimal solutions. This thesis focused on a 2000 rpm 15 RMS current operating condition which operates in the saturation region for the four phase 8/6 SRM but did not consider higher speeds or operation conditions. To further justify the implemented design techniques, the same design modifications should be analyzed at higher speeds and more aggressive operating conditions to see the performance impacts over a wider range. The various designs tested followed a baseline four phase 8/6 SRM, however for ultimate NVH designs, pole slot combinations and various SRM topologies should be compared to decide on the best starting design based on application.

Acoustic noise analysis is a unique field as qualitative measurements are difficult to analyze. There exists an entire field related to noise called psychoacoustics which study the perception of sound. Noise can be analyzed for metrics such as harshness, sharpness and annoyance which can all be crucial to the behaviour of noise produced by SRMs. This thesis can be expanded upon by investigating psychoacoustic indicators and developing performance criteria considering more metrics than measured SPL.

Furthermore, the design processes used in this thesis can be improved upon. Specifically, the performance of a SRM is sensitive to the notch and window rotor modifications and require more advanced optimization techniques to provide the best solutions possible. The design techniques applied in this thesis included comparative analysis and parametric sweeping for various combinations of size and location of the geometry modifications. However, if more advanced optimization algorithms are applied to a completely parameterized SRM model, many more variables could be considered such as notch geometry and window angle. Also, the relationship between radial force magnitude and acoustic noise reduction should be further analyzed. Although reduction of the radial force magnitude was a goal for the rotor modifications, if the characteristics that create the dominant radial force densities could be modified through design, this may have a greater impact on acoustic noise than simply reducing the magnitude.

Lastly, ideally a prototype of the motor design would be manufactured and tested experimentally. For this motor design, the effectiveness of the acoustic noise reduction techniques would be best quantified with a physical prototype to experimentally validate with the FEA model results. In the same way, manufacturability is an aspect that should be investigated to improve upon these findings. Depending on application, the complexity of SRM designs can be quite costly. Manufacturability and cost need to be investigated for the implemented acoustic noise reduction design techniques in order to evaluate all aspects of the machine design process. The manufacturing process can also be compared to evaluate the most efficient procedures to create these designs. For example, for the rotor and stator laminations, a cost benefit analysis on the use of laser cutting versus retooling

for stamping would assist in manufacturing decisions depending on application and quantity.

## References

- [1] U.S. Energy Information Administration. Energy-Related CO<sub>2</sub> Emission Data Tables. March 2, 2021. [Online]. Available: <https://www.eia.gov/environment/emissions/state/>. Accessed: March 27, 2021.
- [2] B. Bilgin, J. Jiang, A. Emadi, “Switched Reluctance Motor Drives: Fundamentals to Applications,” Boca Raton, FL, USA: CRC Press, ISBN: 9781138304598
- [3] A. Emadi, Young Joo Lee, and K. Rajashekara, “Power Electronics and Motor Drives in Electric, Hybrid Electric, and Plug-In Hybrid Electric Vehicles,” *IEEE Transactions on Industrial Electronics*, vol. 55, no. 6, pp. 2237–2245, 2008. [Online]. Available: <http://ieeexplore.ieee.org/lpdocs/epic03/wrapper.htm?arnumber=4493430>
- [4] B. Bilgin, A. Emadi, and M. Krishnamurthy, “Design considerations for switched reluctance machines with a higher number of rotor poles,” *IEEE Transactions on Industrial Electronics*, vol. 59, no. 10, pp. 3745–3756, 2012.
- [5] A. Emadi, Ed., *Advanced Electric Drive Vehicles*. Boca Raton, FL: CRC Press, 2015.
- [6] H. Li, “Torque Ripple Minimization in Switched Reluctance Machines (M.A.Sc. Dissertation),” McMaster University, Hamilton, Ontario Canada. July 2017.
- [7] K. Kiyota, T. Kakishima, and A. Chiba, “Comparison of test result and design stage prediction of switched reluctance motor competitive with 60-kW rare-earth PM motor,” *IEEE Transactions on Industrial Electronics*, vol. 61, no. 10, pp. 5712–5721, 2014.
- [8] B. Bilgin, A. Emadi, and M. Krishnamurthy, “Comprehensive evaluation of the dynamic performance of a 6/10 SRM for traction application in PHEVs,” *IEEE Transactions on Industrial Electronics*, vol. 60, no. 7, pp. 2564–2575, 2013.
- [9] H. Li, B. Bilgin, and A. Emadi, “An improved torque sharing function for torque ripple reduction in switched reluctance machines,” *IEEE Transactions on Power Electronics*, pp. 1–1, May 2018.
- [10] J. Ye, B. Bilgin, and A. Emadi, “An offline torque sharing function for torque ripple reduction in switched reluctance motor drives,” *IEEE Transactions on Energy Conversion*, vol. 30, no. 2, pp. 726–735, June 2015.
- [11] D. Lee, J. Liang, Z. Lee, and J. Ahn, “A simple nonlinear logical torque sharing function for low-torque ripple sr drive,” *IEEE Transactions on Industrial Electronics*, vol. 56, no. 8, pp. 3021–3028, Aug 2009.
- [12] X. D. Xue, K. W. E. Cheng, and S. L. Ho, “Optimization and evaluation of torque-sharing functions for torque ripple minimization in switched reluctance motor drives,” *IEEE Transactions on Power Electronics*, vol. 24, no. 9, pp. 2076–2090, Sept 2009.
- [13] J. Ye, B. Bilgin, and A. Emadi, “An extended-speed low-ripple torque control of switched reluctance motor drives,” *IEEE Transactions on Power Electronics*, vol. 30, no. 3, pp. 1457–1470, March 2015.

- [14] J. Furqani, M. Kawa, K. Kiyota, and A. Chiba, "Comparison of current waveforms for noise reduction in switched reluctance motors," in *Proc. IEEE Energy Conversion Congress and Exposition (ECCE)*, Cincinnati, OH, Oct. 2017, pp. 752-759.
- [15] C. Ma, L. Qu, R. Mitra, P. Pramod, and R. Islam, "Vibration and torque ripple reduction of switched reluctance motors through current profile optimization," *2016 IEEE Applied Power Electronics Conference and Exposition (APEC)*, pp. 3279-3285, 2016.
- [16] M. Kawa, K. Kiyota, J. Furqani, and A. Chiba, "Acoustic noise reduction of a high efficiency switched reluctance motor for hybrid electric vehicles with novel current waveform," in *Proc. IEEE International Electric Machines and Drives Conference (IEMDC)*, Miami, FL, May 2017, pp. 1-6.
- [17] ] K. Okabayashi, K. Honda, T. Sugiura, and H. Kakigano, "Noise Reduction using High-switching- frequency Operation with SiC MOSFET for Switched Reluctance Motors."
- [18] A. Hofmann, A. Al-Dajani, M. Bosing, and R. W. De Doncker, "Direct instantaneous force control: A method to eliminate mode-0-borne noise in switched reluctance machines," *Proceedings of the 2013 IEEE International Electric Machines and Drives Conference, IEMDC 2013*, vol. 0, no. Mx, pp. 1009-1016, 2013.
- [19] ] N. Bianchi and M. Dai Pre, "Comparative study of switching controls in vibration and acoustic noise reductions for switched reluctance motor," *IEEE Proceedings-Electric Power Applications*, vol. 150, no. 2, pp. 139-145, 2003. [Online]. Available: [http://digital-library.theiet.org/content/journals/10.1049/ip-epat\\_u20030009](http://digital-library.theiet.org/content/journals/10.1049/ip-epat_u20030009)
- [20] A. Tanabe and K. Akatsu, "Vibration reduction method in SRM with a smoothing voltage commutation by PWM," *9th International Conference on Power Electronics - ECCE Asia: Green World with Power Electronics*, ICPE 2015- ECCE Asia, pp. 600-604, 2015.
- [21] Z. Q. Zhu, X. Liu, and Z. Pan, "Analytical model for predicting maximum reduction levels of vibration and noise in switched reluctance machine by active vibration cancellation," *IEEE Transactions on Energy Conversion*, vol. 26, no. 1, pp. 36-45, 2011.
- [22] A. Dorneles Callegaro, "Radial Force Shaping of Switched Reluctance Motor Drives for Acoustic Noise Reduction (Ph.D. Dissertation)," McMaster University, Hamilton, Ontario, Canada. December 2018.
- [23] D. E. Cameron, J. H. Lang, and S. D. Umans, "The origin and reduction of acoustic noise in doubly salient variable-reluctance motors," *IEEE Transactions on Industry Applications*, vol. 28, no. 6, pp. 1250-1255, Nov 1992.
- [24] C. Ma and L. Qu, "Design considerations of switched reluctance machines for structural vibration reduction," in *Proc. IEEE Transportation Electrification Conference and Expo (ITEC)*, Chicago, IL, June 2017, pp. 598-604.
- [25] P. C. Desai, M. Krishnamurthy, N. Schofield, and A. Emadi, "Novel switched reluctance machine configuration with higher number of rotor poles than stator poles: Concept to implementation," *IEEE Transactions on Industrial Electronics*, vol. 57, no. 2, pp. 649-659, Feb 2010.
- [26] B. Bilgin, A. Emadi, and M. Krishnamurthy, "Comprehensive evaluation of the dynamic performance of a 6/10 srm for traction application in phev," *IEEE Transactions on Industrial Electronics*, vol. 60, no. 7, pp. 2564-2575, July 2013.



- [27] B. Bilgin, "Design considerations for switched reluctance machines with a higher number of rotor poles," *IEEE Transactions on Industrial Electronics*, vol. 59, no. 10, pp. 3745–3756, Oct 2012.
- [28] M. Sanada, S. Morimoto, Y. Takeda and N. Matsui, "Novel rotor pole design of switched reluctance motors to reduce the acoustic noise," *Conference Record of the 2000 IEEE Industry Applications Conference. Thirty-Fifth IAS Annual Meeting and World Conference on Industrial Applications of Electrical Energy (Cat. No.00CH37129)*, 2000, pp. 107-113 vol.1, doi: 10.1109/IAS.2000.881033
- [29] S. Yaman, C. Chen, Z. Zhang and M. Krishnamurthy, "Acoustic Noise and Vibration in Switched Reluctance Machines: A Comparative Study of 12/8 and 8/6 Topologies," *2019 IEEE International Electric Machines & Drives Conference (IEMDC)*, 2019, pp. 1130-1137, doi: 10.1109/IEMDC.2019.8785240.
- [30] D. Tekgun, "Acoustic Noise and Vibration Reduction on Switched Reluctance Machines Through Hole Placement in Stator/Rotor Laminations," The University of Akron, Akron, Ohio, U.S.A. May 2017.
- [31] ] M. Abbasian, M. Moallem, and B. Fahimi, "Double-Stator Switched Reluctance Machines (DSSRM): Fundamentals and Magnetic Force Analysis," *IEEE Trans. Energy Convers.*, vol. 25, no. 3, pp. 589–597, 2010.
- [32] A. H. Isfahani and B. Fahimi, "Multi-physics Analysis of Double Stator Switched Reluctance Machines," *IEEE Energy Convers. Congr. Expo.* 2013, pp. 2827–2833, 2013.
- [33] A. Isfahani and B. Fahimi, "Comparison of Mechanical Vibration Between a Double-Stator Switched Reluctance Machine and a Conventional Switched Reluctance Machine," *Magn. IEEE Trans.*, vol. 50, no. 2, 2014.
- [34] A. Sakuma, M. Kadowaki, H. Ukigai, I. Miki, T. Okamoto and T. Segawa, "Stator structure for noise reduction of switched reluctance motor," *2012 15th International Conference on Electrical Machines and Systems (ICEMS)*, 2012, pp. 1-4.
- [35] Jung-Pyo Hong, Kyung-Ho Ha and Ju Lee, "Stator pole and yoke design for vibration reduction of switched reluctance motor," in *IEEE Transactions on Magnetics*, vol. 38, no. 2, pp. 929-932, March 2002, doi: 10.1109/20.996239.
- [36] Wei Cai, P. Pillay, Zhangjun Tang and A. M. Omekanda, "Low-vibration design of switched reluctance motors for automotive applications using modal analysis," in *IEEE Transactions on Industry Applications*, vol. 39, no. 4, pp. 971-977, July-Aug. 2003, doi: 10.1109/TIA.2003.814559.
- [37] K. Takayama and I. Miki, "Design of switched reluctance motor to reduce acoustic noise," *2016 International Symposium on Power Electronics, Electrical Drives, Automation and Motion (SPEEDAM)*, 2016, pp. 425-429, doi: 10.1109/SPEEDAM.2016.7525830.
- [38] P. O. Rasmussen, J. H. Andreasen and J. M. Pijanowski, "Structural stator spacers-a solution for noise reduction of switched reluctance motors," in *IEEE Transactions on Industry Applications*, vol. 40, no. 2, pp. 574-581, March-April 2004, doi: 10.1109/TIA.2004.824489.
- [39] O. Naderi Samani and B. Ganji, "Noise reduction of switched reluctance motors," *2017 8th Power Electronics, Drive Systems & Technologies Conference (PEDSTC)*, 2017, pp. 300-304, doi: 10.1109/PEDSTC.2017.7910341
- [40] K. Edamura and I. Miki, "Design of stator and rotor for noise reduction of SRM," *2014 17th International Conference on Electrical Machines and Systems (ICEMS)*, 2014, pp. 1871-1874, doi: 10.1109/ICEMS.2014.7013788

- [41] H. Yang, Y. Lim and H. Kim, "Acoustic Noise/Vibration Reduction of a Single-Phase SRM Using Skewed Stator and Rotor," in *IEEE Transactions on Industrial Electronics*, vol. 60, no. 10, pp. 4292-4300, Oct. 2013, doi: 10.1109/TIE.2012.2217715.
- [42] C. Gan, J. Wu, M. Shen, S. Yang, Y. Hu, and W. Cao, "Investigation of Skewing Effects on the Vibration Reduction of Three-Phase Switched Reluctance Motors," *IEEE Trans. Magn.*, vol. 51, no. 9, pp. 1–9, Sep. 2015.
- [43] M. Elamin, Y. Yasa, Y. Sozer, J. Kutz, J. Tylanda and R. L. Wright, "Effects of windows in stator and rotor poles of switched reluctance motors in reducing noise and vibration," *2017 IEEE International Electric Machines and Drives Conference (IEMDC)*, 2017, pp. 1-6, doi: 10.1109/IEMDC.2017.8002375.
- [44] Jie Li, HeXu Sun and Yi Liu, "New rotor structure mitigating vibration and noise in switched reluctance motor," *2010 International Conference on Information, Networking and Automation (ICINA)*, 2010, pp. V2-80-V2-84, doi: 10.1109/ICINA.2010.5636789.
- [45] P. O. Rasmussen, E. C. LaBrush, and J. H. Andreasen, "Interlaminated Damping - A Method for Reduction of Vibration and Acoustic Noise for Switched Reluctance Machines," *Conf. Rec. - IAS Annu. Meet. (IEEE Ind. Appl. Soc.)*, vol. 3, pp. 1531–1539, 2005.
- [46] I. Hasan, Y. Sozer, A. Pina, S. Paul, R. Islam and J. Klass, "Stator design techniques to reduce vibration in permanent magnet synchronous machines," *2017 20th International Conference on Electrical Machines and Systems (ICEMS)*, 2017, pp. 1-6, doi: 10.1109/ICEMS.2017.8056492.
- [47] J.W. Jiang, "Three-Phase 24/16 Switched Reluctance Machine for Hybrid Electric Powertrains: Design and Optimization (Ph.D Dissertation)," McMaster University, Hamilton, 2016.
- [48] M. Ehsani, Y. Gao and A. Emadi, *Modern Electric, Hybrid Electric, and Fuel Cell Vehicles*, Boca Raton: CRC Press, 2009.
- [49] J. W. Jiang, B. Bilgin, and A. Emadi, "Three-phase 24/16 switched reluctance machine for a hybrid electric powertrain," *IEEE Transactions on Transportation Electrification*, vol. 3, no. 1, pp. 76–85, March 2017.
- [50] J. Liang, "Acoustic Noise and Vibrations in Switched Reluctance Motors: Enhanced Modelling (Ph.D . Dissertation)," McMaster University, Hamilton, Ontario, Canada. December 2019.
- [51] Tontechnik-Rechner-sengpielaudio Decibel Table-SPL-Loudness Comparison Chart. [Online] Available: <http://www.sengpielaudio.com/TableOfSoundPressureLevels.htm>. Accessed: May 7,2021.
- [52] S. Marburg and B. Nolte, *Computational Acoustics of Noise Propagation in Fluids: Finite and Boundary Element Methods*, Germany: Springer, ISBN: 978-3-540-77448-8, Feb. 2008.
- [53] A. D. Callegaro, B. Bilgin, and A. Emadi, "Radial force shaping for acoustic noise reduction in switched reluctance machines," *IEEE Transactions on Power Electronics*, vol. 34, no. 10, pp. 9866-9878, Oct. 2019
- [54] K. Kiyota, T. Kakishima, A. Chiba, and M. A. Rahman, "Cylindrical rotor design for acoustic noise and windage loss reduction in switched reluctance motor for HEV applications," *IEEE Transactions on Industry Applications*, vol. 52, no. 1, pp. 154–162, Jan 2016.

- [55] Jin Woo Lee, Hong Seok Kim, Byung Il Kwon and Byung Taek Kim, "New rotor shape design for minimum torque ripple of SRM using FEM," in *IEEE Transactions on Magnetics*, vol. 40, no. 2, pp. 754-757, March 2004, doi: 10.1109/TMAG.2004.824803.
- [56] M.Kasprzak, "6/14 Switched Reluctance Machine Design for Household HVAC System Applications (M.A.Sc. Dissertation)," McMaster University, Hamilton, Ontario, Canada. November 2016.
- [57] Y. Yang, S. Castano, R. Yang, M. Kasprzak, B. Bilgin, A. Sathyan, H. Dadkhah and A. Emadi, "Design and Comparison of Interior Permanent Magnet Motor Topologies for Traction Application," *IEEE Transactions on Transportation Electrification*, vol. PP, no. 99, 2016.